Chaos and Relaxation in Classical and Quantum Spin Systems

Dissertation submitted to
the Combined Faculties of the Natural Sciences and Mathematics of
the Ruperto-Carola-University of Heidelberg, Germany
for the degree of
Doctor of Natural Sciences

Put forward by

Tarek A. Elsayed

Born in Giza, Egypt.

25
Oral examination: ~~28~~ October 2013

Referees: Prof. Dr. Boris Fine

Prof. Dr. Jürgen Berges

Zusammenfassung

Probleme im Kontext von Chaos und Relaxation haben eine fundamentale Bedeutung für die Untersuchung von klassischen und quantenmechanischen Vielteilchensystemen. Wir untersuchen einige der mit diesen Problemen verbundenen Fragen numerisch in klassischen und quantenmechanischen Spin-Systemen. Zu den neuen Ergebnissen, die in dieser Arbeit präsentiert werden, gehören : (i) ein bemerkenswert einfacher Algorithmus zur Unterscheidung von nicht-chaotischem und chaotischem Verhalten in klassischen Systemen mit Hilfe der Zeitreihe einer makroskopischen Observablen. Die Leistungsfähigkeit dieses Algorithmus beruht auf den qualitativen Unterschieden in den Leistungsspektren der chaotischen und nicht-chaotischen Systeme. (ii) Eine modifizierte Version der Onsager Regressionsbeziehung für Quantenzustände. (iii) Ein effizient Algorithmus zur Berechnung der Zeit-Korrelationsfunktionen bei unendlicher Temperatur in Systemen mit großen Hilbert-Räumen. (iv) Abwesenheit der exponentiellen Empfindlichkeit auf kleine Störungen in makroskopischen, nicht integrierbaren Systemen von Spins 1/2. Dieses Verhalten wird der exponentiellen Empfindlichkeit auf kleine Störungen in chaotischen klassischen Spin-Systemen gegenübergestellt. (v) Genaue numerische Untersuchungen von Free Induction Decay und Spindiffusion in bestimmten Spin-Gittern. Die Folgen dieser Ergebnisse haben Auswirkungen auf die Grundlagen der statistischen Mechanik und auf praktische Probleme wie die Berechnung des Langzeitverhaltens des Free Induction Decay in Feststoffen.

Abstract

The problems of chaos and relaxation have a fundamental importance in the study of many-body classical and quantum systems. We investigate some of the issues related to these problems numerically in classical and quantum spin systems. New results reported in this thesis include: (i) A remarkably simple algorithm for discriminating chaotic from nonchaotic behavior in classical systems using a time series of one macroscopic observable. The effectiveness of this algorithm stems from the qualitative differences in the power spectra of chaotic and nonchaotic systems. (ii) A modified version of the Onsager regression relation applicable to pure quantum states. (iii) An efficient algorithm for computing the infinite-temperature time correlation functions in systems with large Hilbert spaces. (iv) Absence of exponential sensitivity to small perturbations in macroscopic nonintegrable systems of spins 1/2 . Such a behavior is contrasted with the exponential sensitivity to small perturbations in chaotic classical spin systems. (v) Accurate numerical investigations of free induction decay and spin diffusion in certain spin lattices. The consequences of these results have implications for the foundations of statistical mechanics or practical problems such as computing the long-time behavior of the free induction decay in solids.

Acknowledgements

Only His words can express my gratitude to Him: All praise is due to Allah, Lord of the worlds, the most compassionate, the most merciful.
It is my pleasure to thank my advisor, Dr. Boris Fine, for the support, patience, and understanding that he provided during the whole period of my doctoral study. Working with Boris, I enjoyed many stimulating discussions, elaborate explanations of basic concepts, sincere advices, and considerate appreciation of our cultural differences. He was willing to share his expertise with me, available when I sought discussions with him, and keen to offer help in any complicated situation. I gratefully acknowledge the financial support from the Heidelberg Graduate School of Fundamental Physics (HGSFP) and the Institute of Theoretical Physics (ITP) during my study. I would like to thank Gesine Heinzelmann from HGSFP for her help in many administrative issues. I have benefited greatly from many free numerical libraries such as MTL4, Eigen3, GMM++, BOOST and OMP. Most of the simulation in this dissertation was performed on the BW-grid. I would like to thank Sabine Richling for her support on technical issues regarding working on the grid. I am indebted to the wonderful community at Stack Exchange websites, where I frequently asked technical and scientific questions. Special thanks to Walter Hahn for his comments on two chapters of this dissertation. Finally, I would like to thank my family for their patience, encouragement and constant support during my educational journey.

"And He taught Adam the names - all of them"

Koran, 2-31.

Contents

Contents v

1 Introduction 1

1.1 Chaos in classical dynamical systems 4

1.1.1 Lyapunov exponents 5

1.1.2 Classical spin lattices 7

1.2 Quantum chaos 8

1.2.1 Quantum signatures of chaos 10

1.2.2 Quantum chaos and the quantum-classical correspondence . 12

1.3 Numerical simulations of quantum spin systems 13

2 Detecting chaotic behavior from a time series of a macroscopic system 17

2.1 Detecting chaos from time series analysis 19

2.1.1 Information entropy quantifiers of the randomness of chaotic systems 22

2.2 Power spectra of integrable and chaotic systems 26

2.2.1 Computing power spectra by means of the Discrete Fourier Transform 26

2.2.2 Exponential tails of power spectra of chaotic systems 29

2.2.3 Power spectra of integrable systems 31

2.2.4 Finite temperatures and the transition to integrability . . . 32

2.2.5 Power spectra of quantum spin systems 34

2.3 Higher order derivatives 36

2.3.1 Very short time series 40

2.3.2 Effects of noise and inaccurate measurements of the time series 42

2.4 Beyond spin systems . . . 44
2.4.1 Toda lattice . . . 51
2.5 Summary . . . 53
2.6 Appendix . . . 54

3 Regression relations for pure quantum states and their implications for efficient computing 57
3.1 Linear response theorem and Onsager regression relation . . . 58
3.1.1 Onsager relation as the high-temperature limit of the fluctuation-dissipation theorem . . . 59
3.1.2 Onsager regression relation at finite temperature . . . 62
3.2 Quantum dynamical typicality . . . 63
3.3 Modified regression relation . . . 64
3.4 Efficient computation of correlation functions . . . 69
3.4.1 Numerical integration of Schrödinger equation . . . 70
3.4.2 Numerical verification of Onsager regression relation applied on pure quantum states . . . 71
3.4.3 Classical versus quantum: Numerical efficiency of computing correlation functions based on Onsager relation . . . 74
3.4.4 A more efficient method to compute correlation functions based on quantum dynamical typicality . . . 75
3.4.5 Comparison between three numerical methods to compute correlation functions . . . 78
3.5 Summary . . . 79

4 Sensitivity of quantum spin systems to small perturbations 81
4.1 Quantum fidelity . . . 82
4.1.1 Fidelity decay for integrable and nonintegrable quantum spin systems . . . 86
4.2 Elementary attempts to define a quantum Lyapunov exponent . . . 88
4.2.1 Novel quantifiers of sensitivity in quantum systems . . . 92
4.3 Sensitivity of Loschmidt echoes to small perturbations . . . 98
4.3.1 Computing the maximum Lyapunov exponent from the behavior of macroscopic observables of classical spin systems . 98
4.3.2 Extracting the maximum Lyapunov exponent from Loschmidt echo experiments . . . 100

4.3.3 Are Loschmidt echoes of quantum spin systems sensitive to small perturbations? 104
4.3.4 Numerical simulations of Loschmidt echoes in quantum spin systems 108
4.4 Summary 114

5 Spin diffusion and free induction decay in solids 115
5.1 Spin diffusion in quantum and classical spin systems 116
5.1.1 Spin diffusion in isotropic Heisenberg systems 117
5.1.2 Spin diffusion in anisotropic Heisenberg systems 122
5.1.3 Spin diffusion in classical spin systems 123
5.2 Free induction decay in solids 124
5.2.1 Computing free induction decay using classical spin simulation 126

6 Summary and outlook 131

Bibliography 135

1 Introduction

Many of the topics covered in this dissertation are related to the notion of chaos and integrability in classical and quantum many-body systems. Our investigations of chaos are primarily focused on the signatures of chaos in the time evolution of macroscopic observables in classical and quantum many-body systems. Several diverse issues in the physics of many-body quantum dynamics have been investigated in the course of this work. These issues include Onsager regression relation, the spin diffusion problem, and free induction decay in solids.

The complexity and richness of the phenomena occurring in strongly interacting many-body systems make them particularly interesting to investigate. However, the large number of degrees of freedom constituting these systems makes it extremely difficult to simulate them on digital computers. Therefore, novel methods and approaches are always sought to gain new insights into these systems with modest computer resources. In this work, we present some of these novel methods which were developed along with our investigations of the time evolution of macroscopic observables. The paradigmatic examples for strongly interacting classical and quantum many-body systems investigated in this dissertation are lattices of classical and quantum spin systems respectively. Lattices of classical spins are excellent examples of chaotic many-body classical systems while quan-

tum spin systems have been successfully used as the prototypes of many strongly interacting many-body systems in condensed matter physics since the advent of quantum mechanics. In the following, we give an overview of the plan for the rest of the dissertation.

In chapter 2, we summarize our efforts aiming at extracting reliable measures of chaos in many-body systems based on the analysis of time series produced by a single macroscopic observable. The advantage of this approach is that it can be applied on time series produced by many-body quantum systems as well to test the existence of quantum chaos. The success of this approach would have the potential to shed more light on the role of chaos in many-body dynamics, a topic barely understood today. However, it turned out that extracting such a measure of chaos from a time series of finite length is a challenging task. We illustrate in chapter 2 the failure of conventional approaches to detect chaos in time series produced by classical spin systems. In the same time, we present a new approach that is based on taking time derivatives to discriminate between accurately measured chaotic and nonchaotic time series [1]. This approach depends on the differences between the power spectrum of both types of time series. We show in the same chapter that the power spectra of many chaotic systems are characterized by long exponential tails, unlike integrable systems. We give several examples of the power spectra of chaotic and integrable systems, in addition to a detailed treatment of an exceptional case, namely the Toda lattice [2].

An excellent example of a many-body quantum system that has been studied since long time is the nuclear magnetic dipoles in solids. The dynamics of this system can be probed by Nuclear Magnetic Resonance (NMR) techniques, a well established field of experimental physics. The universal long time behavior of the correlation function of this system was conjectured to reflect analogies with classically chaotic systems [3]. This observation, in addition to the practical importance of finding a controllable algorithm to compute the correlation function of the nuclear spin system, has encouraged us to look for unconventional approaches to do this computation. The answer came quickly from the linear response theory. One of the fundamental results in this theory states that the relaxation of an observable in the linear response regime towards equilibrium follows the same laws (resembles) the correlation function of that observable at equilibrium. This is known as Onsager regression relation. In chapter 3, we verify the applicability of this relation to quantum spin systems on the level of single pure states [4].

In the same chapter, we introduce a new relation, the modified regression relation. This relation deals with another type of correlation functions that describes the correlation in the time dependence of the expectation values at equilibrium. We show that this correlation function obeys a similar regression relation to the one dealt with in the original Onsager regression relation. The potential to use the quantum regression relation as a resource for efficient computing of correlation functions is emphasized. This method is used in subsequent chapters to compute correlation functions for systems too large to be solved by exact diagonalization methods.

In chapter 4, we revisit the problem of chaos in many-body systems from another perspective, and ask the following important question: Can we find an experimentally realizable technique that detects chaotic dynamics in many-body spin systems from the behavior of macroscopic observables? We propose the answer to this question in terms of Loschmidt echo experiments, and show that indeed for classical chaotic spin systems, one can extract reliable information on the Lyapunov exponent from measurable macroscopic quantities [5]. We give analytic and numerical arguments that this criterion indicates the absence of exponential sensitivity in quantum spin 1/2 systems. This result is an important one since it indicates that a quantum spin 1/2 system is a limiting case that exhibits no macroscopic manifestation of chaotic dynamics in terms of sensitivity to small perturbations. In the same chapter, we search for signatures of exponential sensitivity in quantum spin systems in terms of other measures such as quantum fidelity, with negative outcomes [1].

Chapter 5 deals with two separate issues in the physics of classical and quantum spin systems that evolved during the investigations reported in the previous chapters. First, we consider the issue of spin transport in Heisenberg lattices, and explore in detail the issue of spin diffusion from various perspectives.

The parallels between classical and quantum spin dynamics manifested in various domains indicate that we can use classical spin simulation to compute approximate solutions for the correlation functions of many-body quantum spin systems that are not accessible to direct numerical simulation. We verify this assumption in the second part of chapter 5 by comparing classical spin simulation with various experimental data of quantum spin systems obtained in NMR experiments.

[1] Many of the analytical arguments and derivations given in chapter 3 and chapter 4 are due to my advisor, Prof. Boris Fine.

The research reported in this thesis appeared in the following publications:
(i) T. A. Elsayed, B. Hess, and B. V. Fine, "Detecting microscopic chaos in a time series of a macroscopic observable," arXiv:1105.4575, 2011.
(ii) T. A. Elsayed and B. V. Fine, "Regression relation for pure quantum states and its implications for efficient computing," Phys. Rev. Lett., vol. 110, p. 070404, 2013.
(iii) B. V. Fine, T. A. Elsayed, C. M. Kropf, and A. S. de Wijn, "Absence of exponential sensitivity to small perturbations in nonintegrable systems of spins 1/2," arXiv: 1305.2817, 2013.

In this chapter, the primary focus will be on the concept of chaos in classical and quantum systems. Additionally, the numerical methods utilized to simulate classical and quantum spin systems are briefly discussed.

1.1 Chaos in classical dynamical systems

Explaining the statistical behavior of many-particle systems (e.g., diffusion, ergodicity, equilibration,..etc.) on the basis of the dynamical laws of physics is one of the big problems in physics today [6]. It has been long supposed that microscopic chaos is responsible for the equilibrium and non-equilibrium properties of gases, liquids and solids. This supposition has never been verified experimentally. For example, chaos is often invoked to explain Brownian motion based on the randomness generated by the underlying chaotic dynamics [7–9]. Experimental evidence for this assumption has been considered inconclusive and controversial [10, 11]. Therefore, nonlinearity and microscopic chaos are believed to be sufficient to produce Brownian motion, but they may not be necessary conditions. Another example closer to the scope of this dissertation is the long time behavior of the correlation functions of classical and quantum spin systems which has been shown to be generically similar to a damped harmonic oscillator [12, 13]. While the notion of chaos is sufficient to produce the exponential decay of the correlation functions, we do not know whether it is a necessary condition or not.

The most notable signatures that define the phenomena of chaos in classical mechanics is deterministic randomness and exponential sensitivity to initial conditions, both are related to the concept of unpredictability. Exponential sensitivity to initial conditions means that the smallest perturbations to the initial state of

the system grow up exponentially, due to intrinsic dynamical instability caused by the nonlinearity of the equations of motion and hence inhibit the predictability of the state of the system. Since initial conditions are never known with an arbitrary accuracy, the evolution of the system will look effectively random, even though it is deterministic. If one initializes a chaotic system with two initial states slightly far from each other in phase space, then the trajectories of these states will eventually diverge exponentially from each other. Dynamical systems possessing this property are called "chaotic". In this dissertation, we use the terms, chaotic and nonintegrable, synonymously in the classical domain. On the other hand, a classical system consisting of N degrees of freedom is completely integrable if it has N independent integrals of motion which are mutually in involution with respect to Poisson brackets [14].

An alternative definition of chaos that captures the idea of deterministic randomness can be given in terms of Kolmogorov algorithmic complexity, which measures the complexity of a signal by the length of the shortest program running on a universal computer that can generate this signal. A truly random signal would require a never-ending program to generate it. A signal produced from a system with exponential sensitivity to small errors of the initial conditions would also require an infinitely long program to store the information of the initial conditions. Therefore, the two definitions are equivalent [15].

1.1.1 Lyapunov exponents

The quantities which measure the rate of divergence of a bunch of trajectories along several directions in phase space, and hence characterize the sensitivity to initial conditions, are called Lyapunov exponents. Positive and negative Lyapunov exponents correspond to directions of expansions and contractions in phase space respectively. A conservative system has an equal number of positive and negative Lyapunov exponents. If the system is ergodic, then the Lyapunov spectrum does not depend on where the trajectory is started from. The directions in phase space corresponding to conservative quantities (integrals of motion) are associated with zero Lyapunov exponents. A system is technically called chaotic if it has at least one positive Lyapunov exponent.

Consider an initial probability density function, in an N-dimensional phase space, which is uniform in an infinitesimal N-sphere and zero everywhere else. In the course of time evolution, the sphere will deform in various directions into an

N-ellipsoid. The i$^{\text{th}}$ Lyapunov exponent, λ_i, is defined in terms of the i$^{\text{th}}$ ellipsoidal principal axis p_i as [16]

$$\lambda_i = \lim_{t\to\infty} \frac{1}{t} \log \frac{p_i(t)}{p_i(0)}. \tag{1.1}$$

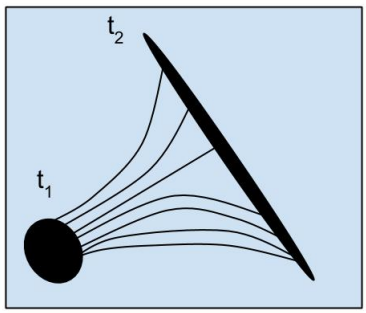

Figure 1.1: Divergence of a continuous set of initially close trajectories in a chaotic phase space.

Out of the whole Lyapunov spectrum, the maximum Lyapunov exponent (λ_{max}) has a particular importance since it defines the existence of chaos and dominates the long-time properties of the dynamics. To obtain λ_{max} numerically, we define the distance vector between two nearby states in phase space to be $\bar{\mathbf{D}}$, and compute the rate of exponential increase of $|\bar{\mathbf{D}}(t)|$. Computing this distance requires access to all the coordinates in phase space (information about all the degrees of freedom of the system). The maximum Lyapunov exponent is defined as [17]

$$\lambda_{\max} = \lim_{t\to\infty, |\bar{\mathbf{D}}(0)|\to 0} \frac{1}{t} \ln \frac{|\bar{\mathbf{D}}(t)|}{|\bar{\mathbf{D}}(0)|}. \tag{1.2}$$

For bounded systems (e.g., classical spin systems) the distance vector $\bar{\mathbf{D}}(t)$ can not grow indefinitely. Therefore, we need to manually reset $\bar{\mathbf{D}}(t)$ to the initial distance $\bar{\mathbf{D}}(0)$ every τ, where τ is a finite duration, in order to avoid $|\bar{\mathbf{D}}(t)|$ becoming of the order of the diameter of the phase space. Following ref. [18], we propagate two trajectories starting from nearby initial conditions (usually called reference orbit and test orbit) for N steps (corresponding to a duration of $N\tau$) and compute the phase space distance vector $\bar{\mathbf{D}}(\tau)$ between the two trajectories at the end of each step. At the beginning of each step τ, the distance vector $\bar{\mathbf{D}}$ is rescaled so

that it has the same length as $\bar{\mathbf{D}}(0)$. For chaotic systems, $\lambda(t_N)$ defined as

$$\lambda(t_N) = \frac{1}{N\tau} \sum_{n=1}^{N} \ln \left(\frac{|\mathbf{D}(\mathbf{t_n})|}{|\mathbf{D}(\mathbf{t_0})|} \right), \tag{1.3}$$

should converge to the maximum Lyapunov exponent for large N.

1.1.2 Classical spin lattices

The model system for our investigations of classical many-body dynamics is the classical spin lattice. At each lattice site, there exists a classical spin represented by a vector $\mathbf{S}_i$ with constant norm $|\mathbf{S}_i|^2 = 1$ and spin components (S_{ix}, S_{iy}, S_{iz}). Each spin $\mathbf{S}_i$ precesses around its local field $\mathbf{h}_i$ produced by all other spins according to

$$\dot{\mathbf{S}}_i = \mathbf{S}_i \times \mathbf{h}_i. \tag{1.4}$$

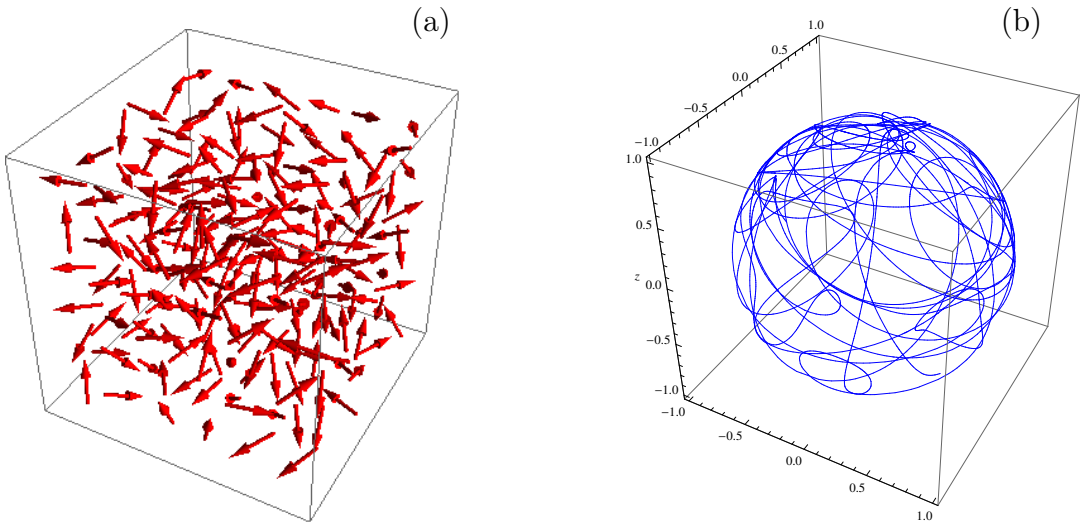

Figure 1.2: (a) A lattice of classical spins. (b) A sample trajectory of a single classical spin on the unit sphere.

The local field $\mathbf{h}_i$ is defined by the Hamiltonian of the system, which specifies the interaction between the spins. For example, a lattice with nearest neighbor interactions has the Hamiltonian

$$H = \sum_{i<j}^{NN} J_x S_{ix} S_{jx} + J_y S_{iy} S_{jy} + J_z S_{iz} S_{jz}, \tag{1.5}$$

where J_x, J_y and J_z are coupling coefficients and the local field $\mathbf{h}_i = \sum_j^{NN} J_x S_{jx} \hat{\mathbf{e}}_x + J_y S_{jy} \hat{\mathbf{e}}_y + J_z S_{jz} \hat{\mathbf{e}}_z$ where $\hat{\mathbf{e}}_x$, $\hat{\mathbf{e}}_y$ and $\hat{\mathbf{e}}_z$ are unit vectors. To solve 1.4 numeri-

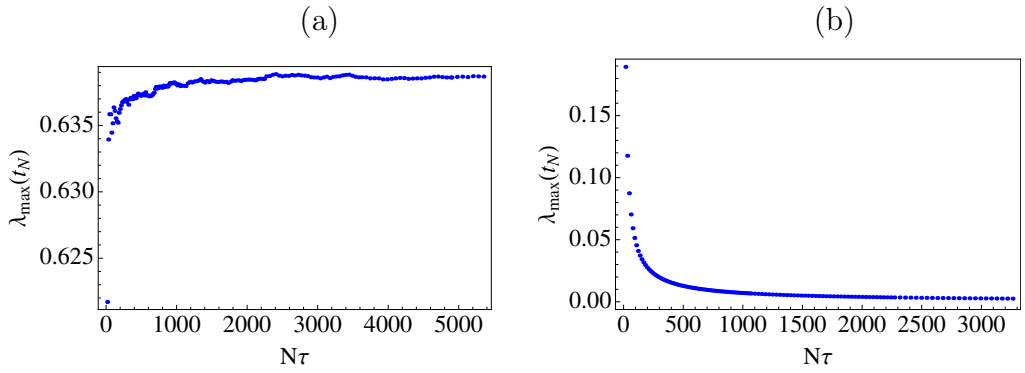

Figure 1.3: $\lambda_{max}(t_N)$ for a lattice of $20 \times 20 \times 20$ classical spins with nearest neighbour interaction. (a): Chaotic system with coupling coefficients $J_x = -0.65$, $J_y = -0.3$ and $J_z = 0.7$ (b): Integrable Ising system with coupling coefficients, $J_x = 0$, $J_y = 0$ and $J_z = 1$.

cally, we use a fourth-order Runge Kutta algorithm. The distance vector $\bar{\mathbf{D}}$ between the test orbit and the reference orbit include all the spin vector components $\{\delta S_{1x}, \delta S_{1y}, \delta S_{1z}, \delta S_{2x}, \delta S_{2y}, \delta S_{2z}, ...\}$, where $\delta S_{i\alpha}$ is the difference between the α^{th} component of the i^{th} spin of the reference and test orbits. We illustrate in Fig. 1.3-a the calculation of $\lambda_{max}(t_N)$ for a 3D lattice consisting of $20 \times 20 \times 20$ spins with nearest neighbour interaction and coupling coefficients $J_x = -0.65$, $J_y = -0.3$ and $J_z = 0.7$. We took the value of the resetting time step τ to be 15, and the initial distance between the test and reference orbits to be 0.001. We noticed, however, that there is very little dependence on the precise values of these parameters [1]. We show for comparison, in Fig. 1.3-b, $\lambda_{max}(t_N)$ computed for the integrable Ising model having $J_x = 0$, $J_y = 0$ and $J_z = 1$, where $\lambda_{max}(t_N)$ decreases monotonically to zero as expected for a nonchaotic system. An extensive survey of the maximum Lyapunov exponents in classical spin lattices was performed in [19]. One of the main results reported in that work is that far from the integrable Ising limit, the maximum Lyapunov exponent in classical spin lattices with nearest neighbor interactions shows very little dependence on the precise choice of the coupling coefficients, J_x, J_y and J_z subject to the constraint $J_x^2 + J_y^2 + J_z^2 = 1$.

1.2 Quantum chaos

If deterministic chaos lies at the heart of statistical mechanical phenomena, where the interactions between microscopic particles are fundamentally quantum, then

the connection between chaos and quantum dynamics has to be thoroughly investigated. In this section, we give a short review of the quantum manifestations of chaos and some of the recent results in that field.

Chaotic phenomena require intrinsic nonlinearity that renders the equations of motion of the system nonintegrable. Quantum dynamics, on the other hand, are fully described by Schrödinger equation which is fundamentally linear. A bounded quantum system possesses a set of discrete energy levels and hence the evolution is quasi-periodic. The occupancies of those levels are time-invariant and play the role of the integrals of motion in an integrable classical system. In classical chaotic systems, the exponential sensitivity is driven by the continuity of the underlying phase space, which allows to specify the initial conditions up to an arbitrary accuracy. On the other hand, the notion of a point in phase space does not exist in quantum mechanics. How can one then speak about any relation between quantum systems and chaos?

One possible resolution to this question is that the energy level spectrum of many-body systems is extremely dense, and hence the time scale at which the quantum dynamics exhibits apparent nonchaotic behavior becomes extremely long. This point motivated researchers to think that the randomness generated by macroscopic quantum systems [2] may resemble classically chaotic systems [20, 21]. On the other hand, even for systems having a few degrees of freedom, it has been observed that quantum systems which have chaotic classical limits usually exhibit distinctive features that set them apart from quantum systems which have nonchaotic classical limit, in accordance with the correspondence principle [22]. These features define the scope of *quantum chaos*.

Finite quantum systems (described by finite Hilbert spaces) can always be solved exactly by limited computer resources, and hence are fully predictable. On the other hand, in the thermodynamic limit, we seek analytic solutions (i.e., analytic expressions for the energy levels, and in particular the ground state). However, not every quantum system can be solved analytically in the thermodynamic limit. Only a few classes of quantum systems (e.g., Bethe ansatz systems) can be fully integrated in that limit, and hence are called integrable systems (see [23] for other commonly used definitions of integrability). Several examples of fully solvable quantum systems are given in [24]. One intriguing question here is whether

[2] Randomness can quantified by information entropy rates, for example, which will be explained in the next chapter.

the ability to analytically solve a quantum system in the thermodynamic limit is a subjective matter or an objective matter. To avoid this philosophical issue, the scope of solvability in the definition of integrability is sometimes narrowed down to a particular method, e.g., Bethe ansatz or quantum inverse scattering methods.

Just as a completely integrable classical system possesses a complete set of symmetries equal to the number of its degrees of freedom leading to a set of integrals of motion, an integrable quantum system has a similar property. The breaking of integrability in both cases is associated with the breaking of one or more symmetries.

1.2.1 Quantum signatures of chaos

One might wonder how does the defining property of classical chaos, namely hypersensitivity to initial conditions, carries over to the quantum domain, given the intrinsic linearity of the Schrödinger evolution. In fact, since the initial conditions of a quantum system is not a point in phase space, but a vector representing the wavefunction in Hilbert space, sensitivity to the initial conditions was investigated in terms of the overlap between two slightly different initial states [25] and the rate of spread of an initial wavepacket [26]. In both cases, positive evidences were found for the dependence of the two quantities on whether the initial state of the system belongs to a classically regular or chaotic regions in the phase space. Sensitivity to initial conditions was also found in unbounded systems, where energy is not quantized, such as scattering problems. For example, consider an electron scattering from the complicated potential of a molecule. The time the electron takes before it exits the molecule and the exit direction can depend sensitively on the initial conditions [27]. It is the aim of chapter 4 to discuss the issue of the absence or existence of exponential sensitivity in quantum spin systems in more detail. Much of the research done in quantum chaos is motivated by numerical experiments. We follow the same methodology in chapter 4, by doing numerical experiments on quantum spin systems, searching for signatures of sensitivity to weak perturbations.

The most prominent signature of quantum chaos of a bounded quantum system resides in the distribution of its energy levels. It was conjectured by Bohigas, Giannoni and Schmit [28] that some properties of the quantum systems that have classically chaotic counterpart can be described by an ensemble of random matrices. In particular, the energy levels of those quantum systems and the eigenvalues

of random matrices, exhibit similar statistical properties, such as level repulsion. The precise shape of the distribution function of the energy level spacings $P(s)$, where s is the spacing between two adjacent levels, depends on the universality class to which this system belongs, which, in turn, depends on its underlying symmetries. For example, systems exhibiting time reversal symmetry exhibit the same statistics as the Gaussian Orthogonal Ensemble (GOE) of real symmetric matrices. The spacings of their eigenvalues is characterized by the Wigner-Dyson distribution $P(s) = \frac{\pi s}{2} e^{-\pi s^2/4.0}$. Integrable systems, on the other hand, exhibit level clustering. The statistics of their energy level spacings follow a Poisson distribution, $P(s) = e^{-s}$. This property is sometimes used as a definition for quantum integrability, especially in quantum systems lacking a corresponding classical limit.

For periodically driven quantum systems, the statistics of quasi-energies (eigenvalues of the time evolution operator) exhibit the same kind of behavior as the eigen-energies of time-independent systems [29]. A related approach to seek differences of the energy level distributions between chaotic and and nonchaotic systems treats the sequence of energy level as a time series. It was shown [30] that the power spectrum of this time series behaves like a $1/f$ noise in the former case and $1/f^2$ in the later. The eigenvectors of the Hamiltonian were found to exhibit qualitative differences between chaotic and nonchaotic systems as well. In particular, chaotic eigenfunctions are characterized by decaying spatial correlations and are delocalized through the whole system [31]. Consequently, they overlap and cause the level repulsion that characterize the eigenvalues of chaotic systems. The level of delocalization can be quantified by measures such as inverse participation ratio [32] and Shannon entropy [33].

The spectral differences and the structure of the eigenvectors are static criteria; but do they have any dynamical manifestation on the time-dependent behavior of quantum systems? Pechukas suggested that the survival probability, defined as $|\langle\psi(t)|\psi(0)\rangle|^2$, behaves differently in integrable and nonintegrable quantum systems due to their spectral differences [34]. We investigate this proposal for quantum spin systems in chapter 4. Another feature which was suggested to characterize quantum chaotic systems is the sensitivity of the eigenvalues to the variations of Hamiltonian parameters [35, 36]. It was proposed [22] that under variations of Hamiltonian parameters, the eigenvalues of quantum chaotic systems, which exhibit avoided crossings, should exhibit strong sensitivity to these variations, qualitatively different from integrable systems. Similar features were

suggested for the structure of the eigenfunctions [37].

1.2.2 Quantum chaos and the quantum-classical correspondence

The study of quantum chaos is very important in investigating the correspondence between classical and quantum motion. According to the Ehrenfest theorem, there is a correspondence between the quantum motion (e.g., the evolution of a quantum wavepacket) for sufficiently large quantum numbers and the motion of the corresponding classical system. This correspondence breaks down at a time scale of the order of Ehrenfest time, which depends on the typical action of the problem (S) in units of Planck's constant ($\hbar$). If the system is chaotic, the correspondence between the classical and quantum motion would break down much earlier at a time scale of the order of $\log(S/\hbar)/\lambda$, where λ is the Lyapunov exponent [38]. For a classical system which has a mixed phase space, a quantum wavepacket centred in the chaotic region will spread very rapidly compared to the one centred in the regular region.

The analogies between classical chaotic motion and the corresponding quantum motion can be investigated in coordinate space [39] or phase space [40]. A promising approach that avoids the problem of the absence of the notion of a trajectory in quantum mechanics seeks to find analogies between the evolution of classical density functions in phase space and quantum distribution functions (i.e., Wigner's function). Indeed, it was found that the complexity of the quantum motion as quantified by the number of harmonics in the density function, depends on whether the classical limit is chaotic or not. If the classical limit is chaotic, the number of harmonics in the density function increases exponentially in the classical system and only up to the Ehrenfest time in its quantum counterpart [41].

The breakdown of the correspondence between classical and isolated quantum motion makes it natural to consider the effect of an external agent, namely the environment, that may explain this discrepancy [20]. This point brings us to the field of quantum decoherence, which deals with the appearance of classical behavior in a world described fundamentally by quantum laws. Normally, a quantum system is coupled to many degrees of freedom in its environment. Theoretically, the whole system plus environment composite evolves unitarily by Schrödinger equation. Mathematically, decoherence can be viewed as the effect of tracing out

the environmental degrees of freedom on the behavior of the quantum system. This process destroys the coherence terms in the density matrix that describes the system, and causes the appearance of classical-like effects. It was found that coupling the system to one single degree of freedom which is chaotic can cause decoherence effects similar to an environment possessing many (integrable) degrees of freedom [42]. This suggests that the complexity resulting from chaotic behavior (in nonlinear systems) and the complexity of many degrees of freedom (of linear environment) may be equivalent in effect. Moreover, it was found that in quantum systems with chaotic classical analogue, decoherence occurs at a rate determined by some generalized Lyapunov exponent [43]. Finally, decoherence may provide an explanation for the origin of classical chaos, in a world dominated by the linear quantum laws of motion, if it can be shown that the process of tracing out the environment degrees of freedom brings chaos into linear quantum systems [44, 45].

1.3 Numerical simulations of quantum spin systems

A quantum spin system with nearest neighbour interaction is described by a Hamiltonian similar to 1.5, namely,

$$H = \sum_{i<j}^{NN} J_x S_{ix} S_{jx} + J_y S_{iy} S_{jy} + J_z S_{iz} S_{jz}, \tag{1.6}$$

where S_{ix}, S_{iy} and S_{iz} are the quantum spin operators at the i^{th} lattice site. When two of the coupling coefficients J_x, J_y and J_z are equal, the system is called XXZ model. If, additionally, the third coupling coefficient is zero, the system is called XX model. Similarly, when the coupling coefficients are different, the system is an anisotropic Heisenberg model, or in our nomenclature, XYZ model. We assume periodic boundary conditions in all the models studied in this work. A spin chain with the Hamiltonian 1.6 is known to be integrable by Bethe ansatz. In order to break the integrability in our investigations in chapter 4, we add next nearest neighbor interaction or disordered fields or deal with higher dimensional lattices. When we speak about the nonintegrability of these systems, we, of course, mean in the thermodynamic limit.

In order to numerically simulate a quantum spin system on a digital computer, we need first to select a basis for the Hilbert space, and then represent the operators and wavefunctions constructed in this basis on the computer. The easiest

choice to represent a Hamiltonian in the form 1.6 is to select the eigenbasis of the projection of the total spin operator in any of the three directions as the basis for the representation. We call this basis the Ising basis, since it represents the eigenbasis of a Hamiltonian with Ising coupling coefficients. Each state in this basis corresponds to a certain combination of the projection of all spins in that direction. For a system consisting of N spins 1/2, the Hilbert space is composed of 2^N basis states, whose indices range from 0 to $2^N - 1$. The state of each spin (whether up or down) is decoded in the binary representation of the index of each state. For spin systems with spin quantum number S higher than 1/2, the projection of the i$^{\text{th}}$ spin can be retrieved from the j$^{\text{th}}$ state in a similar manner by the formula: $\text{mod}(\text{integer}(j/M^i), M)) - S$, where $M = 2S + 1$.

In the above basis, the matrix representation of a Hamiltonian 1.6 will be sparse as shown in Fig.1.4-a and can be efficiently stored in a compressed form. With nearest neighbour interaction, one can store the Hamiltonian matrix of a system consisting of up to 25 spins in less than 22 GB of memory. For systems of larger sizes, we can exploit the symmetries of the problem in order to decompose the Hamiltonian into smaller blocks and process them in parallel on different computers. These symmetries correspond to operators which commute with the Hamiltonian. The above mentioned blocks correspond to particular sets of the quantum numbers corresponding to those operators. The most frequently used symmetries in the present work are [46]:

- Rotational symmetry: In this case, the total spin projection in one or more directions for the entire lattice is conserved. For example, the total spin polarization $m_z = \sum_i^N S_{iz}$ is conserved in the XXZ Hamiltonian. Therefore, the Hamiltonian can be decomposed into different blocks corresponding to different eigenvalues of m_z.

- Translation symmetry: In this case, the spatial translation operator $\hat{T}$ commutes with the Hamiltonian, and different blocks correspond to different eigenvalues of $\hat{T}$. The states used in this representation satisfy $\hat{T}|\Psi(k)\rangle = e^{ik}|\Psi(k)\rangle$. For a 1D chain consisting of N spins, the value of k is given by $\frac{2n\pi}{N}$, where n is an integer that ranges from 0 to $N - 1$. A schematic of the block diagonal form of the Hamiltonian 1.6 for a spin 1/2 chain consisting of 8 spins in the eigenbasis of the translation operator $\hat{T}$ is shown in Fig.1.4-b.

Representing the Hamiltonian matrix in a block diagonal form as in Fig.1.4-b is

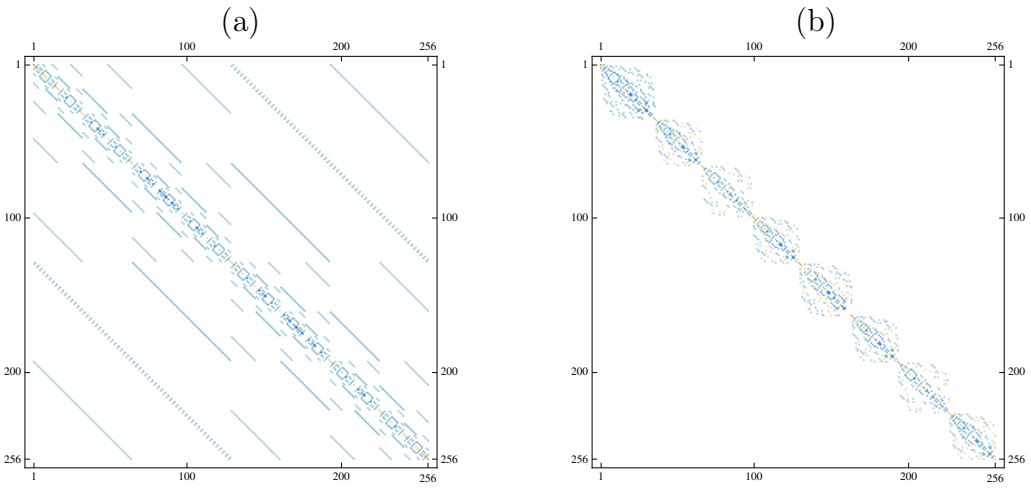

Figure 1.4: (a) A schematic of the Hamiltonian matrix for a quantum spin-1/2 chain consisting of 8 spins with nearest neighbour interaction, periodic boundary conditions and coupling coefficients $J_x = -0.65$, $J_y = -0.3$ and $J_z = 0.7$ in the Ising basis in the z direction (b) A schematic of the same Hamiltonian matrix in (a) in the translationally invariant basis $|\Psi(k)\rangle$.

particularly important when doing exact diagonalization by routines which accept only dense matrix formats (e.g., LAPACK routines). Note that we can obtain the level statistics that characterize the integrability or the lack thereof only for a single block of the Hamiltonian matrix that can not be further decomposed into block structure form, after considering all possible symmetries of the problem. The eigenvalues of each block matrix have to be further unfolded, such that they have the same average local spacing [29].

After the states and operators are represented on the computer, we need to solve the time-dependent Schrödinger equation numerically. In this work, we follow one of two methods: Exact diagonalization and fourth-order Runge Kutta algorithm. In the first method, the eigenvalues and eigenvector of the Hamiltonian matrix (usually in its block structure form) are obtained by one of LAPACK routines and all the wavefunctions and operators are transformed into the new basis states represented by the eigenvectors. In this basis, the evolution of pure states is a straightforward phase rotation algorithm. We defer the discussion of the second method to chapter 3.

There is one thing even more vital to science than intelligent methods; and that is, the sincere desire to find out the truth, whatever it may be.

Charles Pierce

2

Detecting chaotic behavior from a time series of a macroscopic system

In this chapter, we will be concerned with detecting chaos in classical systems by observing a single degree of freedom of those systems. We shall call the time evolution of such an observable henceforth a time series. The conventional definition of chaos in terms of the exponential divergence of nearby phase space trajectories requires access to all the degrees of freedom of the system in order to detect chaotic behavior. In many cases, and, in particular, in systems consisting of many degrees of freedom, gaining this access is not possible. Often, we are provided with a single time series representing the evolution of a single macroscopic observable over a period of time and asked to analyse this time series to determine whether the underlying dynamics is integrable or chaotic. This time series can be the output power of a laser system [47], the electrocardiography (ECG) recording of the human heart [48], or the stock market prices [49]; just to mention a few examples.

To probe into the nature of the underlying dynamics of a many-body dynamical system from observing one single degree of freedom is a challenging task. After observing a time series produced by an unknown system, two questions need to be answered: First, is the underlying system stochastic or deterministic? Second, if

it is deterministic, is it regular or chaotic? Here, we are only concerned with the second question. The ultimate goal of searching for a robust technique to detect chaotic behavior from observed data in our agenda is to apply that technique to time series observed from a macroscopic quantum system. A possible example is the spin noise signal observed by monitoring the equilibrium fluctuations of the total magnetization of nuclear spins in solids which has been already measured by several groups [50, 51] (see chapter 3 for more details).

Several techniques were developed to analyse time series and extract measures of chaotic behavior from it. Normally, these techniques require analysing very long time series to reach reliable conclusions. Many techniques aim to detect chaos by quantifying the randomness of the time series. The quantity which encapsulates this randomness is called rate of entropy production. A notable experiment in this direction was the measurement of the Brownian motion of a macroscopic particle suspended in water [10]. The positive entropy rate evaluated from the coordinate time series of the particle was initially considered an evidence for the existence of microscopic chaos in the motion of the water molecules. This method, however, was criticized as being inconclusive since similar entropy rates can be produced by nonchaotic systems [11]. This example illustrates how difficult it is to reach reliable conclusions about the nature of the underlying dynamics by analysing a time series of finite length. The failure of standard time series analysis techniques to distinguish chaotic from nonchaotic dynamics was reported in [52].

After we briefly review several techniques to detect chaos from a time series and illustrate the failure of those techniques for realistic finite-length time series for many-particle systems, we report on a new approach that can help improve the effectiveness of these methods [1]. This approach relies on the fact that, unlike integrable systems, power spectra of time series produced by chaotic systems exhibit long exponential tails as a function of frequency. It turns out that this exponential tail has important consequences on the time derivatives of the time series and their intrinsic randomness, quantified by entropy production rates.

In this chapter, we consider a classical spin lattice as a model of dynamical system consisting of many degrees of freedom. We apply the new approach on the magnetization time series to discriminate integrable from nonintegrable dynamics. The effects of the equilibrium temperature and the transition to integrability on the exponential tail in the power spectra of the nonintegrable classical spin systems are investigated. We present the power spectra of several integrable and nonintegrable

systems other than classical spin lattices and comment briefly on the power spectra of quantum spin systems.

2.1 Detecting chaos from time series analysis: A short review

There are several algorithms that aim to extract the maximal Lyapunov exponent, the primary indicator of chaos, from observed time series [1] [54–57]. In particular, the algorithm proposed in [57] searches for similarly looking patterns in the time series that can be considered emanating from nearby points in the complete phase space describing the dynamical system. To measure the rate of divergence between the trajectories originating from those points, the distance between time series segments following those similar patterns is measured as a function of time. This distance is considered to be a projection of the difference vector in the complete phase space onto one dimension and hence is expected on average to grow exponentially by a rate determined by the maximal Lyapunov exponent. This process is averaged over the whole time series.

In quantitative terms, if we identify all possible patterns of length T in the time series, we define the distance between two patterns x_r and x_t at a given instant of time by the absolute difference between the two patterns at that instant,

$$\text{dist}[x_r(t), x_t(t)] = |x_r(t) - x_t(t)|, \tag{2.1}$$

where t is measured from the beginning of the pattern. We consider a pair of patterns x_r and x_t to correspond to the same phase space point with respect to a resolution ϵ, if the maximum distance between any corresponding pair of points belonging to these two patterns is smaller than ϵ, i.e.,

$$\max_{t:0\to T}\{\text{dist}[x_r(t), x_t(t)]\} < \epsilon. \tag{2.2}$$

We call such pair of patterns x and x_ϵ. The asymptotic growth of the distance between these patterns is expected to be controlled by the maximum Lyapunov

[1] Apart from section 2.4, we are mainly concerned with conservative systems. For chaotic dissipative systems, several algorithms were developed to estimate the fractal dimension of the chaotic attractor which characterize the phase space of those systems from time series analysis (see, e.g., [53].)

exponent λ_{max}. Therefore, we can compute λ_{max} as

$$\lambda_{max} = \lim_{\epsilon \to 0} \frac{1}{\tau} \log \left\langle \frac{|x(t+\tau) - x_\epsilon(t+\tau)|}{\epsilon} \right\rangle, \tag{2.3}$$

where the average $\langle \cdots \rangle$ is taken over all pairs that satisfy 2.2.

Let us illustrate this algorithm by applying it to the two-body Henon-Heiles problem defined by the Hamiltonian

$$H = \frac{1}{2}(p_1^2 + p_2^2 + q_1^2 + q_2^2) + q_1^2 q_2 - \frac{1}{3} q_2^3, \tag{2.4}$$

where (q_1, q_2) and (p_1, p_2) are the coordinates and momenta of the two particles respectively. We show in Fig. 2.1 the growth of $\langle |x(t+\tau) - x_\epsilon(t+\tau)| \rangle$ for two different sets of initial conditions $\{q_1 = 0, q_2 = -0.15, p_1 = 0.5542, p_2 = 0\}$ and $\{q_1 = 0, q_2 = -0.15, p_1 = 0.45, p_2 = 0\}$ corresponding to energies $E_1 = 0.166$ and $E_2 = 0.1136$ respectively, where $x(t)$ is taken to be the coordinate of the second particle $q_2(t)$. The value of the maximum Lyapunov exponent λ_{max} in each case is computed independently as in 1.3. The results for $\lambda_{max}(t_N)$ shown in Fig. 2.1-c indicate that λ_{max} converges to 0.13 s^{-1} and 0.036 s^{-1} respectively. The fitting of $\langle |x(t+\tau) - x_\epsilon(t+\tau)| \rangle$ with $ce^{\lambda_{max} t}$ in each case in Fig. 2.1-a illustrates the accuracy of this method.

In many-dimensional systems, we expect that this procedure would require very long time series to compensate for the effect that similar patterns can originate from phase space trajectories that are not close to each other in the many-dimensional phase space. That would require taking longer patterns, and hence the tremendous number of distinctive patterns would require considering an extremely long time series to have good statistics. For example, in Fig. 2.2, we illustrate the same algorithm for an integrable chain of 10 classical spins with Ising coupling coefficients ($J_x = 0, J_y = 0$ and $J_z = 1.0$). We have analyzed 9600 time series, each of length 10^6. Taking the length of each pattern $T = 25$, and the time interval between two adjacent patterns to be 10, the total number of patterns analyzed $= 9.6 \times 10^8$. Within a resolution $\epsilon = 0.1$, we found that only 1281 pairs of patterns satisfy the condition 2.2. On the other hand, implementing the same procedure, with the same parameters for a nonintegrable classical spin chain with the anisotropic coupling coefficients, $J_x = 0.873, J_y = -0.436$ and $J_z = 0.218$, the number of similar pattern pairs found within the same resolution is zero! Taking the value of ϵ larger than 0.1 to increase the probability of finding similar patterns, would narrow the range of growth of $\langle |x(t+\tau) - x_\epsilon(t+\tau)| \rangle$

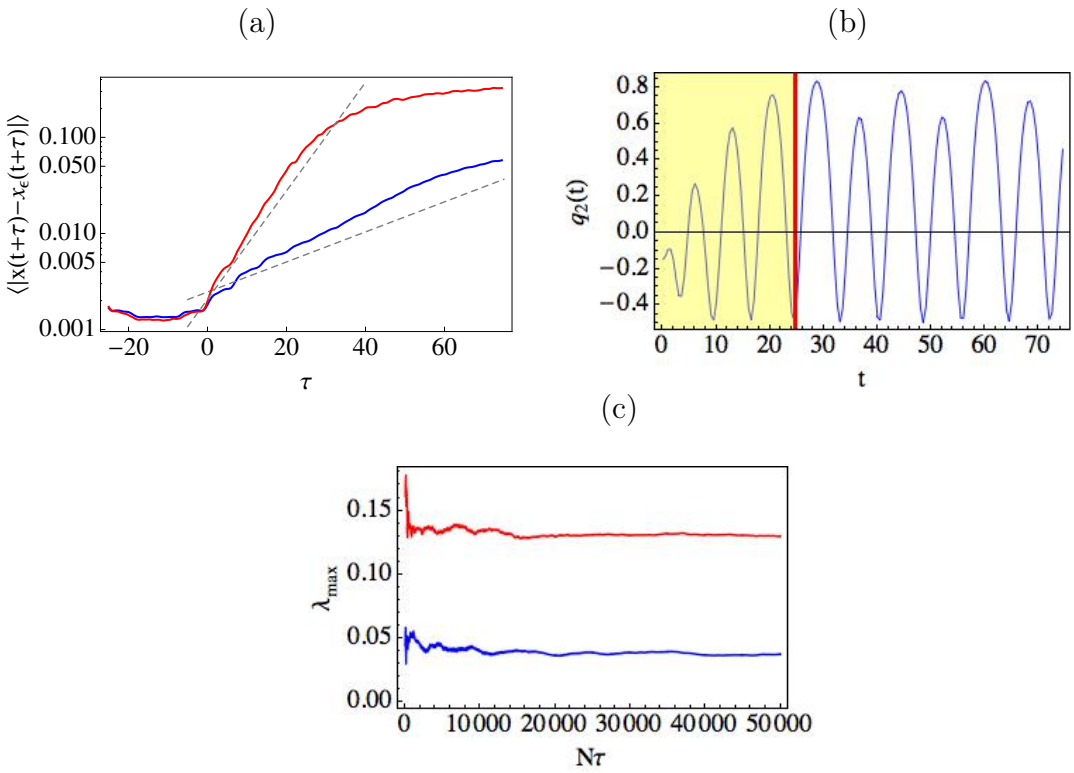

Figure 2.1: (a) The average of $|x(t+\tau) - x_\epsilon(t+\tau)|$ for the Henon-Heiles problem, where x represents the coordinate q_2, and $\epsilon = 0.005$. The blue plot corresponds to initial conditions $\{q_1 = 0, q_2 = -0.15, p_1 = 0.45, p_2 = 0\}$ while the red plot corresponds to initial conditions $\{q_1 = 0, q_2 = -0.15, p_1 = 0.5542, p_2 = 0\}$. The two plots were obtained by analysing a time series of length 6.5×10^6. The dashed line represents the function $ce^{\lambda_{max}t}$, where $\lambda_{max} = 0.13$ and 0.036 is the maximum Lyapunov exponent for the two initial conditions respectively. (b) A sample of the time series of $q_2(t)$, a single pattern is highlighted in yellow. This figure illustrates the length of the pattern considered in the calculation with respect to the time scale of the motion. (c) $\lambda_{max}(t_N)$ as computed in 1.3 for the two initial conditions.

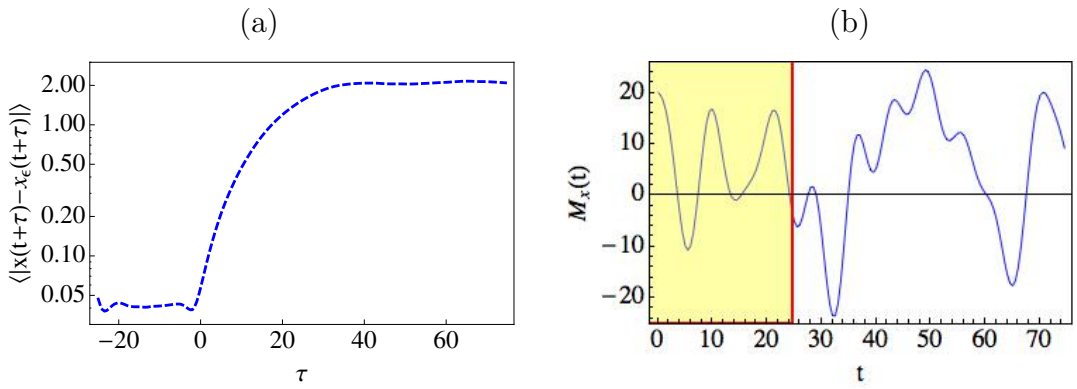

Figure 2.2: (a) The average of $|x(t+\tau) - x_\epsilon(t+\tau)|$ for an Ising classical spin chain consisting of 10 spins, where x represents the total magnetization M_x and $\epsilon = 0.1$. (b) A sample of the time series of $M_x(t)$, a single pattern is highlighted in yellow.

before it saturates, and consequently make it difficult to detect any exponential growth. On the other hand, we can consider the mere difference of the statistics of similar patterns between integrable and chaotic systems to be a yes/no criterion to diagnose chaotic behavior in many-body systems. This approach requires more detailed investigation.

2.1.1 Information entropy quantifiers of the randomness of chaotic systems

Another class of measures that can be extracted from a time series is the entropic measures. These measures aim at characterizing the rate of entropy production by the system, or more simply, the ability of the system to "produce information". The entropy production of the system is defined in terms of the description of its evolution in phase space, involving all the degrees of freedom. However, it has been shown that the rate of entropy production (as defined later) can be estimated from time series analysis [58, 59].

So far, the rate of Kolmogorov-Sinai (KS) entropy production is the most famous entropic measure used to distinguish between chaotic and nonchaotic dynamics. In order to define the KS entropy, let us consider a dynamical system described by a phase space which is course-grained, i.e., divided into small cells of dimension L, as in Fig. 2.3. Let us assume that we start with an ensemble of initial conditions at time t_1 described by a probability distribution $\rho(t_1)$ over the phase space. As the ensemble evolves in time, the probability distribution evolves to a different shape with a different footprint on the cell structure of the phase

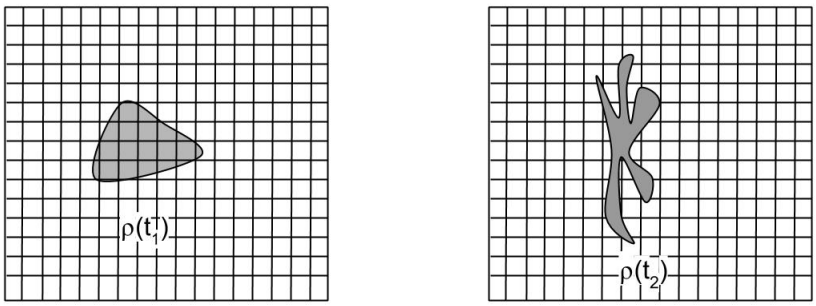

Figure 2.3: The evolution of the probability density function $\rho(t)$ in a course grained phase space.

space. If we discretize the time flow in equal units τ and consider the trajectories emerging from a certain cell at $t = t_1$, then we can define a distinct sequence of cells $\mathcal{L}(n)$ traversed by each of these systems up to the $\underline{\text{n}^{\text{th}}}$ unit of time. We can assign each sequence $\mathcal{L}_i(n)$ a probability $p_i(n)$ proportional to how many system trajectories correspond to this sequence. The KS entropy S_n at time $n\tau$ is defined as [60]

$$S_n = \langle \sum_i -p_i(n) \log p_i(n) \rangle, \tag{2.5}$$

where the average is taken over all initial cells. The rate of KS entropy production $\mathcal{S}$ is defined as the average rate of increase of S_n in the limit of very long trajectories, very small time step and very small cell size:

$$\mathcal{S} = \lim_{\substack{n\to\infty \\ L\to 0 \\ \tau\to 0}} \frac{1}{n\tau}(S_n - S_0). \tag{2.6}$$

An alternative way to calculate $\mathcal{S}$ is to compute

$$S_n = \langle \sum_r -p_r(n) \log p_r(n) \rangle, \tag{2.7}$$

where $p_r(n)$ is the probability that a trajectory starting from a certain initial cell will pass through the $\underline{\text{r}^{\text{th}}}$ cell after n units of time. The average is taken aver all initial cells. The rate of change of S_n is given by $\frac{S_{n+1}-S_n}{\tau}$. The average of this rate over N units of time is given by $\frac{1}{N\tau}\sum_{n=0}^{N-1}(s_{n+1} - s_n) = \frac{1}{N\tau}(s_N - s_0)$. The rate of KS entropy production ($\mathcal{S}$) is obtained after taking the same limits in 2.6, namely,

$$\mathcal{S} = \lim_{\substack{N\to\infty \\ L\to 0 \\ \tau\to 0}} \frac{1}{N\tau}(s_N - s_0). \tag{2.8}$$

The rate of KS entropy production was shown to be equal to the sum of positive Lyapunov exponents of a bounded system (Pesin identity) [61]. A positive and finite value of $\mathcal{S}$ indicates that the system is chaotic. In contrast, for integrable systems, $\mathcal{S} = 0$.

To achieve the goal of this chapter, we have to find a prescription to extract the rate of KS entropy production from a time series, without access to the full phase space dynamics. To deal with a continuous time series on a digital computer, we need to discretize both the time axis and assume a minimum resolution ϵ for the quantity characterized by the time series (the vertical axis). The entropy defined for such a discretized time series is called the (ϵ, τ)-entropy. This coarse grained entropy should be able to determine the timescale of the predictability of the system [47]. A popular numerical implementation of an (ϵ, τ) version of the Kolmogorov-Sinai entropy from a time-series is the Grassberger-Procaccia method [58] and its slightly modified Cohen-Procaccia (CP) (ϵ, τ) entropy [60, 62].

In the following two sections, we consider the time series representing the x-component of the total magnetization for a cubic classical spin lattice with nearest neighbor interaction. As a prototype for a chaotic system, we consider an anisotropic Heisenberg system, with coupling coefficients $J_x = -0.65, J_y = -0.3$ and $J_z = 0.7$, while for the integrable system we consider the Ising limit (the only integrable limit for this Hamiltonian [19]) with coupling coefficients $J_x = J_y = 0$ and $J_z = 1$.

Let us first describe how we can apply the more popular Shannon entropy to extract the rate of the (ϵ, τ)-entropy production and then introduce the CP (ϵ, τ)-entropy. To calculate the (ϵ, τ) Shannon entropy rate for a time series of length T, we discretize the magnetization axis uniformly in steps of ϵ and the time axis in steps of τ to obtain a new discretized version of the time series (a stream of symbols). We group each block of symbols of length $N\tau$ in the time series in one pattern, and catalogue all patterns in the time series. The (ϵ, τ) Shannon entropy associated with patterns of length N is given by

$$H_{Sh}(\epsilon, \tau, N) = -\sum_i P_i \; Log \; P_i, \tag{2.9}$$

where P_i is the probability of occurrence of the $\underline{\text{i}^{\text{th}}}$ pattern and the sum runs over all distinct patterns of length N. The Shannon (ϵ, τ) entropy per unit time is

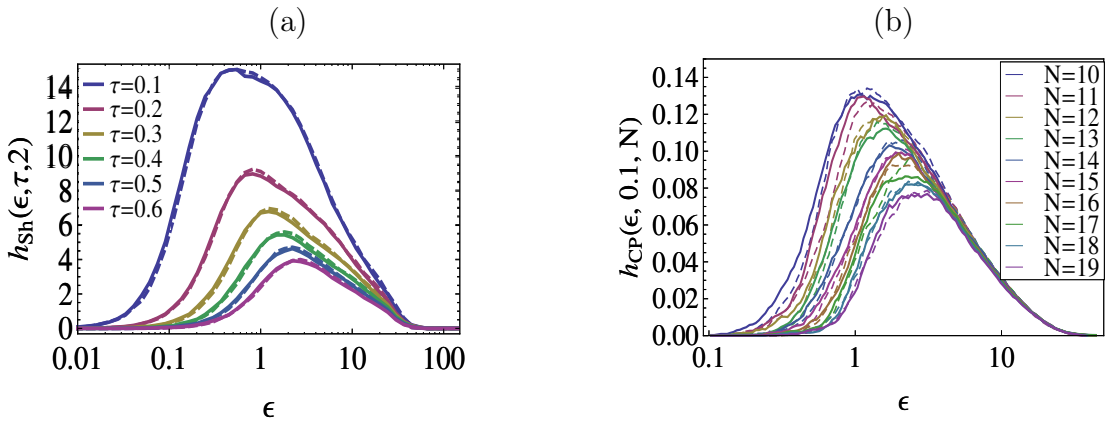

Figure 2.4: (a) Comparison between the entropy rates $h_{Sh}(\epsilon, \tau, N)$ produced by the chaotic system (solid lines) and by the integrable system (dashed lines) for $N = 2$ and different values of τ. (b) Comparison between the entropy rates $h_{CP}(\epsilon, \tau, N)$ for the chaotic time series (solid lines) and the integrable time series (dashed lines), with $\tau = 0.1$ and various values of N. Curves reaching higher maximum values of h_{CP} correspond to the smaller values of N [1].

given by $\lim_{N\to\infty} h_{Sh}(\epsilon, \tau, N)$, where

$$h_{Sh}(\epsilon, \tau, N) = \frac{1}{\tau}\,[H_{Sh}(\epsilon, \tau, N+1) - H_{Sh}(\epsilon, \tau, N)]. \tag{2.10}$$

For chaotic systems, the value of $h_{Sh}(\epsilon, \tau)$ approaches a constant nonzero value in the limits $T \to \infty$, $N \to \infty$, $\epsilon \to 0$ and $\tau \to 0$. Taking N very large or taking ϵ very small is not practical because the finite length of the time series does not allow all possible patterns to be fairly represented.

We illustrate the inefficiency of this approach to distinguish between finite time series representing the total magnetization produced by the integrable and chaotic spin systems in Fig. 2.4-a. We plot $h_{Sh}(\epsilon, \tau, 2)$ for different values of τ ranging from 0.1 to 0.6 and a range of ϵ covering four orders of magnitude. It is evident that the plots for both the integrable and chaotic systems are almost indistinguishable.

Unlike Shannon entropy, the CP (ϵ, τ) entropy does not require the discretization of the magnetization axis. Instead, the distance d_{ij} between two patterns x_i and x_j of length N is defined as the maximum of the absolute differences between corresponding data points appearing in each of the two patterns, i.e.,

$$d_{ij} = \max_{n:1\to N}\{\text{dist}[x_i[n], x_j[n]]\}, \tag{2.11}$$

where $\text{dist}[x_i[n], x_j[n]] = |[x_i[n] - x_j[n]]|$. To calculate the CP (ϵ, τ) entropy,

$H_{CP}(\epsilon, \tau, N)$, a group of R reference patterns of length N is selected randomly. The probability P_i of a certain reference pattern x_i is obtained by counting the number of all other patterns x_j in the time series that are within distance ϵ from that reference pattern, i.e., satisfy $d_{ij} < \epsilon$. The CP (ϵ, τ) entropy is defined as [60]

$$H_{CP}(\epsilon, \tau, N) = -\frac{1}{R} \sum_{\{R\}} \log P_i. \tag{2.12}$$

The rate of the CP (ϵ, τ)-entropy production is defined by $\lim_{N\to\infty} h_{CP}(\epsilon, \tau, N)$, where

$$h_{CP}(\epsilon, \tau, N) = \frac{1}{\tau} \left[H_{CP}(\epsilon, \tau, N+1) - H_{CP}(\epsilon, \tau, N)\right]. \tag{2.13}$$

In Fig. 2.4-b, we plot $h_{CP}(\epsilon, \tau, N)$ for discretization time step $\tau = 10$ and pattern lengths ranging from 10τ to 19τ for both integrable and chaotic spin clusters. Ideally, for a chaotic system, the plots of CP entropy rates should converge to a single plateau as the pattern length increases, but due to the finite length effects (T=1000), they do not. We notice in Fig. 2.4-b that the CP-(ϵ, τ) entropy, like the Shannon entropy, is not capable either of distinguishing integrable from chaotic many-particle dynamics due to the finite length of our time series.

The failure of the techniques discussed in this section to detect chaotic behavior in many-particle systems has motivated us to look for other approaches to diagnose chaos. Our efforts culminated in the time derivatives technique discussed later in this chapter. This technique relies on the difference between the power spectra of integrable and chaotic systems. We discuss these differences in the following section.

2.2 Power spectra of integrable and nonintegrable systems

2.2.1 Computing power spectra by means of the Discrete Fourier Transform

First, let us explain how to compute the power spectrum for a discrete signal. Let us assume that we have a time series consisting of the discrete sequence $x[0], x[1], \ldots, x[N-1]$. The Discrete Fourier Transform (DFT) of this sequence results in N complex components $X[0], X[1], \ldots, X[N-1]$ in the frequency domain,

defined as

$$X[k] = \sum_{n=0}^{N-1} x[n] \cdot e^{-i2\pi kn/N}. \tag{2.14}$$

$X[k]$ represents the complex amplitude of the angular frequency $\omega_k = \frac{2k\pi}{N}$ and satisfies $X[k] = X^*[N-k]$. The power spectrum of the discrete time series $x[n]$ at the frequency index k is given in terms of $X[k]$ as

$$P[\omega_k] = X[k]X^*[k]. \tag{2.15}$$

We now describe how the DFT represents the frequency domain of a continuous time series in order to understand the origin of the numerical errors associated with it.

Suppose we have a continuous signal $x(t)$ extending from $t \to -\infty$ to $t \to \infty$ whose Fourier transform $X(\omega) = \int_{-\infty}^{\infty} x(t)e^{i\omega t}$. Now, let $y(t)$ be a discretized version of $x(t)$, such that $y(t) = \sum_n \delta(t - n\Delta)x(n\Delta)$. Let us denote the $x(n\Delta)$ simply by $x[n]$. It is easy to see that $Y(\omega) = \sum_{n=-\infty}^{\infty} x[n]e^{i\omega n\Delta}$, the Fourier transform of $y(t)$, is a periodic function of ω with periodicity $\frac{2\pi}{\Delta}$. In fact, $Y(\omega)$ is the convolution of $X(\omega)$ and the function $\sum_n \delta(\omega - \frac{2n\pi}{\Delta})$.

We can see here the first problem which appears in the frequency domain, due to the discretization in the time domain. The original $x(\omega)$ was extending from $\omega = -\infty$ to $\omega = \infty$. When we "periodicize" $x(\omega)$, which we assume decays to zero for $|\omega| \to \infty$, the high frequency tails will overlap with each other at the edges of the frequency window $[-\frac{\pi}{\Delta}, \frac{\pi}{\Delta}]$. This problem is called aliasing. To avoid this problem, the frequency window $[-\frac{\pi}{\Delta}, \frac{\pi}{\Delta}]$ should be very large, which means that Δ is very small and the sampling frequency in time domain is very large with respect to the frequency content of $x(\omega)$. When this condition is not fulfilled, the aliasing problem mentioned above will become significant.

If, for practical purposes, the signal $x(t)$ (and consequently the sequence $x[n]$) is truncated to a finite length $N\Delta$ (N), then this sharp truncation will affect the high frequency components of $X(\omega)$ ($Y(\omega)$) and will introduce additional tails at high frequencies even if $x(t)$ originally represented a single sinusoidal wave. This problem is called spectral leakage.

Finally, in order to have a discrete representation in the frequency domain, we assume that the truncated sequence $x[n]$ is repeated periodically, with period N, such that $x[n] = x[n + N]$. We now show that this construction will have the effect of making $Y(\omega)$ discrete in frequency. Only the values of $Y(\omega)$ at frequencies

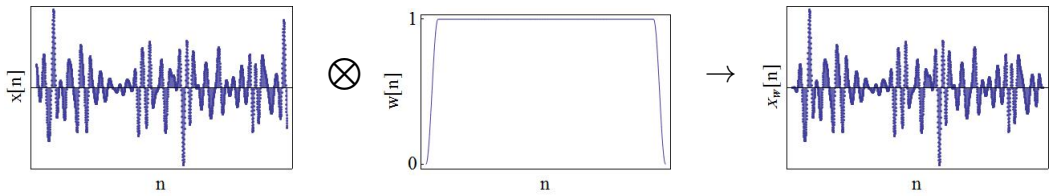

Figure 2.5: The time series is pre-processed by multiplying it by a window function to mitigate spectral leakage effects before computing its power spectrum.

which are multiples $\frac{2\pi}{N\Delta}$ will remain, and all other components will average out. To see this, let $\omega = \frac{2\pi k}{N\Delta}$, where k is a real number, and $n = m + Ns$ where m is an integer in the range $[0, N-1]$ and s is an integer from $-\infty$ to ∞. $Y(\omega)$ can be expressed as

$$Y(\omega) = \sum_{m=0}^{N-1} \sum_{s=-\infty}^{\infty} x[m+Ns] e^{\frac{2\pi i k m}{N}} e^{2\pi i k s} \tag{2.16}$$

$$= \left[\sum_{m=0}^{N-1} x[m] e^{\frac{2\pi i k m}{N}} \right] \left[\sum_{s=\infty}^{\infty} e^{2\pi i k s} \right]. \tag{2.17}$$

For non-integer k, the second bracket in 2.17 will average out, and $Y(\omega)$ will have nonzero value only for integer k, which is equal to $X[k]$ defined in 2.14.

The spectral leakage becomes particularly strong when there is mismatch between the end points of the time series. For example, the DFT representing a sinusoidal time series terminated at the same phase as the starting point is different than the DFT for a time series terminated at a different phase. To mitigate the spectral leakage problem, the discrete time series is multiplied by a window function that smoothly diminishes the values of $x[n]$ at the boundaries as illustrated in Fig. 2.5. The window we use is called the "Tukey window" [63, 64], sometimes also referred to as a ten percent window. It is defined as

$$w[i] = 0.5 \left(1 - \cos \left(\frac{2\pi i}{0.1N} \right) \right) \text{ for i=0 to } 0.05\ N,$$

$$w[i] = 1 \text{ for i=}0.05N \text{ to } 0.95\ N, \text{ and}$$

$$w[i] = 0.5 \left(1 - \cos \left(\frac{2\pi (i-N)}{0.1N} \right) \right) \text{ for i=}0.95\ N \text{ to } N, \tag{2.18}$$

where N is the length of the time series.

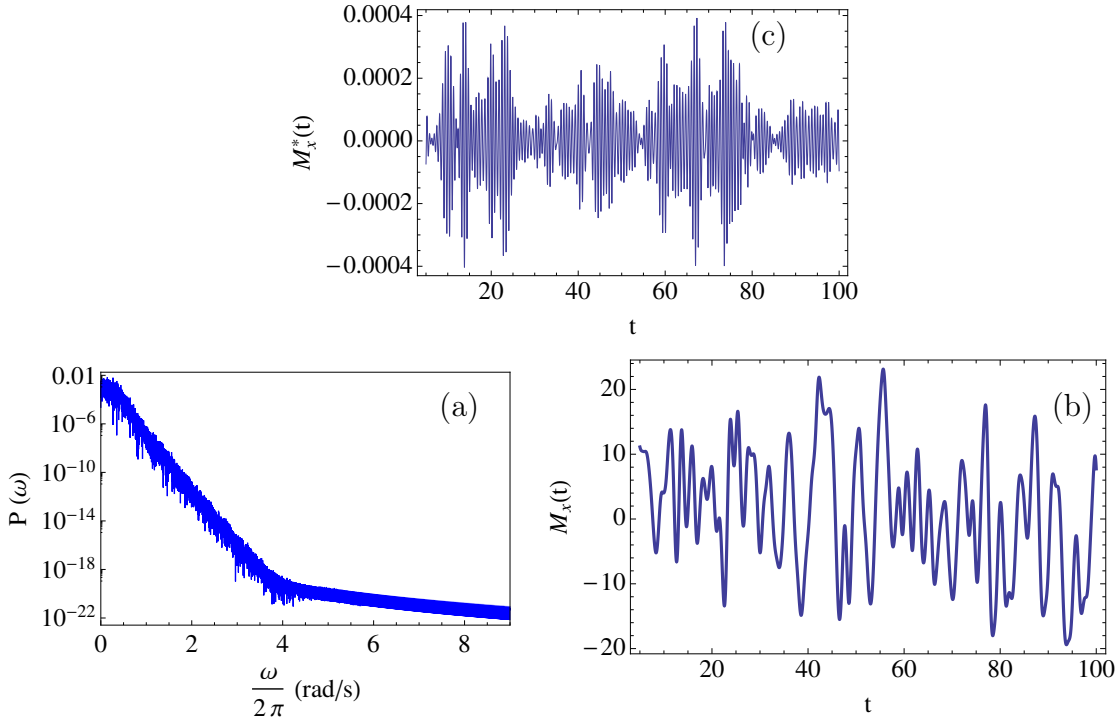

Figure 2.6: (a) Power spectrum $P(\omega)$ for nonintegrable classical spin lattice consisting of $6 \times 6 \times 6$ spins with nearest neighbor coupling coefficients $J_x = -0.65, J_y = -0.3$ and $J_z = 0.7$ computed for a time series representing the total magnetization in the x-direction of length $T = 1000$. The initial conditions are selected randomly from the infinite temperature ensemble. (b) A segment of the time series for which $P(\omega)$ is shown in (a). (c) The same as in (b) after applying a high-pass filter with a corner frequency at 1.5 Hz.

2.2.2 Exponential tails of power spectra of chaotic systems

We now use the DFT procedure with the Tukey window to compute the power spectrum of the nonintegrable classical spin system defined in section 2.1. We have used a time series of length $T = 1000$ generated by selecting a random initial condition picked from the infinite temperature ensemble. The result is shown in Fig. 2.6-a on a semi-log scale. It is clear that $P(\omega)$ exhibits a long exponential tail at high frequencies. The level at which this tail stops is determined by the spectral leakage of the discretized time series and the level of noise in the time series.

Exponential tails were confirmed to exist in the power spectra of other chaotic systems [65–68]. The existence of this exponential tail is considered to be a consequence of the complex time singularities that exist when the solution of the equations of motion is analytically continued to the complex time plane. The

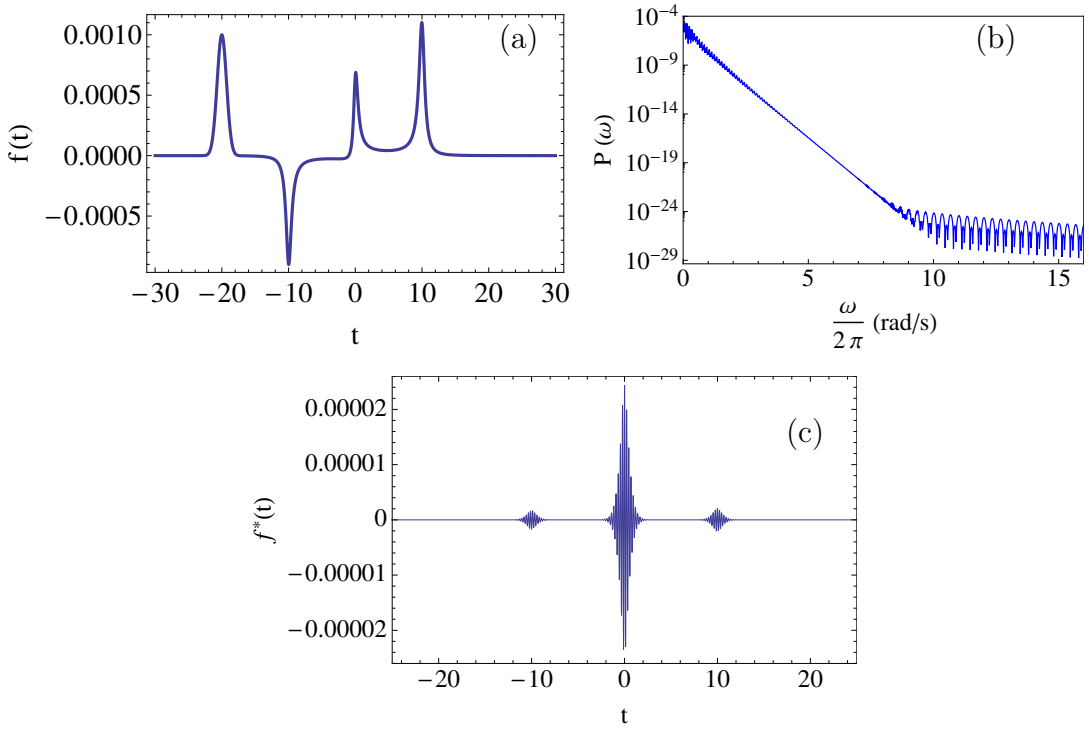

Figure 2.7: (a) A plot of $f(t) = 10^{-3}e^{-(x+20)^2} + \frac{x^2+0.15}{x^4-199.5x^2+10050.1}$ (b) Power spectrum for $f(t)$. (c) The function $f(t)$ after being filtered with a high-pass filter with corner frequency at 4.2 Hz.

close connection between real-time behavior of dynamical systems and the singularities of their solution in the complex time plane was investigated in Refs. [69–71]. It was found that chaotic signals contain bursts of high frequency fluctuations at the real parts of those complex time singularities. These bursts can be revealed as an intermittent behavior when letting the chaotic signals pass through a high-pass filter (a filter which passes only high frequencies) [70]. For more on the connection between complex time singularities and the exponential tail in the power spectrum, we refer the reader to [72]. In Fig. 2.6-b, we show the bursty behavior of the time series of the chaotic spin system filtered with a high-pass filter with corner frequency at 1.5 Hz.

We demonstrate numerically this connection by analysing the power spectrum of the function $f(t) = 10^{-3}e^{-(x+20)^2} + \frac{x^2+0.15}{x^4-199.5x^2+10050.1}$ plotted in Fig. 2.7-a. This function was chosen to have singularities at $t = \pm 0.387i$, $t = 10 \pm 0.5i$ and $t = -10 \pm 0.5i$. These singularities give rise to the exponential tail in its power spectrum as shown in Fig. 2.7-b. We further see in Fig. 2.7-c that after filtering out the low frequency part of $f(t)$, three bursts of high frequency appear around the real parts of the complex time singularities. Since the exponential tail is

mainly controlled by the singularities closest to the real-time axis, we notice that the amplitude of the high frequency bursts at $t = 0$ is larger than the bursts at $t = \pm 10$.

We have confirmed the existence of the exponential tail in the power spectrum in other nonintegrable dynamical systems and systems of nonlinear differential equations (e.g., Lorenz and Rössler systems). In some other systems (e.g., anisotropic Kepler problem [73]) the power spectrum will have a long tail, but not necessarily decaying in a pure exponential manner as in the former cases. We provide details of those systems and other systems in section 2.4.

2.2.3 Power spectra of integrable systems

Power spectra of integrable systems are typically terminated faster than exponentially. An integrable system consisting of N degrees of freedom possesses by definition N integrals of motion. In the language of the action-angle variables, the motion of the system can be described as a precession on the surface of an N-dimensional torus, with fixed frequencies. Therefore, while the power spectrum of chaotic motion is continuous [74], the power spectrum of any time series produced by an integrable system consisting of a finite number of degrees of freedom consists of discrete frequencies. We confirm this statement by computing the power spectrum for an Ising classical spin lattice consisting of $6 \times 6 \times 6$ spins. As shown in Fig. 2.8, the power spectrum is sharply terminated, and consists of discrete frequencies.

Since the dynamics of the Ising system is trivially multi-periodic, we investigated several non-trivial integrable few-body and many-body systems and noticed the absence of the long exponential tail in their power spectra. The details of those systems are given in section 2.4. One notable exception is the Toda lattice, which is treated in more depth in the same section.

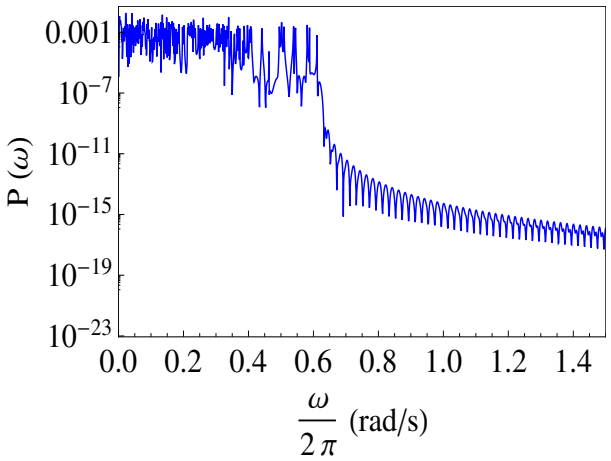

Figure 2.8: Power spectra for an Ising classical spin system consisting of $6 \times 6 \times 6$ spins, computed for a time series representing the total magnetization in the x-direction of length $T = 1000$.

2.2.4 Finite temperatures and the transition to integrability

Two interesting issues that are worth investigating here are:

1. How is the exponential tail in a chaotic many-particle system affected by selecting initial conditions corresponding to lower temperature?

2. How is the exponential tail affected by changing the parameters of the system gradually towards the integrability limit?

We investigate the first issue in Fig. 2.9. By selecting initial conditions corresponding to gradually increasing absolute energy per spin, and hence approaching the zero temperature limit[2], we obtained power spectra whose exponential tails exhibit humps and valleys at specific frequencies. The origin of this behavior is not clear to us.

On the other hand, as we change the coupling coefficients, approaching the integrable Ising limit, the exponential tail becomes attenuated, but keeps the same slope, until it vanishes completely at the Ising limit. This behavior is shown in Fig. 2.10. To obtain this plot, the maximum coupling constant, $\max[|J_x|,|J_y|,|J_z|]$, is varied while keeping $J_x^2 + J_y^2 + J_z^2 = 1$. For the parameters used in this plot, the maximum Lyapunov exponent decreases by two orders of magnitude during

[2]At infinite temperature, each spin is randomly oriented and the average interaction energy between any spin and its local field from the other spins is zero. The opposite occurs at low temperatures.

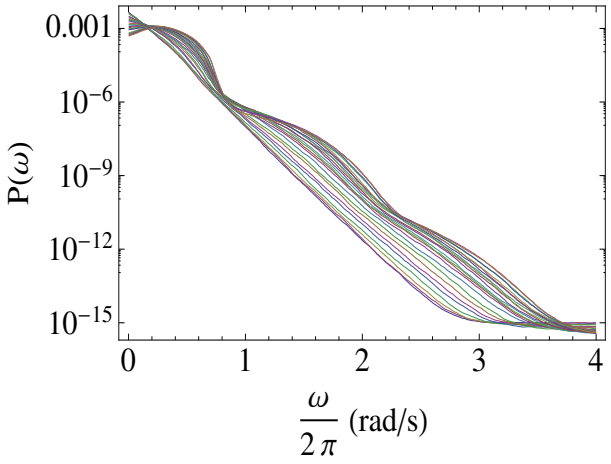

Figure 2.9: Power spectra for a 3D classical spin system with nearest neighbor coupling coefficients $J_x = 0.873, J_y = -0.436$ and $J_z = 0.218$ for various temperatures. The upper curve corresponds to very low temperature (energy per spin = 2.3) while the lowest curve corresponds to infinite temperature (energy per spin =0). The power spectra were smoothed out to reduce the fluctuations that show up in Fig. 2.6.

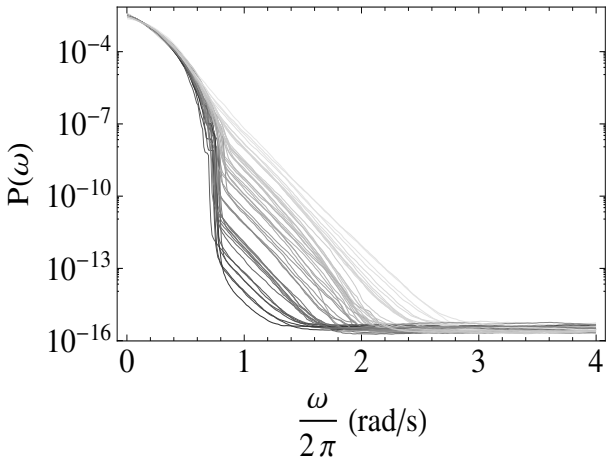

Figure 2.10: Power spectra at infinite temperature for 50 randomly selected realizations of J_x, J_y, J_z in the proximity of the Ising limit subject to the constraint $J_x^2 + J_y^2 + J_z^2 = 1$. The corresponding maximum Lyapunov exponent varies over two orders of magnitude [19]. The Lyapunov exponents decrease monotonically from the upper (light gray) plots to the lower (dark gray) plots [1]. The power spectra were smoothed out to reduce the fluctuations that show up in Fig. 2.6.

the convergence to the Ising limit, while, as seen in Fig. 2.10, the slope of the exponential tail remains nearly the same [3].

[3]The maximum Lyapunov exponents were computed by Astrid de Wijn.

2.2.5 Power spectra of quantum spin systems

After having discussed the power spectra of integrable and nonintegrable classical spin systems, it is natural to investigate the power spectra of the analogous quantum spin systems. Of course, for a finite quantum system, the spectrum is always discrete in both cases, unlike the case of chaotic classical spin system. Therefore, we are concerned here with the overall shape of the spectrum, namely whether the existence of exponential tails at high frequencies distinguishes nonintegrable systems from integrable ones.

Exponential tails were confirmed to exist in the wings of the NMR spectral lines solids such as CaF_2 [75]. These lines represent the Fourier transform of the free induction decay signal (see chapter 5).

We present in Fig. 2.11 the power spectra of four quantum spin lattices, integrable and nonintegrable, computed from the time series of the expectation value of the total magnetization operator in the x direction M_x at equilibrium. The results presented in Fig. 2.11 imply that both types of systems can have a long tail of (discrete) frequencies in their spectra.

We present the power spectra of two nonintegrable models in Figs. 2.11-a and 2.11-b. The first case is an XYZ spin chain with both nearest neighbor and next-nearest neighbor interaction and we see clearly the signature of an exponential tail in its spectrum. The second case is a nonintegrable 2D quantum spin lattice with XXZ coupling coefficients. We notice, however, that the tail of the power spectrum is not purely exponential. This case may require further investigation to exclude finite-size effects.

In Fig. 2.11-c, we show the power spectrum for an integrable XX spin chain. We observe that the power spectrum of this model is a Gaussian function of frequency. This result is expected since the correlation function $\langle M_x(t)M_x\rangle$ is Gaussian [76]. In chapter 3, we show analytically and numerically that the correlation function of the equilibrium noise of $\langle\psi(t)|M_x|\psi(t)\rangle$, whose Fourier transform yields the power spectrum, approaches the quantum correlation function $\mathrm{Tr}\{M_x(t)M_x\}$ in the thermodynamic limit. The second integrable model we consider is the Bethe ansatz integrable XXZ spin chain, whose power spectrum is shown in Fig. 2.11-d. We notice that its power spectrum has an exponential tail. However, for this particular case, it was found that the long-time behavior of its correlation function exhibits an exponential tail, a phenomenon intimately related to chaotic dynamics [13].

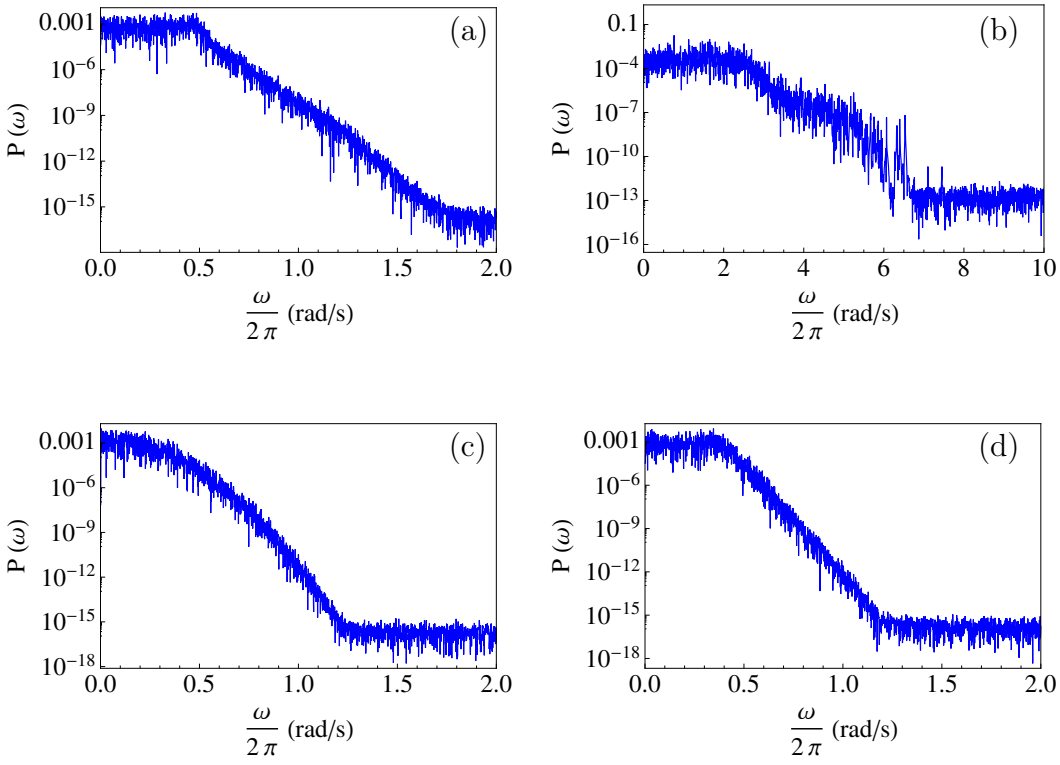

Figure 2.11: Power spectra for different quantum spin 1/2 systems. The time series represent $\langle \hat{M}_x \rangle$, and have length $T > 2000$. The initial state is selected randomly from an infinite temperature ensemble. The systems are: (a) 16-spin chain, with nearest neighbor coupling coefficients $J_x = 1.0/\sqrt{14.0}$, $J_y = 2.0/\sqrt{14.0}$ and $J_z = -3.0/\sqrt{14.0}$ and next nearest neighbor coupling of strength 30% of the nearest neighbor coupling. (b) a 2D lattice consisting of 5×4 spins with XXZ coupling coefficients $J_x = \sqrt{3.0/16.0}$, $J_x = \sqrt{3.0/16.0}$ and $J_z = -\sqrt{1.0/8.0}$ (c) a 1D lattice consisting of 16 spins with XX coupling coefficients $J_x = 1/\sqrt{2.0}$, $J_x = 1/\sqrt{2.0}$ and $J_z = 0$ (d) a 1D lattice consisting of 16 spins with XXZ coupling coefficients $J_x = \sqrt{3.0/8.0}$, $J_x = \sqrt{3.0/8.0}$ and $J_z = -0.5$. Models (c) and (d) are integrable in the thermodynamic limit.

2.3 Higher order derivatives: A new tool for discriminating chaotic from nonchaotic behavior

We noticed in the previous section that the time series produced by finite integrable spin systems have sharply terminated spectra, while those produced by nonintegrable spin systems exhibit continuous frequency spectra with long exponential tails. In this section, we exploit this observation in order to introduce new methods to discriminate between integrable and nonintegrable systems from time series analysis, or improve on existing methods. The basic idea is to take the high-order time derivatives of the time series under investigation. For both integrable and nonintegrable time series, taking derivatives will progressively suppress the low frequency parts of their spectra with respect to the high frequency parts. For the integrable case, this suppression will have the effect of reducing the entropy per unit time since the spectrum has a well-defined maximum frequency, even in the thermodynamic limit. On the other hand, for the nonintegrable case, the entropy generated by the time series will not decrease by differentiation since its power spectrum extends to infinity and differentiation will shift the bulk of the spectrum to higher frequencies. The high frequency bursts embedded in a chaotic time series will become amplified upon taking derivatives, giving rise to a broader spectrum (i.e., bigger full width at half maximum-FWHM).

In fact, the statistical properties of the time series and its power spectrum and consequently the visual appearances become different for integrable and chaotic systems upon taking higher order derivatives even though the original signals might be indistinguishable. As a consequence, the distinction between the integrable and nonintegrable systems is better manifested in the behavior of their respective numerically calculated entropy rates when their physical signals are subjected to differentiation. This is particularly important when the finite length of the time series is not long enough to extract the true values of the entropy rates.

When the length of the available time series is too short, visual comparison between the original signal and its higher order derivative and their respective power spectra may be a quick and handy way to determine whether the underlying dynamical system is integrable or nonintegrable. Of course, this approach requires the time series to be very accurately measured, i.e., the level of noise is very low. We comment on this aspect later in this section.

In Fig. 2.12, we present segments of the time series of chaotic and integrable

classical spin systems together with their $7^{\underline{\text{th}}}$ order derivatives. We see from this figure that while both time series are almost indistinguishable, the integrable time series becomes more regular after taking the $7^{\underline{\text{th}}}$ order derivative while the chaotic time series becomes more erratic and bursty. In Appendix 2.6, we present all the time derivatives of the two time series up to the $9^{\underline{\text{th}}}$ order derivative. The numerical noise concealed within the data limits the order of the highest derivative we can take. In our computer simulation, we are limited by the rounding errors of the double precision numbers.

The exponential tail of the power spectrum of chaotic spin system that has the form $P(\omega) \approx e^{-\gamma|\omega|}$ implies that the power spectrum of the $\text{n}^{\underline{\text{th}}}$ derivative for sufficiently large n has the form,

$$P^{(n)}(\omega) \cong \omega^{2n} e^{-\gamma|\omega|}. \tag{2.19}$$

We plot the fitting of $P^{(7)}(\omega)$ for the chaotic time series with a function of the form $\omega^{14}e^{-\gamma|\omega|}$ in Fig. 2.12-e. In contrast, the power spectrum for the Ising spin lattice is sharply terminated. Therefore, taking higher order derivative in time domain makes the power spectrum peaked around a maximum frequency, which represents the carrier frequency of the $7^{\underline{\text{th}}}$ order derivative in Fig. 2.12-d. The modulation frequency of $M_x^{(7)}$ is controlled by the width of the peak.

We propose two criteria to quantify the differences in time and frequency domains between the chaotic and integrable time series. The first criterion is related to the observation that the root mean square (RMS) value of the derivatives, denoted as $M_{rms}^{(n)}$, in the chaotic time series is larger than the integrable time series by an order of magnitude. In Fig. 2.13(a), we plot the quantity $R_n \equiv M_{rms}^{(n)}/M_{rms}^{(n-1)}$ as a function of n. We see clearly that while R_n saturates for the integrable system, it increases monotonically for the chaotic spin system.

The second criterion is related to the widths of the power spectra of the derivatives. We quantify this width by the square root of the variance for the positive-ω part of $P^{(n)}(\omega)$ denoted as v_n (v_0 corresponds to $P(\omega)$). In Fig. 2.13(b), we plot $W_n \equiv v_n/v_0$ for the two systems considered. The distinction between the two systems is again apparent. The relative width of the power spectrum for the chaotic system increases with the order of the derivative, while, for the integrable system, it decreases monotonically.

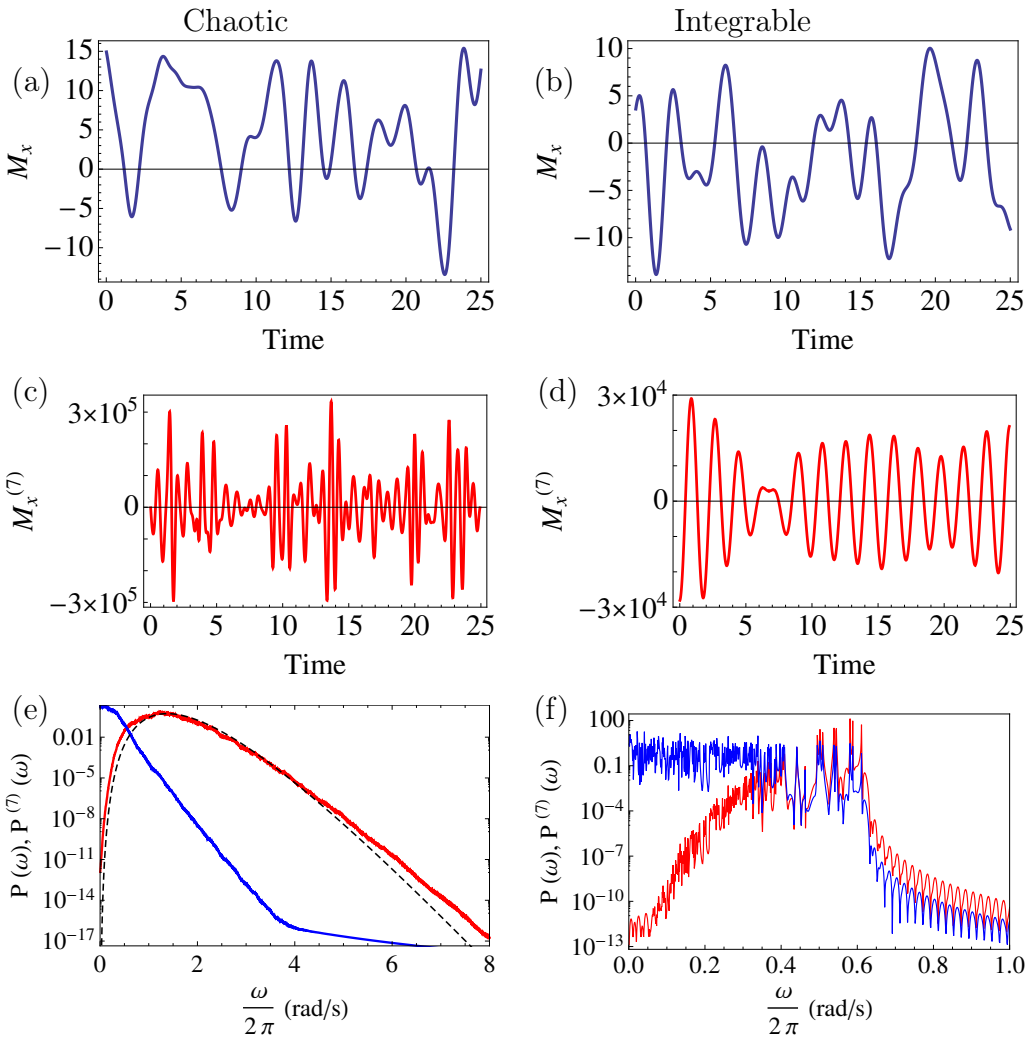

Figure 2.12: (a,b) Segments of the time series $M_x(t)$ for $6\times6\times6$ spin lattices. (c,d) The corresponding $7^{\underline{\text{th}}}$ order time derivatives $M_x^{(7)}(t)$. (e, f) The power spectra $P(\omega)$ (blue) and $P^{(7)}(\omega)$ (red) computed for a total length $T = 1000$. The figures in the left column correspond to the chaotic system with coupling coefficients $J_x = -0.65, J_y = -0.3, J_z = 0.7$ while the figures in the right column represent for the integrable system with coupling coefficients $J_x = J_y = 0$ and $J_z = 1$. The black dashed line in (e) represents the fitting of $P^{(7)}(\omega)$ to a function of the form $\alpha\,\omega^{14}e^{-\gamma\omega}$ where α is a fitting parameter and γ is the high-frequency exponential decay constant for $P(\omega)$. The power spectra for the chaotic system in (e) have been smoothed out. The tails of the power spectra at $\omega/2\pi > 4$ in (e) and $\omega/2\pi > 0.6$ in (f) are affected by the spectral leakage problem.

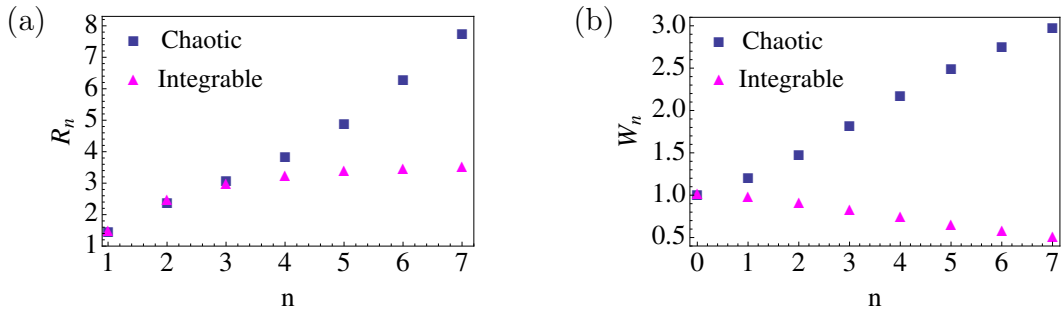

Figure 2.13: New discriminators that characterize the differences in the time derivatives $M_x^{(n)}(t)$ and their power spectra of time series corresponding to integrable and chaotic systems. (a) Ratios R_n of the RMS value of $M_x^{(n)}(t)$ to the RMS value of $M_x^{(n-1)}(t)$; (b) Relative width W_n of the power spectrum $P^{(n)}(\omega)$ with respect to the width of $P(\omega)$ [1].

We now consider how to exploit the qualitative differences in time domain and frequency domain to improve the negative results of the rate of the (ϵ, τ)-entropy production presented in section 2.1 in discriminating between the integrable and chaotic time series. The observation that the integrable time series becomes more regular upon taking the higher-order derivatives already gives a hint that its rate of entropy production decreases as the order of the derivatives increases, unlike the chaotic time series. We test this proposition in Fig. 2.14 where the rates of Cohen-Proccacia entropy production $h_{CP}(\epsilon, 0.1, 10)$ for both the $7^{\underline{\text{th}}}$ order derivative and the original time series are plotted. We notice that while $h_{CP}(\epsilon, 0.1, 10)$ for the integrable system is reduced after taking the time derivative, that of the chaotic system is not. In other words, it is the incremental behavior of the CP (ϵ, τ) rate of entropy production under taking the derivatives of the time series which makes a recognizable difference when the length of the time series is finitely small rather than the absolute value of the $h_{CP}(\epsilon, \tau, N)$.

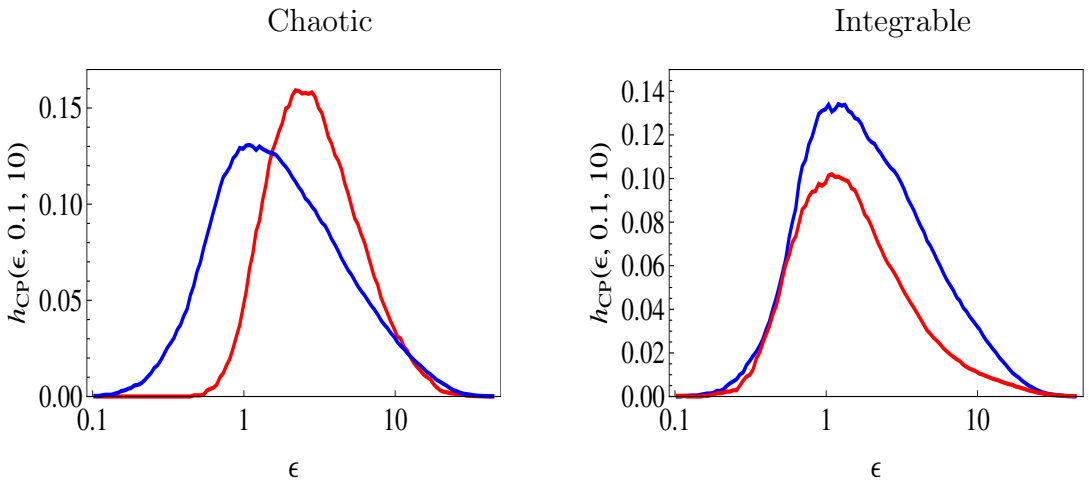

Figure 2.14: $h_{CP}(\epsilon, \tau, 10)$ calculated for both $M_x(t)$ [blue] and $M_x^{(7)}(t)$ [red] for both chaotic and integrable systems. The values of ϵ for $h_{CP}(\epsilon, \tau, 10)$ associated with the $7^{\underline{\text{th}}}$ derivative were rescaled by dividing the true values by the following factors: 1.13×10^4 in the chaotic case and 1.31×10^3 in the integrable case. These factors were chosen such as to make the spread between the maximum and the minimum values of $M_x^{(7)}(t)$ equal to that of the corresponding $M_x(t)$, thereby, compensating for the different dimensions of $M_x(t)$ and $M_x^{(7)}(t)$. The value of τ is taken to be 0.1 in both figures [1].

2.3.1 Very short time series

Let us illustrate the effectiveness of this method applied to very short segments of data produced by the integrable and chaotic spin systems. In Fig. 2.15, we show the results obtained for a 4×4 square spin lattice. Detecting chaos from such a short time series using conventional techniques is an almost impossible task. However, after taking the $7^{\underline{\text{th}}}$ time derivatives and comparing the time series and power spectra of both the original signals and their derivatives, we observe a significant difference between the chaotic and integrable systems. The power spectrum becomes broader and the time series becomes more random for the chaotic system. On the other hand, the power spectrum of the integrable system does not become broader and the time series becomes more regular.

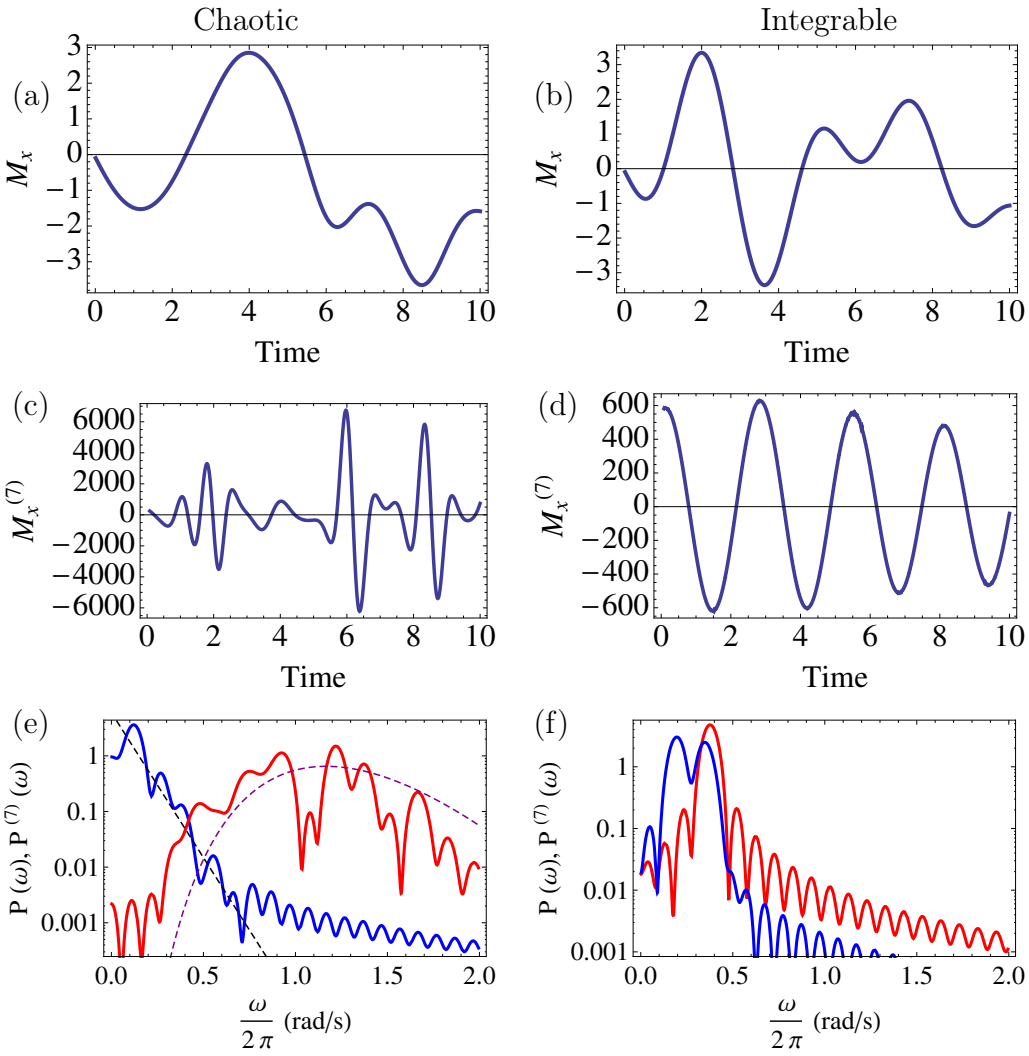

Figure 2.15: Time series of the magnetization for a chaotic spin system (a) and an integrable system (b) consisting of 4×4 spins and the $7^{\underline{\text{th}}}$ order derivative of both systems (c) and (d) respectively. (e) and (f) illustrate the power spectra of the original signals (blue) and their $7^{\underline{\text{th}}}$ order derivatives (red). The black dashed line depicts fitting the power spectrum of the nonintegrable system with $\alpha\ e^{-\gamma\omega}$ while the purple dashed line depicts $\beta\,\omega^{14}e^{-\gamma\omega}$, α, β and γ are fitting parameters.

2.3.2 Effects of noise and inaccurate measurements of the time series

In general, the effect of noise poses a considerable limitation on one's ability to compute high-order time derivatives and, therefore, on the ability to distinguish between integrable and chaotic systems. Here, we give estimates of the acceptable level of noise in order for the technique described above to work properly and show for one example how to deal with the white noise.

Consider a chaotic time series with a long exponential tail in its power spectrum given by $P(\omega) = P_0\ e^{-\Gamma\omega}$. Let us further assume that the measured time series includes an additive white noise of power Q_0. The cutoff frequency at which the noise spectrum will interfere with the exponential tail is given by $\omega_c = \frac{1}{\Gamma}\log\frac{P_0}{Q_0}$. The frequency at which the power spectrum of the $n^{\underline{th}}$ derivative has a maximum is given by $\omega_{max} = \frac{2n}{\Gamma}$. The effect of noise in our method will be tolerable as long as $\omega_{max} < \omega_c$, i.e., $\log(\frac{Q_0}{P_0}) < \frac{1}{2n}$.

The visual distinction between chaotic and integrable systems in Figs. 2.15-c, 2.15-d and Figs. 2.12-c, 2.12-d can be preserved in the presence of noise by filtering, as illustrated in Fig. 2.16. In Fig. 2.16 (a) and (b), we depict a noisy version of the time series in Fig. 2.12 using an additive Gaussian white noise having root mean square equal to unity, i.e., the power of the noise is approximately 60 times smaller than the power of the signal. In Fig. 2.16 (c) and (d), we illustrate the same time series after filtering out all frequencies higher than 1 Hz, compared to the noise-free time series. After taking the fourth-order derivatives of the filtered time series, we see in Fig. 2.16 (e) and (f) that the visual distinction between the chaotic and the integrable time series is better. Therefore, we propose that simply filtering the noisy time series before taking the time derivatives may remedy the effect of the noise.

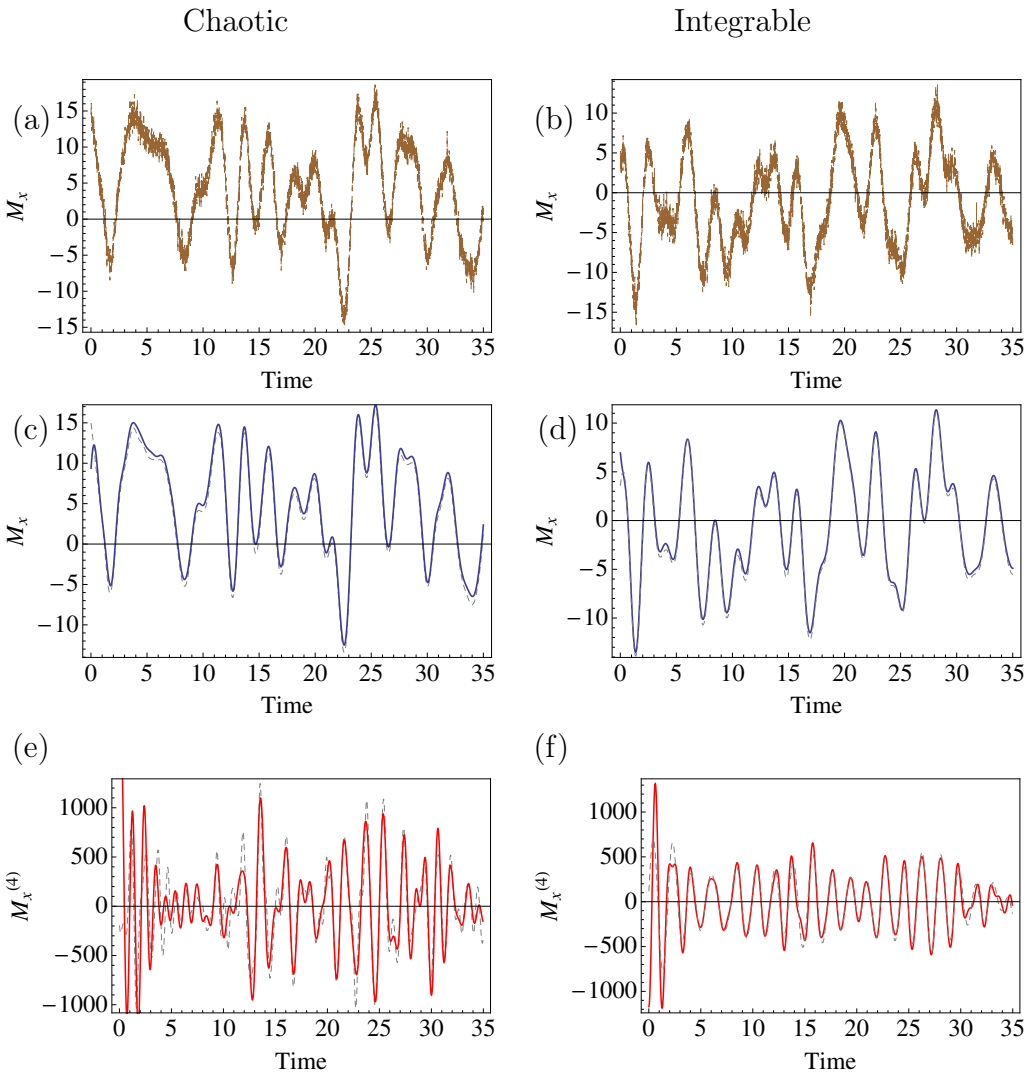

Figure 2.16: (a) and (b) represent noisy time series of $M_x(t)$ for $6 \times 6 \times 6$ spin lattices. The notations and system parameters are the same as in Fig. 2.12. (c) and (d) illustrate the same time series after being filtered at 1 Hz as compared to the noise-free time series in dashed gray. (e) and (f) illustrate the fourth-order derivatives of the filtered time series as compared to the noise-free derivatives of the time series in dashed gray [1].

2.4 Beyond spin systems: Power spectra for other chaotic and integrable systems

In this part, we illustrate the power spectra of several chaotic and integrable systems, other than classical spin lattices, to verify the claim that an exponential tail in the power spectrum is a hallmark of nonintegrable systems.

In tables 2.1 and 2.2, we list several dynamical systems and chaotic attractors for which we compute the power spectra and present sample time series for one of their variables in Figs. 2.17 and 2.18 respectively. For all of these systems, except for model (F)[4], pronounced exponential tails appear at high frequencies of the power spectra.

On the other hand, we present in Table 2.3 a list of completely integrable models for which the power spectra are shown in Fig. 2.19. We notice the absence of the exponential tail in all of the cases except for the periodic Toda lattice [2], which we will investigate in more details in rest of this section.

[4]We do not have an explanation for this case.

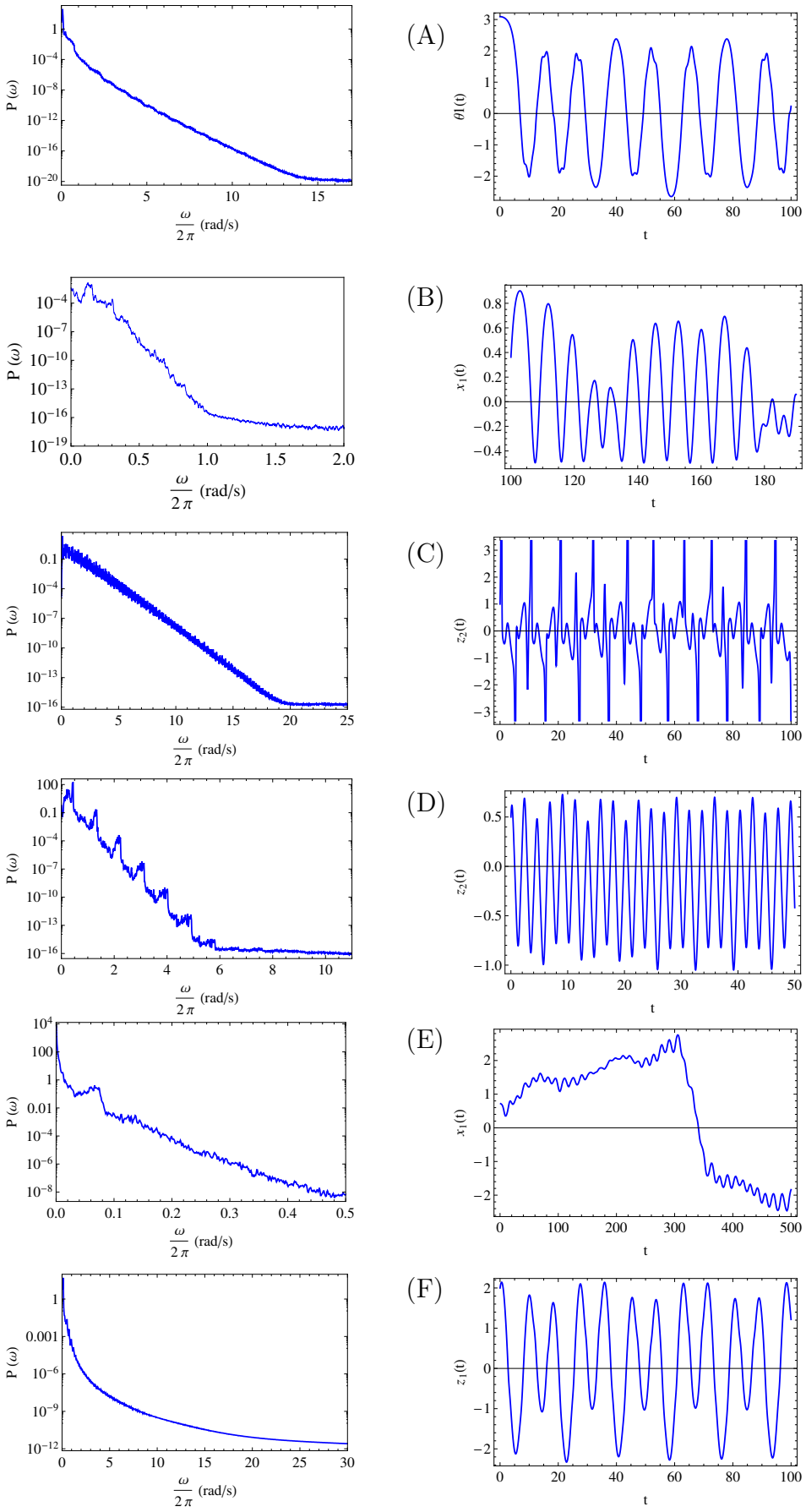

Figure 2.17: Power spectra for the list of chaotic systems described in Table 2.1 (left) and sample time series (right). The spectra have been smoothed out for better visibility of the exponential tails. The variables for which the time series are computed are indicated on the vertical axes.

System	Equations of motion/Hamiltonian/Lagrangian	λ_{max}
A- Double pendulum [77]	$\mathcal{L} = \frac{1}{2}[l_1^2(m_1+m_2)\dot{\phi_1}^2 + l_2^2 m_2 \dot{\phi_2}^2 + 2l_1 l_2 m_2 \times$ $\cos(\phi_1-\phi_2)\dot{\phi_1}\dot{\phi_2}] + g l_1(m_1+m_2)\cos\phi_1 + g l_2 m_2 \cos\phi_2$ $m_1=3,\ m_2=1,\ l_1=2,\ l_2=1,\ g=1,\ \theta_2(0)=0$ $\theta_2(0) = \arccos(-7.99/8.0)$	0.179
B- Hénon-Heiles system [78]	$H = \frac{1}{2}(p_1^2+p_2^2+q_1^2+q_2^2) + q_1^2 q_2 - \frac{1}{3}q_2^3$ $p_1=0.5542,\ p_2=0,\ q_1=0$ and $q_2=-0.15$	0.148
C- Driven van der Pol oscillator [73]	$\frac{d}{dt}\begin{pmatrix} z_1 \\ z_2 \end{pmatrix} = \begin{pmatrix} z_2 \\ -d(1-z_1^2)z_2 - z_1 + b\ \cos\omega t \end{pmatrix}$ $d=-5,\ b=5,\ \omega=2.47, z_1(0)=-1$ and $z_2(0)=1$	0.0985
D- Coupled quartic oscillators [73]	$\frac{d}{dt}\begin{pmatrix} z_1 \\ z_2 \\ z_3 \\ z_4 \end{pmatrix} = \begin{pmatrix} z_3 \\ z_4 \\ -(4z_1^3 + 2\alpha z_1 z_2^2) \\ -(4z_2^3 + 2\alpha z_2 z_1^2) \end{pmatrix}$ $\alpha=8,\ z_1(0)=0.8,\ z_2(0)=0.5,\ z_3(0)=1,$ and $z_4(0)=1.3$	0.1892
E- Coupled map lattice [79]	$(x_i,p_i) \mapsto (x_i',p_i') \quad i=1,2,\cdots,N$ $p_i' = p_i + \frac{K}{2\pi\sqrt{N-1}}\sum_{j=1}^{N}\sin 2\pi(x_j-x_i)$ $x_i' = x_i + p_i',\ N=16$ and $K=0.1$ x_i initially random, $\lvert p_i\rvert \ll 1$	0.65
F- Anisotropic Kepler problem [73]	$\frac{d}{dt}\begin{pmatrix} z_1 \\ z_2 \\ z_3 \\ z_4 \end{pmatrix} = \begin{pmatrix} z_3 + (\gamma-1)z_1\frac{(z_1z_3-z_2z_4)}{(z_1^2+z_2^2)} \\ z_4 + (\gamma-1)z_2\frac{(z_1z_3-z_2z_4)}{(z_1^2+z_2^2)} \\ 2Ez_1 - (\gamma-1)\frac{(z_3^2z_1z_2^2+z_2z_3z_4(z_1^2-z_2^2)-z_2^2z_1z_4^2)}{(z_1^2+z_2^2)} \\ 2Ez_2 - (\gamma-1)\frac{(z_4^2z_2z_1^2+z_1z_3z_4(z_1^2-z_2^2)-z_1^2z_2z_3^2)}{(z_1^2+z_2^2)} \end{pmatrix}$ $\gamma=0.61,\ E=-0.275,\ z_1(0)=1,\ z_2(0)=2,\ z_3(0)=1,$ and $z_4(0)=0.5$	0.138

Table 2.1: The list of chaotic systems, other than classical spin clusters, considered in this chapter in order to verify the existence of an exponential tail in their power spectra.

Chaotic Attractor	Equations of motion	Parameter Values	Initial Conditions	λ_{max}
I- Lorenz Attractor	$\dot{x} = \sigma(y - x)$ $\dot{y} = x(\rho - z) - y$ $\dot{z} = xy - \beta z$	$\sigma = 16$ $\rho = 45.92$ $\beta = 4$	$x(0) = 0$ $y(0) = 1$ $z(0) = 1$	1.497
II- Rossler Attractor	$\dot{x} = -(y + z)$ $\dot{y} = x + ay$ $\dot{z} = b + z(x - c)$	$a = 0.15$ $b = 0.2$ $c = 10$	$x(0) = 0$ $y(0) = -6.78$ $z(0) = 0.02$	0.09
III- Rossler hyper-chaos Attractor	$\dot{x} = -(y + z)$ $\dot{y} = x + ay + w$ $\dot{z} = b + zx$ $\dot{w} = cw - dz$	$a = 0.25$ $b = 3$ $c = 0.05$ $d = 0.5$	$x(0) = -20$ $y(0) = 0$ $z(0) = 0$ $w(0) = 15$	0.11

Table 2.2: The list of chaotic attractors considered in order to verify the existence of exponential tail in their power spectra. The values of Lyapunov exponents are from [54]

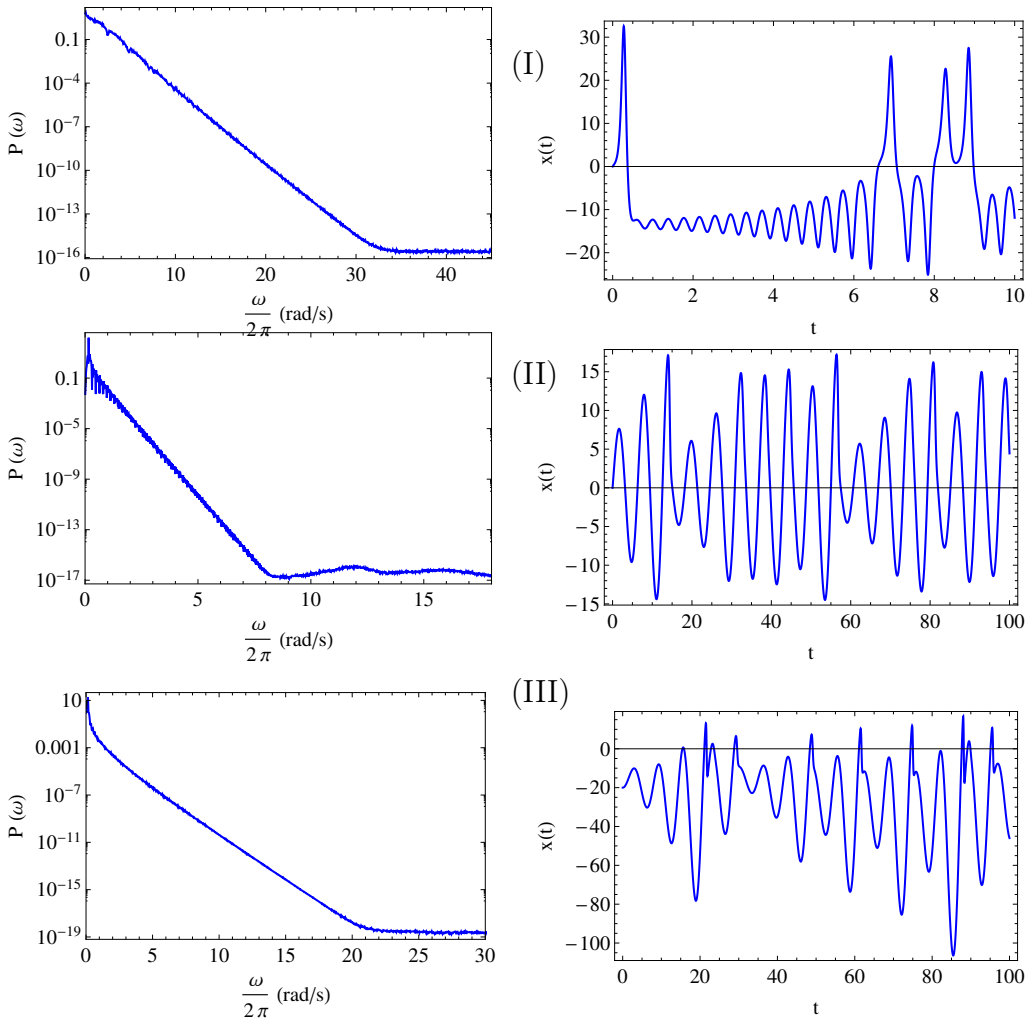

Figure 2.18: Power spectra for the list of chaotic attractors described in Table 2.2 (left) and sample time series (right).

Integrable System	Hamiltonian, Parameter Values and Initial Conditions
a- Double pendulum	Same as system (A) $\theta_1(0) = 0$ and $\theta_2(0) = \arccos(0.99)$
b- Coupled quartic oscillators	Same as system (D), $\alpha = 6$
c- Yoshida 3-particle system [80]	$H = \frac{1}{2}\left(p_1^2 + p_2^2 + p_3^2\right) + \frac{1}{2}\left(x_1^2 x_2^2 + x_1^2 x_3^2 + x_3^2 x_2^2\right)$
d- 6 particles interacting pairwise via potential $V(q_i, q_j)$ [81]	$V(q_i, q_j) = g^2 a^2 \sinh^{-2} a(q_i - q_j)$, $a = 0.5,\ g = -4$
e- 3 Coupled quartic oscillators in 2D [82]	$H = \frac{1}{2}\left(\sum_{i=1}^{3} p_{xi}^2 + \sum_{i=1}^{3} p_{yi}^2\right) + \left(\sum_{i=1}^{3} x_i^2\right)^2 + 12\sum_{i=1}^{3} x_i^2 \sum_{i=1}^{3} y_i^2 + 16\left(\sum_{i=1}^{3} y_i^2\right)^2$
f- 32 particles interacting via nearest neighbor potentials $V(q_i, q_{i+1})$ with periodic boundary conditions [2] (Toda lattice)	$V(q_i, q_{i+1}) = e^{-(q_i - q_{i+1})}$, random initial conditions.

Table 2.3: List of completely integrable systems considered, in order to verify the absence of an exponential tail in their power spectra.

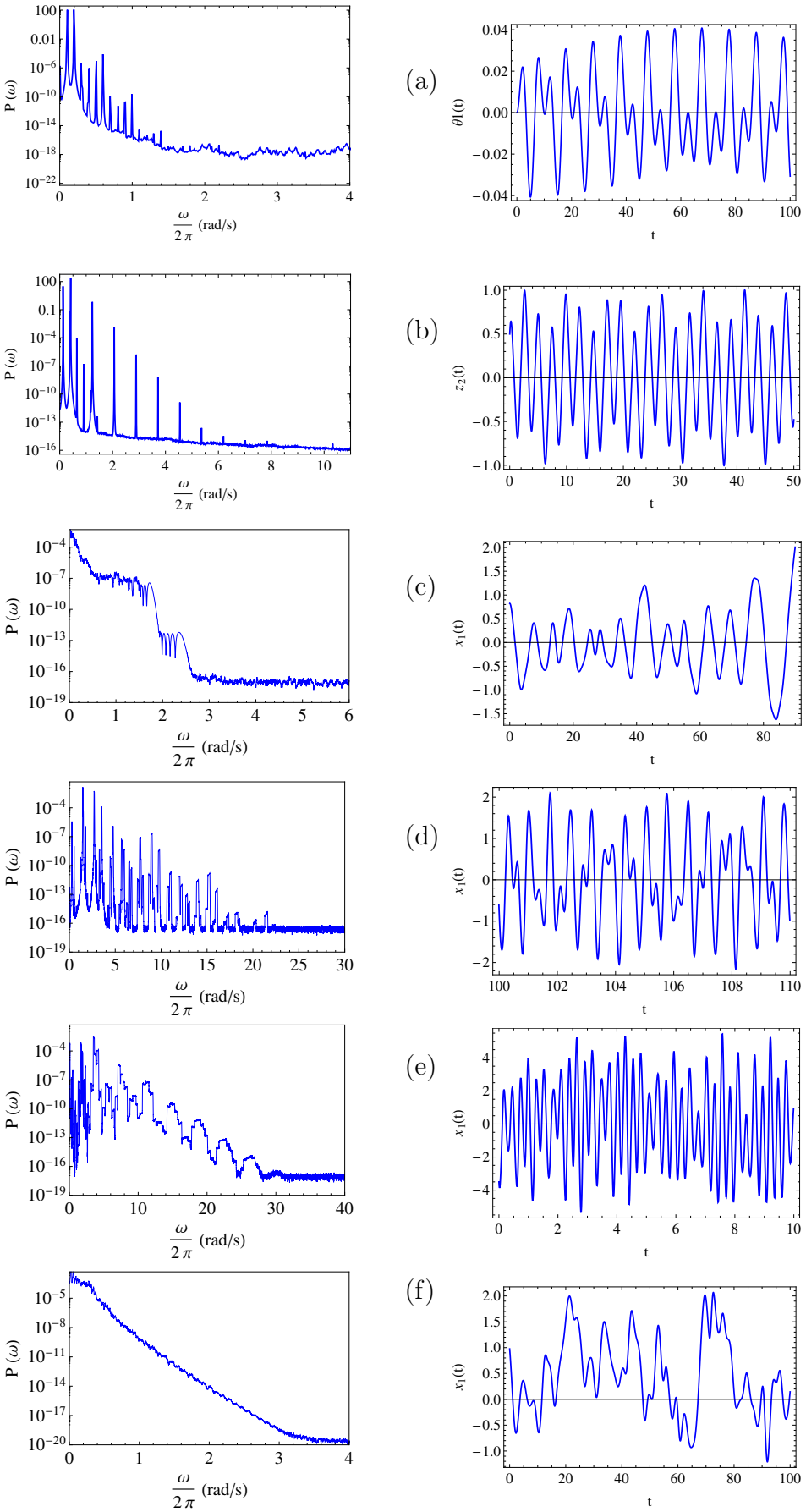

Figure 2.19: Power spectra for completely integrable systems listed in Table 2.3 (left) and the corresponding sample time series (right).

2.4.1 Toda lattice

The Toda lattice consists of N particles in one dimension interacting with the nearest neighbor[5] interaction potential $V(q_i, q_{i+1}) = c\ e^{-\alpha(q_i - q_{i+1})}$. We consider periodic boundary conditions and take $c = \alpha = 1$. The equations of motion have the form

$$\dot{q_i} = p_i \tag{2.20}$$

$$\dot{p_i} = e^{q_i - q_{i-1}} - e^{q_{i+1} - q_i}. \tag{2.21}$$

We illustrate the integrability of the Toda lattice numerically by two methods. First, we compute the maximum Lyapunov exponent, as described in chapter 1. We show in Fig. 2.20 that $\lambda_{max}(t_N)$ decays steadily at large N as a power law, indicating a vanishing Lyapunov exponent.

The second method is to explicitly compute the integrals of motion as a function of time. If we define the set of variables $a_i,\ b_i$ as

$$a_i = e^{\frac{q_{i+1} - q_i}{2}},\ b_i = p_i, \tag{2.22}$$

then we can construct the Lax pair of matrices $(L,\ M)$ [83] defined as

$$L = \begin{bmatrix} b_1 & a_1 & 0 & a_n \\ a_1 & b_2 & & 0 \\ 0 & & & \\ a_n & 0 & & b_n \end{bmatrix},\ M = \begin{bmatrix} 0 & a_1 & 0 & -a_n \\ -a_1 & 0 & a_2 & \\ 0 & -a_2 & 0 & \\ a_n & & & \end{bmatrix}. \tag{2.23}$$

The equations of motion cast in terms of L and M have the form

$$\frac{dL(t)}{dt} = [M(t), L(t)] \equiv M(t)L(t) - L(t)M(t). \tag{2.24}$$

The eigenvalues of L are constants of motion and can be considered as the integrals of motion $\{I_n\}$ for this problem [84]. We plot in Fig. 2.20-a the 32 eigenvalues of L as a function of time for a 32-particle Toda lattice, with initial positions and momenta randomly selected. The invariance of $I_n(t)$ confirms that the system is integrable and illustrates the accuracy of our numerical simulation, excluding the possibility that the exponential tail in Fig. 2.19-f is an artifact of some numerical error (e.g. rounding error), which adds a stochastic noise to the time series.

[5] We use the term "neighbor" here in a symbolic way, since the positions of all the particles are steadily changing. i and $i+1$ label the same particles during the time evolution.

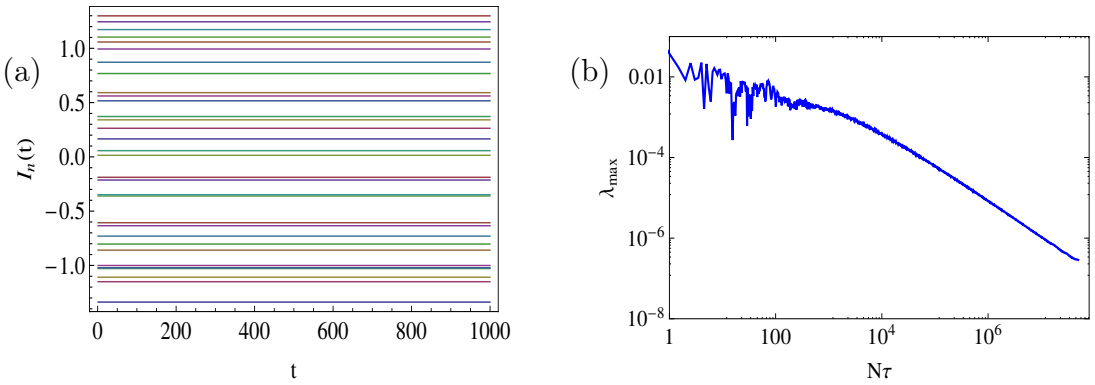

Figure 2.20: (a) The integrals of motion I_n as a function of time for a Toda lattice consisting of 32 particles, with random initial coordinates and momenta. (b) $\lambda_{max}(t_N)$ as defined in 1.3 computed for the same system.

We note, however, that Toda lattice is exceptional in two important aspects. First, a potential in the form of a truncated Taylor series expansion of the exponential function for any order higher than two yields a nonintegrable system [85]. We illustrate this theorem numerically by computing I_n for a truncated potential up to the third order as shown in Fig. 2.21-a, where we notice the wiggling of I_n at long times. We have also computed $\lambda_{max}(t_N)$ for the third- order and fifth-order truncated exponential potential and confirmed that both approach nonzero asymptotic limits as shown in Fig. 2.21-b. Second, although Toda lattice is completely integrable, it is not separable [83]. (A separable problem has constants of motion which are at most quadratic in momenta, and the equations are solved by quadratures).

We finally note that the values of the integrals of motion I_n in Fig. 2.20 are randomly distributed, since the initial conditions are themselves random. We noticed that if we start with a more regular set of initial conditions, the integrals of motion are more uniformly distributed. We show in Fig. 2.22 I_n for the case when the initial coordinates of the particles are given by

$$q_i(0) = A \sin\left(\frac{2\pi i}{N}\right), \quad i = 1, \ldots N \tag{2.25}$$

and $p_i(0) = 0$. We notice in this case that the tail of the power spectrum is not purely exponential.

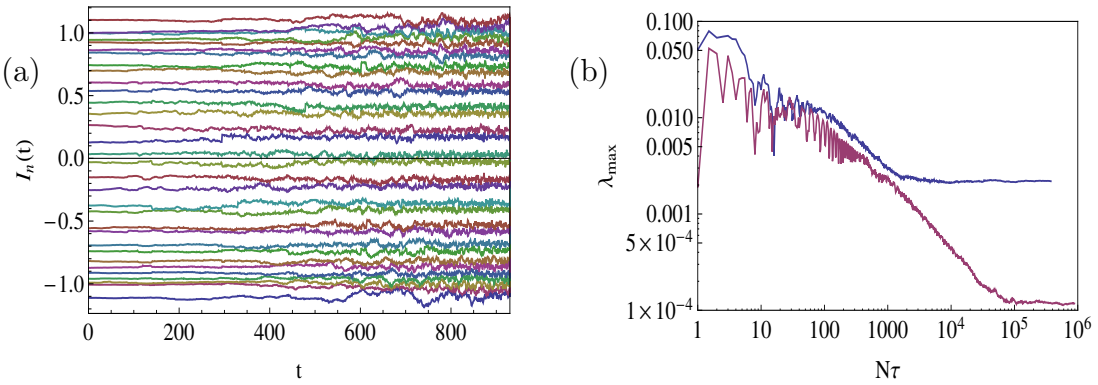

Figure 2.21: (a) Eigenvalues for the matrix $L(t)$ for a Toda lattice with a truncated potential up to third order. (b) $\lambda_{max}(t_N)$ for a Toda lattice with a truncated potential up to third order (blue) and fifth order (purple).

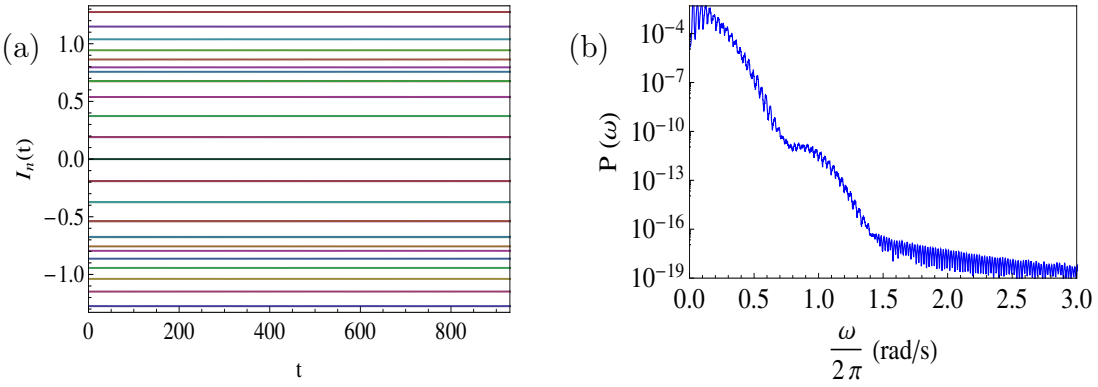

Figure 2.22: (a) Integrals of motion of the Toda lattice consisting of 32 particles. The initial coordinates of particles are chosen according to 2.25. (b) The power spectrum of the time series of the coordinate of a single particle for the same Toda lattice.

2.5 Summary

In this chapter, we illustrated the failure of conventional techniques to discriminate between integrable and chaotic dynamics in many dimensional systems from a finite-length time series. We then presented a new technique that can discriminate chaotic from integrable deterministic dynamics from a finite, but very accurately measured set of data. We applied this technique to time series produced by integrable and nonintegrable classical spin lattices. This techniques relies on the

distinction between integrable and chaotic time series in the frequency domain. While the power spectra of integrable systems are normally sharply terminated, chaotic systems exhibit long exponential tails in their power spectra. This distinction leads to easily identifiable differences between chaotic and integrable time series (c.f. Figs. 2.12 and 2.13). The integrable time series becomes more regular, while the chaotic time series becomes bursty and irregular after taking the time derivatives. This difference makes the rates of entropy production behave differently in both cases as we take the time derivatives. We introduced quantitative measures to capture the differences in time domain and frequency domain between the two types of dynamics. We also showed that the decay constant of the exponential tail of the power spectrum in the chaotic classical spin system is not related to the value of the maximum Lyapunov exponent (c.f. Fig. 2.10). We illustrated the differences between the power spectra of integrable and nonintegrable systems by including several examples of both types of systems. With the exception of Toda lattice, all integrable systems considered exhibit a spectrum that consists of well-separated discrete frequencies or terminates in a non-exponential way. The difference between the power spectra of integrable and nonintegrable systems in the quantum domain requires further investigations.

2.6 Appendix: Examples of numerically computed higher-order time derivatives for integrable and chaotic classical spin systems

In Fig. 2.12, we presented the fragments of two time series representing the total spin polarization $M_x(t)$ for the chaotic and the integrable $6 \times 6 \times 6$ spin clusters together with their respective $7^{\underline{\text{th}}}$ derivatives, $M_x^{(7)}(t)$. In Fig. 2.23 below, we show the plots for all the derivatives $M_x^{(n)}(t)$ of the same time series up to the $9^{\underline{\text{th}}}$ order. We used the standard finite-difference numerical procedure for computing these derivatives. Namely, if the discretized time series in a given order was $\left\{..., \left(t_i, M_{x,i}^{(n)}\right), \left(t_{i+1}, M_{x,i+1}^{(n)}\right), \left(t_{i+2}, M_{x,i+2}^{(n)}\right), ...\right\}$, then the next-order derivative was obtained as $\left\{..., \left(t_i, \frac{M_{x,i+1}^{(n)} - M_{x,i}^{(n)}}{t_{i+1} - t_i}\right), \left(t_{i+1}, \frac{M_{x,i+2}^{(n)} - M_{x,i+1}^{(n)}}{t_{i+2} - t_{i+1}}\right), ...\right\}$.

The numerical derivatives beginning with the $9^{\underline{\text{th}}}$ in the integrable case and $10^{\underline{\text{th}}}$ in the chaotic case show signs of numerical noise associated with the accumulated rounding errors. In order to exclude this concern, the presentation in Fig. 2.12

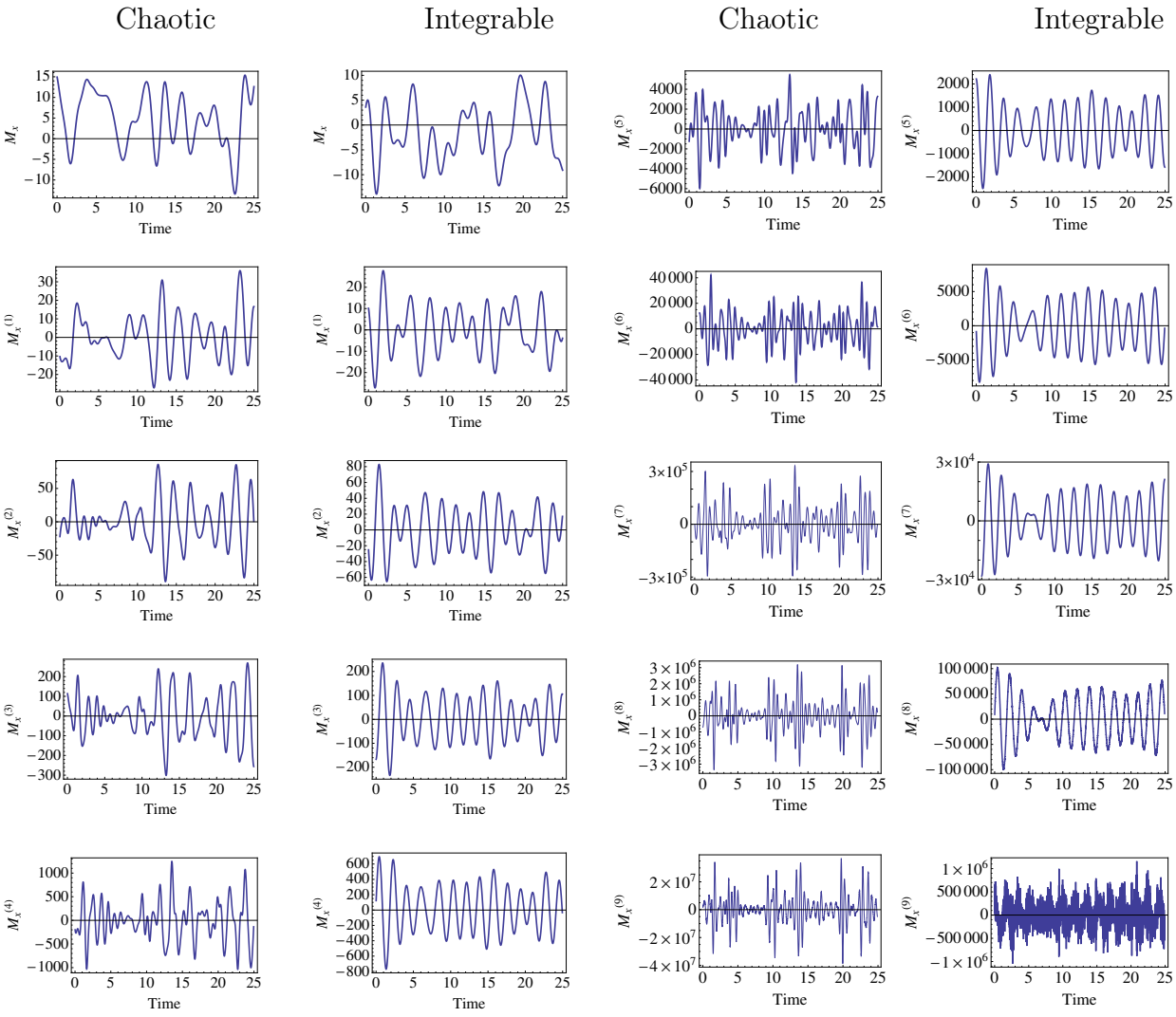

Figure 2.23: Plots of $M_x(t)$ and its nine derivatives for the chaotic and integrable classical spin systems considered in Fig. 2.12. Note: the $9^{\underline{\text{th}}}$ derivative for the integrable case exhibits extrinsic noise due to numerical rounding errors.

was limited to the $7^{\underline{\text{th}}}$ derivative.

Quantum phenomena do not occur in a Hilbert space,
they occur in a laboratory!

Asher Peres

3

Regression relations for pure quantum states and their implications for efficient computing

The purpose of this chapter is two-fold. First, to provide evidence for the validity of the Onsager regression relation (ORR) applied to pure states of isolated many-body quantum systems at high temperature. We, additionally, derive a modified regression relation for pure states of many-body quantum systems that relates the relaxation for an observable quantity for a system in a pure quantum state to the correlation of the expectation value of the same observable at equilibrium. Second, we introduce remarkably simple and fast numerical methods to calculate correlation functions of a many-body quantum system at high temperature [4]. This approach requires only direct simulation of the time evolution of pure quantum states. The validity of these methods is justified by the recently proved quantum dynamical typicality theorem [86]. This theorem states that computing many quantum observables that require averaging over the whole Hilbert space can be achieved with decent accuracy by considering only one properly chosen pure state.

In chapters 4 and 5, we exploit the methods described in this chapter to compute important quantities in the context of quantum chaos and spin diffusion.

3.1 Linear response theorem and Onsager regression relation

In 1931, Onsager had the profound insight that "the average regression of fluctuations will obey the same laws as the corresponding macroscopic irreversible process" [87]. For a classical observable $A(t)$, the Onsager regression relation (ORR) states that

$$\frac{\bar{A}(t) - A_0}{\bar{A}(0) - A_0} = \frac{\langle \delta A(t) * \delta A(0) \rangle_{eq}}{\langle (\delta A(0))^2 \rangle_{eq}}, \tag{3.1}$$

where $\bar{A}(t)$ represents the average relaxation of $A(t)$ from a close-to-equilibrium state, A_0 represents the mean value of $A(t)$ at equilibrium, $\delta A(t)$ represents the equilibrium fluctuations of $A(t)$ and $\langle \cdots \rangle_{eq}$ represents the average over an equilibrium ensemble. The LHS of Eq. 3.1 represents the average evolution of $A(t)$ from a nonequilibrium state to its equilibrium value A_0 in the linear response regime, while the RHS represents the correlation of the fluctuations of $A(t)$ at equilibrium.

To introduce the quantum version of ORR, let us consider a quantum system described by a Hilbert space of dimension N, where $N \gg 1$ and a quantum observable, described by operator $\hat{A}$, that has zero average at equilibrium, i.e.,

$$\mathrm{Tr}\{\hat{A}\} = 0. \tag{3.2}$$

Let ρ_{neq} represent the nonequilibrium initial density matrix given by

$$\rho_{\mathrm{neq}} = \frac{1}{N} \exp(\alpha \hat{A}), \tag{3.3}$$

with α being a small constant. ORR for such a system is

$$\mathrm{Tr}\left\{\hat{A}(t)\rho_{\mathrm{neq}}\right\} = \frac{\alpha}{N} \mathrm{Tr}\left\{\hat{A}(t)\hat{A}(0)\right\}, \tag{3.4}$$

where $\hat{A}(t) = e^{i\mathcal{H}t}\hat{A}e^{-i\mathcal{H}t}$. The RHS of Eq. 3.4 represents the infinite temperature correlation function of $\hat{A}(t)$ at equilibrium.

While it is clear that in the limit of very small α, $\rho_{\mathrm{neq}} \cong \frac{\alpha}{N}\hat{A}$ and Eq. 3.4 will be fulfilled, we provide a formal derivation of this relation in the context of linear response theorem in the rest of this section. In the next section, we investigate the

validity of Eq. 3.4 on the level of single pure state evolution based on the results of quantum dynamical typicality.

A particular example of ORR relevant for the content of this dissertation is the free induction decay (FID) in solids introduced in chapter 5. In this case, the FID signal defined as the relaxation function of the magnetization of a lattice of interacting magnetic dipoles towards an equilibrium state is proportional to the infinite temperature correlation function of the magnetization.

Quantum regression theorem has been used successfully in quantum optics since the work of M. Lax in the sixties in the context of quantum systems weakly coupled to a Markovian reservoir (see [88] for a recent review). In that setting, the regression relation is used to compute two-time correlation functions in terms of single-time correlation functions, since according to Lax theorem both quantities follow the same equations of motion. In the present work, we apply the regression theorem to closed systems, self-equilibrating under their own dynamics.

3.1.1 Onsager relation as the high-temperature limit of the fluctuation-dissipation theorem

The general framework which connects the macroscopic behavior of a thermodynamic system and its microscopic properties is provided by the fluctuation-dissipation theorem (FDT) [89]. FDT is considered today to be one of the most important results in nonequilibrium statistical mechanics. ORR is the high-temperature limit of FDT. The remarkable success of FDT lies in its ability to express transport coefficients in terms of correlation functions at equilibrium [90]. In what follows, we present a derivation of the quantum version of the Onsager regression relation at infinite temperature, i.e., Eq. (3.4), based on the fluctuation-dissipation Theorem.

Let us consider an observable quantity $\hat{A}$ in a system driven by a force $\hat{\mathcal{F}}$ that couples to another observable $\hat{B}$, such that it adds a term $-f(t)\hat{B}$ to the Hamiltonian of the system, where $f(t)$ is a weak time-dependent field. According to the Kubo formula [91], the average causal response of $\hat{A}$ to the force $\hat{\mathcal{F}}$ in the linear response regime (near-equilibrium regime) is given by

$$\langle \hat{A}(t) \rangle_{neq} = \langle \hat{A} \rangle_{eq} + \int_{-\infty}^{t} \chi_{AB}(t-t') f(t') dt', \tag{3.5}$$

where $\langle \hat{A} \rangle_{eq}$ is the average of $\langle \hat{A} \rangle$ at equilibrium (i.e., before the perturbation term is applied) while $\langle \hat{A}(t) \rangle_{neq}$ is the evolution of $\langle \hat{A} \rangle$ in response to the applied field.

$\chi(t-t')$ is the quantum response function, or simply the susceptibility, and is expressed as

$$\chi_{AB}(t-t') = \frac{i}{\hbar}\langle[\hat{A}(t), \hat{B}(t')]\rangle_{eq}\Theta(t-t'). \tag{3.6}$$

The theta function in 3.6 represents the causality property of the response. The expectation values are calculated at equilibrium, i.e., without applying the force $\hat{\mathcal{F}}$.

Now, let us define the equilibrium correlation function $S_{AB}(t-t')$ as $\langle\hat{A}(t)\hat{B}(t')\rangle_{eq}$ and the symmetrized correlation function $\phi_{AB}(t) = \frac{1}{2}(S_{AB}(t) + S_{BA}(-t))$. For the purpose of the present work, we take $\hat{B} = \hat{A}$ and assume that the driving field is applied at a constant strength in the distant past and switched off at $t = 0$. We are interested in the response of $\hat{A}$ at $t > 0$. The subscripts 'AA' and 'eq' are dropped in the rest of this discussion. Since we are dealing with a traceless operator, the equilibrium value of $\hat{A}$ at infinite temperature is zero. Therefore, Eq. 3.5 reads

$$\langle\hat{A}(t)\rangle_{neq} = \int_{-\infty}^{0} \chi(t-t')dt'. \tag{3.7}$$

We define the anti-symmetric version of the $\chi(\tau)$ as

$$\chi_a(\tau) = \frac{1}{2}[\chi(\tau) - \chi(-\tau)]. \tag{3.8}$$

The relaxation function $R(t) \equiv \langle\hat{A}(t)\rangle_{neq}$ defined for $t > 0$ can be extended to the whole time axis in the symmetrized form $R_s(t) \equiv R(t) + R(-t) - R(0)$ as shown in Fig. 3.1. Since the relaxation function $R(t)$ can be written as $R(t) = \int_t^\infty \chi(\tau)d\tau$, we can express $R_s(t)$ in terms of $\chi_a(t)$ as

$$R_s(t) = 2\int_t^\infty \chi_a(\tau)d\tau, \tag{3.9}$$

where we used the fact that $\chi(t) = 0$ for $t < 0$ as depicted in Fig. 3.1.

Let us now switch to the frequency domain by taking the Fourier transform of all the quantities defined so far. According to FDT [92], the spectral density of equilibrium fluctuations of an observable A at temperature T, $\phi(\omega) \equiv \langle A^2(\omega)\rangle \equiv \int_{-\infty}^{\infty}\left\langle\hat{A}(0)\hat{A}(t)\right\rangle_{\mathrm{S}} e^{i\omega t}dt$, is related to the imaginary part of the susceptibility $\chi''(\omega)$ by the relation

$$\phi(\omega) = \hbar\ \coth(\hbar\omega/2k_BT)\chi''(\omega). \tag{3.10}$$

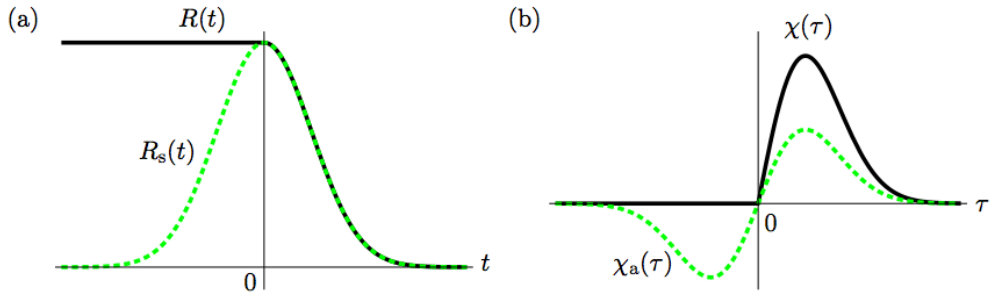

Figure 3.1: (a) Sketches of the relaxation function R(t) and the symmetrized relaxation function $R_s(t)$. (b) Sketches of the susceptibility function $\chi(\tau)$ and its antisymmetric part $\chi_a(\tau)$. The figure is from [4].

The high temperature limit of this relation is

$$\phi(\omega) = \frac{2k_BT}{\omega}\chi''(\omega). \tag{3.11}$$

Using the symmetry properties of Fourier Transforms of real functions, we can easily see that

$$\chi''(\omega) = -i\chi_a(\omega). \tag{3.12}$$

Therefore, we can rewrite Eq. 3.11 as

$$\phi(\omega) = -i\frac{2k_BT}{\omega}\chi_a(\omega). \tag{3.13}$$

Taking the inverse Fourier Transform of Eq. 3.13, using the fact that the Fourier Transform of $\int_{-\infty}^{t}\chi_a(\tau)d\tau$ is $\frac{1}{i\omega}\chi_a(\omega) + \pi\chi_a(\omega)\delta(\omega)$ and keeping in mind that $\chi_a(\omega)|_{\omega=0} = 0$, we arrive at

$$\phi(t) = 2k_BT\int_{-\infty}^{t}\chi_a(\tau)d\tau. \tag{3.14}$$

Since $\chi_a(\tau)$ is anti-symmetric, i.e., $\int_{-\infty}^{\infty}\chi_a(\tau)d\tau = 0$, we rewrite $\phi(t)$ as

$$\phi(t) = -2k_BT\int_{t}^{\infty}\chi_a(\tau)d\tau. \tag{3.15}$$

From Eq. 3.9 and 3.15, we conclude that $\phi(t)$ and $R_s(t)$ are proportional to each other and subsequently $\langle\hat{A}(t)\rangle_{neq} \propto \langle\hat{A}(t)\hat{A}\rangle_{eq}$. At infinite temperature, $\langle\hat{A}(t)\hat{A}\rangle_{eq} = \mathrm{Tr}\{\hat{A}(t)\hat{A}\}$. Thus, we finally obtain the quantum regression relation at infinite temperature

$$\langle\hat{A}(t)\rangle_{neq} \propto \mathrm{Tr}\{\hat{A}(t)\hat{A}\}. \tag{3.16}$$

3.1.2 Onsager regression relation at finite temperature

While ORR declares that the relaxation function of some observable is proportional to the correlation of its fluctuations at equilibrium, FDT implies that quantum systems respect this relation in the classical limit only, i.e., at sufficiently high temperatures, due to the non-trivial dependence on frequency in the prefactor in Eq. 3.10. This fact led to some confusion regarding the applicability of the regression theorem in quantum systems, which has been settled [93] by showing that FDT is the proper generalization of the Onsager regression relation at any temperature. In this part, we explore the conditions under which the regression relation holds in this case at finite temperatures.

We start by writing the equilibrium density matrix at temperature T, assuming $k_B = 1$,

$$\rho_{eq} = \frac{1}{Z} \; e^{-\mathcal{H}/T}, \tag{3.17}$$

where $Z = \mathrm{Tr}\left\{e^{-\mathcal{H}/T}\right\}$. The condition of zero equilibrium value of $\hat{A}$ becomes $\mathrm{Tr}\{\hat{A}\; e^{-\mathcal{H}/T}\} = 0$. The equilibrium fluctuation of $\hat{A}$ can be characterized by different correlation functions. The first one is

$$\left\langle \hat{A}(0)\hat{A}(t) \right\rangle \equiv \frac{1}{Z}\; \mathrm{Tr}\left\{ \hat{A}\; e^{i\mathcal{H}t/\hbar}\; \hat{A} e^{-i\mathcal{H}t/\hbar}\; e^{-\mathcal{H}/T} \right\}. \tag{3.18}$$

The symmetrized version of 3.18 is

$$\left\langle \hat{A}(0)\hat{A}(t) \right\rangle_{\mathrm{S}} \equiv \frac{1}{2}\left(\left\langle \hat{A}(0)\hat{A}(t) \right\rangle + \left\langle \hat{A}(0)\hat{A}(-t) \right\rangle \right), \tag{3.19}$$

while the anti-symmetrized version is

$$\left\langle \hat{A}(0)\hat{A}(t) \right\rangle_{\mathrm{A}} \equiv \frac{1}{2}\left(\left\langle \hat{A}(0)\hat{A}(t) \right\rangle - \left\langle \hat{A}(0)\hat{A}(-t) \right\rangle \right). \tag{3.20}$$

Unlike the infinite temperature case, the first two versions are distinct and carry different information. To arrive at a regression relation that relates the relaxation function with any of these correlation functions, we start with the symmetrized relaxation function

$$R_{\mathrm{s}}(t) \equiv R(t) + R(-t) - R(0) = \mathrm{Tr}\left\{ e^{i\mathcal{H}|t|/\hbar}\; \hat{A}\; e^{-i\mathcal{H}|t|/\hbar} \rho_0 \right\}, \tag{3.21}$$

where $\rho_0 = \frac{1}{Z_0}\; e^{-(\mathcal{H} - f_0\hat{A})/T}$. We can expand $e^{-(\mathcal{H}-f_0\hat{A})}$ as a power series of f_0 [94]

$$e^{-(\mathcal{H}-f_0\hat{A})/T} \approx e^{-\mathcal{H}/T}\left(\mathbb{1} + f_0 \int_0^{1/T} e^{\alpha\mathcal{H}} \hat{A} e^{-\alpha\mathcal{H}} d\alpha + \ldots \right). \tag{3.22}$$

The zeroth order contribution in Eq. 3.22 vanishes due to the traceless nature of A and the first order contribution can be expanded as a power series of $\frac{1}{T}$

$$\int_0^{1/T} e^{\alpha\mathcal{H}}\hat{A}e^{-\alpha\mathcal{H}}d\alpha = \frac{1}{T}\,\hat{A} + \frac{1}{2T^2}\,[\mathcal{H},\hat{A}] + \frac{1}{3!\;T^3}\,[\mathcal{H},[\mathcal{H},\hat{A}]] + \dots\,. \tag{3.23}$$

Now, it is clear that when $[\mathcal{H},\hat{A}]$ is sufficiently small, we can truncate the expansion in Eq. 3.23 to the first order in $\frac{1}{T}$. Then after substituting in Eqs. 3.22 and 3.21, we recover the symmterized correlation function $\left\langle \hat{A}(0)\hat{A}(t)\right\rangle_{\mathrm{S}}$. The condition of small $[\mathcal{H},\hat{A}]$ is satisfied for example due to some conservation law that makes $\hat{A}$ a slow variable, or when $T/\hbar$ is much larger than the typical one-particle frequency [95].

3.2 Quantum dynamical typicality

The formal structure of ORR as expressed by Eq. 3.4, implies that Onsager relation is applicable on average to an ensemble of pure many-body quantum states, or a mixed quantum state, described initially by the density matrix ρ_{neq}. One might ask, however, how far does ORR apply at the level of a single pure state. We give the answer to this question based on the notion of 'typicality' [96–98]. Typicality, in general, aims to relate quantum phenomena, normally described by density matrix language, with individual realizations described by pure quantum states. For example, the term canonical typicality describes the observation that a single *typical* pure state describing a system coupled to a bath at a certain temperature will yield the correct canonical density matrix for the system after tracing out the degrees of freedom of the bath.

Quantum dynamical typicality states that the time-dependent expectation value for an observable quantity computed for a single pure state randomly selected from an ensemble of nonequilibrium initial states will be very close to the ensemble-averaged expectation value with an overwhelming probability [96]. To introduce the concept of dynamical typicality, consider a Hilbert space H of dimension N and spanned by the orthonormal basis $\{|n\rangle\}$. For any distribution ρ over all pure, normalized states $\{|\psi\rangle\}$ which is invariant under unitary transformations, the average of an observable $\hat{D}$ with respect to this distribution is called Hilbert Space Average $HA[\langle\psi|\hat{D}|\psi\rangle]$ and is given by [97]

$$HA[\langle\psi|\hat{D}|\psi\rangle] = \frac{\mathrm{Tr}\{D\}}{N}, \tag{3.24}$$

while the Hilbert space variance $HV[\langle\psi|\hat{D}|\psi\rangle] \equiv HA\left[\left(\langle\psi|\hat{D}|\psi\rangle - HA[\langle\psi|\hat{D}|\psi\rangle]\right)^2\right]$ is given by

$$HV[\langle\psi|\hat{D}|\psi\rangle] = \frac{1}{N+1}\left(\frac{\mathrm{Tr}\{\hat{D}^2\}}{N} - \left(\frac{\mathrm{Tr}\{\hat{D}\}}{N}\right)^2\right). \tag{3.25}$$

From (3.24) and (3.25), we can write

$$\langle\psi|\hat{D}|\psi\rangle_\rho = \mathrm{Tr}\{D\rho\}\left[1 + O\left(\frac{1}{\sqrt{N}}\right)\right], \tag{3.26}$$

where $\langle\psi|\hat{D}|\psi\rangle_\rho$ represents the average of $\hat{D}$ computed with one *typical* pure state that "samples" ρ. The generalization of (3.26) to the nonequilibrium ensemble $\rho_{\mathrm{neq}} = \frac{1}{N}\exp(\alpha\hat{A})$ is:

$$\langle\Psi_{\mathrm{neq}}|\hat{A}|\Psi_{\mathrm{neq}}\rangle = \mathrm{Tr}\left\{\hat{A}\rho_{\mathrm{neq}}\right\}\left[1 + O\left(\frac{1}{\alpha\sqrt{N}}\right)\right], \tag{3.27}$$

where $|\Psi_{\mathrm{neq}}\rangle$ is a wave function that samples ρ_{neq}. Now comes the dynamical part in "dynamical typicality" and the validity of (3.27) is extended to the time evolution generated by the Hamiltonian $\mathcal{H}$

$$\langle\Psi_{\mathrm{neq}}|\hat{A}(t)|\Psi_{\mathrm{neq}}\rangle = \mathrm{Tr}\left\{\hat{A}(t)\rho_{\mathrm{neq}}\right\}\left[1 + O\left(\frac{1}{\alpha\sqrt{N}}\right)\right], \tag{3.28}$$

where $\hat{A}(t) = e^{i\mathcal{H}t}\hat{A}e^{-i\mathcal{H}t}$. The message of this equation, as expressed in [97], is "individual dynamics of expectation values are typically well described by the ensemble average ". From 3.28 and 3.4, we conclude that

$$\langle\Psi_{\mathrm{neq}}|\hat{A}(t)|\Psi_{\mathrm{neq}}\rangle = \frac{\alpha}{N}\mathrm{Tr}\left\{\hat{A}(t)\hat{A}(0)\right\}\left[1 + O\left(\frac{1}{\alpha\sqrt{N}}\right)\right], \tag{3.29}$$

which is ORR on the level of a single pure state.

3.3 Modified regression relation

Equation 3.29 implies that Onsager regression relation can be used as a rigorous method to compute infinite temperature correlation functions from the time evolution of a single nonequilibrium pure state. Now, we go one step further and ask the following conceptual question: Can we compute the infinite temperature correlation function $\mathrm{Tr}\left\{\hat{A}(t)\hat{A}(0)\right\}$ by monitoring the equilibrium noise of $\langle\hat{A}(t)\rangle$ for sufficiently long time? Can we extract the information contained in $\mathrm{Tr}\left\{\hat{A}(t)\hat{A}(0)\right\}$

from one single time series of $\langle \hat{A}(t) \rangle$ generated by a macroscopic quantum system at equilibrium, i.e., in the limit $N \to \infty$ and $T_0 \to \infty$, where T_0 is the time during which $\hat{A}$ is monitored? The answer to this question is provided through the observation that the correlation function $C(t, T_0)$ for the time series of the expectation value $\langle \Psi_{\rm eq} | \hat{A}(t') | \Psi_{\rm eq} \rangle$ in the time interval $[-T_0, T_0 + t]$ defined as,

$$C(t, T_0) \equiv \frac{1}{2T_0} \int_{-T_0}^{T_0} dt' \langle \Psi_{\rm eq} | \hat{A}(t + t') | \Psi_{\rm eq} \rangle \langle \Psi_{\rm eq} | \hat{A}(t') | \Psi_{\rm eq} \rangle, \tag{3.30}$$

provides a good approximation for the infinite temperature correlation function $\mathrm{Tr}\left\{ \hat{A}(t)\hat{A}(0) \right\}$ in the limit of large T_0 and N. In particular, we will show below that

$$C(t, T_0) = \frac{1}{N^2} \mathrm{Tr}\left\{ \hat{A}(t)\hat{A}(0) \right\} + \Delta_1, \tag{3.31}$$

where

$$\overline{\Delta_1^2} \approx \frac{1}{2\sqrt{2}\, T_0 N^4} \int_{-T_0\sqrt{2}}^{T_0\sqrt{2}} dt_2 \Bigg(\left[\mathrm{Tr}\left\{ \hat{A}(t_2)\hat{A}(0) \right\} \right]^2 + \mathrm{Tr}\left\{ \hat{A}(t - t_2)\hat{A}(0) \right\} \mathrm{Tr}\left\{ \hat{A}(t + t_2)\hat{A}(0) \right\} \Bigg). \tag{3.32}$$

The two terms in the integral (3.32) are of equal orders of magnitude. The order of magnitude of the correction term Δ_1 depends on how fast $\mathrm{Tr}\left\{ \hat{A}(t_2)\hat{A}(0) \right\}$ decays to zero. If the timescale for the decay of $\left[\mathrm{Tr}\left\{ \hat{A}(t_2)\hat{A}(0) \right\} \right]^2$ is τ, then $\Delta_1 = O(\sqrt{\tau/T_0}) \mathrm{Tr}\left\{ \hat{A}^2 \right\} / N^2$.

Based on the results of (3.31) and (3.29), we introduce the modified regression relation

$$\lim_{N\to\infty} \langle \Psi_{\rm neq} | \hat{A}(t) | \Psi_{\rm neq} \rangle = \alpha \lim_{T_0\to\infty, N\to\infty} N C(t, T_0). \tag{3.33}$$

The message of this relation is that the correlation of the time series of the expectation value of an observable $\hat{A}$ for a system in a pure state selected from the equilibrium ensemble is proportional to the relaxation of $\langle \Psi_{\rm neq} | \hat{A}(t) | \Psi_{\rm neq} \rangle$ from a slightly perturbed state towards equilibrium, in the limit of large N and T_0. The difference between $C(t, T_0)$ and the trace formula $\mathrm{Tr}\left\{ \hat{A}(t)\hat{A}(0) \right\}$ is the difference between a classical correlation function that involves the correlation of a time series and a quantum correlation function that involves the correlation of quantum operators. Eq. 3.31 implies that that both correlation functions contain the same information in the macroscopic limit.

To derive Eqs. 3.31 and 3.32, we write $C(t,T_0)$ in terms of the matrix elements $\{A_{mn}\}$ of $\hat{A}$ and the expansion coefficients $\{a_k\}$ of $|\Psi_{\rm eq}\rangle$, represented in terms of the energy basis $\{|\phi_k\rangle\}$, as follows

$$C(t,T_0)=\frac{1}{2T_0}\int_{-T_0}^{T_0}dt'\sum_{m,n,p,q}a_q^*a_n^*a_pa_mA_{qp}A_{nm}e^{i(\epsilon_q-\epsilon_p)t/\hbar}e^{i(\epsilon_q-\epsilon_p+\epsilon_n-\epsilon_m)t'/\hbar}, \quad (3.34)$$

where $\{\epsilon_k\}$ are the eigen-energies. We let $\hbar=1$ in the rest of this chapter. The Hilbert space average of $C(t,T_0)$ expressed as $\overline{C(t,T_0)}$ is obtained by averaging over all the expansion coefficients $\{a_k\}$. Due to the randomness of the complex phases of a_k, the Hilbert-space average $\overline{a_q^*a_n^*a_pa_m}$ will be nonzero only when two of the four coefficients are the complex conjugates of the other two coefficients. In this case, $\overline{a_q^*a_n^*a_pa_m}$ reduces to $(\overline{|a_q|^2})^2=1/N^2$. The number of the terms where the four coefficients coincide is smaller by a factor $1/N$. Therefore, we neglect these terms and we are left with

$$\overline{a_q^*a_n^*a_pa_m}=1/N^2(\delta_{qp}\delta_{nm}+\delta_{qm}\delta_{np}). \quad (3.35)$$

After substituting in the the Hilbert space average of 3.34, we obtain

$$\overline{C(t,T_0)}=\frac{1}{N^2}\sum_{m,n}e^{i(\epsilon_m-\epsilon_n)t}A_{mn}A_{nm}=\frac{1}{N^2}\mathrm{Tr}\left\{\hat{A}(t)\hat{A}(0)\right\}, \quad (3.36)$$

which is the principal part of 3.31.

Now, we compute the variance $\overline{\Delta_1^2}\equiv\overline{\left[C(t,T_0)-\overline{C(t,T_0)}\right]^2}$, which defines the deviation of $C(t,T_0)$ computed by a single realization from the Hilbert space average. The explicit form of $\overline{\Delta_1^2}$ can be obtained using Eq. 3.36 as

$$\begin{aligned}\overline{\Delta_1^2}=&\tfrac{1}{4T_0^2}\textstyle\int_{-T_0}^{T_0}dt'\int_{-T_0}^{T_0}dt''A_{qp}A_{nm}A_{kl}A_{uv}\;e^{i(\epsilon_q-\epsilon_p+\epsilon_k-\epsilon_l)t}\;e^{i(\epsilon_q-\epsilon_p+\epsilon_n-\epsilon_m)t'}\;e^{i(\epsilon_k-\epsilon_l+\epsilon_u-\epsilon_v)t''}\\&\times\textstyle\sum_{q,p,m,n,k,l,u,v}\left[\overline{a_q^*a_n^*a_k^*a_u^*a_pa_ma_la_v}-\tfrac{1}{N^4}(\delta_{qp}\delta_{nm}+\delta_{qm}\delta_{np})(\delta_{kl}\delta_{uv}+\delta_{kv}\delta_{ul})\right]. \quad (3.37)\end{aligned}$$

By following similar arguments to the case of $\overline{a_q^*a_n^*a_pa_m}$, we can see that $\overline{a_q^*a_n^*a_k^*a_u^*a_pa_ma_la_v}$ will be nonzero only when the coefficients are arranged into conjugate pairs. In this case, we will have $\overline{a_q^*a_qa_n^*a_na_k^*a_ka_u^*a_u}=(\overline{|a_q|^2})^4=1/N^4$. The terms containing two or more identical pairs will be exponentially smaller than when all the four pairs are distinct. Therefore, we have

$$\begin{aligned}\overline{a_q^* a_n^* a_k^* a_u^* a_p a_m a_l a_v} \;=\; \tfrac{1}{N^4}[\;& \delta_{qm}\delta_{np}\delta_{kv}\delta_{ul} \;+\; \delta_{ql}\delta_{nv}\delta_{kp}\delta_{um} \;+\; \delta_{qv}\delta_{nl}\delta_{km}\delta_{up} \\ &+ \delta_{qm}\delta_{nl}\delta_{kv}\delta_{up} \;+\; \delta_{qv}\delta_{np}\delta_{km}\delta_{ul} \;+\; \delta_{qm}\delta_{nv}\delta_{kp}\delta_{ul} \\ &+ \delta_{ql}\delta_{np}\delta_{kv}\delta_{um} \;+\; \delta_{ql}\delta_{nv}\delta_{km}\delta_{up} \;+\; \delta_{qv}\delta_{nl}\delta_{kp}\delta_{um} \\ &+ \{\text{omitted terms}\}\;].\end{aligned} \tag{3.38}$$

The first term in 3.39 cancels with part of the second term in 3.37. After substituting the second and third terms of 3.39 into 3.37, the result will contain an integral of the form

$$\frac{1}{4T_0^2}\int_{-T_0}^{T_0}\int_{-T_0}^{T_0} dt'dt''\; e^{i\eta t'}\; e^{-i\eta t''}, \tag{3.39}$$

where η is a combination of the energies ϵ_n. For the sake of approximation, we change the integration variables to $t_1^{'} = (t' + t'')/\sqrt{2}$ and $t_1^{''} = (t'' - t')/\sqrt{2}$, and simultaneously rotate the integration region as shown in Fig. 3.2. This manipulation has the effect of reducing the double integral in 3.39 to the single integral over t_2, defined as $t_2 = t_1^{''}\sqrt{2}$,

$$\frac{1}{2T_0\sqrt{2}}\int_{-T_0\sqrt{2}}^{T_0\sqrt{2}} dt_2\; e^{-i\eta t_2}. \tag{3.40}$$

The values of the two integrals are not exactly the same, but we are only interested in the order of magnitude of Δ_1. The second term in 3.39 yields the integral

$$\frac{1}{2T_0\sqrt{2}}\int_{-T_0\sqrt{2}}^{T_0\sqrt{2}} dt_2\; e^{-i(\epsilon_q-\epsilon_p+\epsilon_n-\epsilon_m)t_2} A_{qp}A_{nm}A_{pq}A_{mn}, \tag{3.41}$$

which can be expressed as $\frac{1}{2\sqrt{2}\;T_0}\int_{-T_0\sqrt{2}}^{T_0\sqrt{2}} dt_2 \left[\mathrm{Tr}\left\{\hat{A}(t_2)\hat{A}(0)\right\}\right]^2$, while the third term in 3.39 yields the integral

$$\frac{1}{2T_0\sqrt{2}}\int_{-T_0\sqrt{2}}^{T_0\sqrt{2}} dt_2\; e^{i(\epsilon_q-\epsilon_p+\epsilon_m-\epsilon_n)t} e^{-i(\epsilon_q-\epsilon_p+\epsilon_n-\epsilon_m)t_2} A_{qp}A_{nm}A_{pq}A_{mn}, \tag{3.42}$$

which can be expressed as $\frac{1}{2\sqrt{2}\;T_0}\int_{-T_0\sqrt{2}}^{T_0\sqrt{2}} dt_2 \mathrm{Tr}\left\{\hat{A}(t-t_2)\hat{A}(0)\right\}\mathrm{Tr}\left\{\hat{A}(t+t_2)\hat{A}(0)\right\}$.

To estimate the order of magnitude of the remaining terms, let us examine the fourth term in 3.39. After substituting that term in 3.37, it will contain the summation:

$$\sum_{q,p,k,l}\left[e^{i(\epsilon_q-\epsilon_p+\epsilon_k-\epsilon_l)t} e^{-i(\epsilon_p-\epsilon_l)t_2} A_{qp}A_{lq}A_{kl}A_{pk}\right]. \tag{3.43}$$

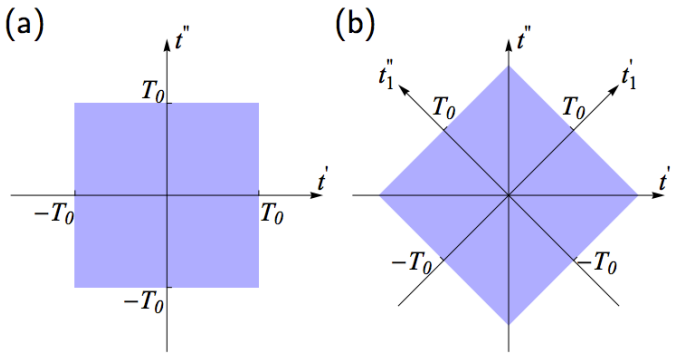

Figure 3.2: (a) The original integration region of the integral in 3.39. (b) The rotated integration region in 3.40 and the new axes $t_1^{'}$ and $t_1^{''}$. The figure is taken from [4].

The terms in this summation can be rearranged as:

$$\sum_{q,p,k,l} \left[e^{i(\epsilon_q-\epsilon_p)t_2} A_{qp} e^{i(\epsilon_k-\epsilon_p)(-t)} A_{pk} A_{kl} e^{i(\epsilon_l-\epsilon_q)(t_2-t)} A_{lq} \right], \tag{3.44}$$

which is equivalent to $\mathrm{Tr}\left\{\hat{A}(t_2)\hat{A}(0)\hat{A}(-t)\hat{A}(t_2-t)\right\}$. For very large $t_2 \sim T_0 \gg t$, the operators separated by t_2 are uncorrelated and the trace has the order of magnitude of $\frac{1}{N}\left[\mathrm{Tr}\left\{\hat{A}(t)\hat{A}(0)\right\}\right]^2$. This term is smaller than the previous two terms (3.41 and 3.42) by factor $1/N$ and can be neglected. The same arguments apply for the remaining terms in 3.39 and 3.37. We can, therefore, write the approximate value of $\overline{\Delta_1^2}$ as

$$\overline{\Delta_1^2} \approx \frac{1}{2\sqrt{2}\ T_0 N^4} \int_{-T_0\sqrt{2}}^{T_0\sqrt{2}} dt_2 \Bigg(\left[\mathrm{Tr}\left\{\hat{A}(t_2)\hat{A}(0)\right\}\right]^2 + \mathrm{Tr}\left\{\hat{A}(t-t_2)\hat{A}(0)\right\} \mathrm{Tr}\left\{\hat{A}(t+t_2)\hat{A}(0)\right\} \Bigg). \tag{3.45}$$

The integrals considered in this derivation converge to small values as long as the limits of the integrals are not too large to encounter the recurrences that occur due to the discreteness of the energy levels. In other words, T_0 should be smaller than the average inverse level spacing of the spectrum. To avoid this problem, we take $\lim_{N\to\infty}$ first and then take $\lim_{T_0\to\infty}$ in Eq. 3.33.

3.4 Efficient computation of correlation functions based on Onsager regression relation and quantum dynamical typicality

Understanding strongly correlated many-body quantum systems has been the driving force behind many of the exciting discoveries in condensed matter in the last few decades. Along with the unexpected and fascinating phenomena which emerge from the interaction between the components of a many-body quantum system, the level of complexity and resources required to analyse such a system increases tremendously with its size. In this regard, any improvement or addition to the arsenal of numerical techniques devised to overcome this problem would be a valuable resource for condensed matter community.

The last two decades have already witnessed the discovery of many useful numerical techniques that proved to be invaluable tools to probe into the properties of strongly interacting systems with limited computer resources. The most pronounced of those algorithms is the Density Matrix Renormalization Group (DMRG) technique [99] that has been used successfully to gain useful information about the static properties of 1D quantum systems. Further algorithms have been developed to deal with time-dependent properties (i.e., time-dependent DMRG - tDMRG [100, 101] and time-evolving block decimation TEBD[102]) and systems in more than one dimension (e.g., projected entangled pair state PEPS[103]).

These methods are more efficient at low temperature [102], while at infinite temperature, they can be practical only for short time evolutions. In general, the cost of numerical simulation using methods dependent on Matrix Product States (like DMRG) increases with the amount of entanglement. Moreover, some improvements have to be incorporated into these methods in order to deal with systems with long-range interactions [104].

In this section, we introduce new methods based on quantum dynamical typicality in conjunction with ORR to efficiently compute correlation functions of strongly interacting many-body quantum systems at infinite temperature. At the same time, we illustrate numerically the applicability of Onsager regression relation at high temperatures on pure state evolution, and test the validity of the modified Onsager regression relation. In order to integrate the time-dependent Schrödinger equation, we use either exact diagonalization or a fourth-order Runge-Kutta algorithm. We first, introduce the Runge-Kutta algorithm, and then pro-

ceed with showing numerically the validity of ORR on pure quantum states (Eq. 3.29). Afterwards, we introduce an even more efficient method to compute the infinite temperature correlation function based on the spirit of quantum dynamical typicality.

3.4.1 Numerical integration of Schrödinger equation

The evolution of pure quantum states is governed by the time-dependent Schrödinger equation, $\frac{d|\psi\rangle}{dt} = -i\hat{H}|\psi\rangle$. Numerical evolution of the initial state can be implemented through a power series expansion of the time evolution operator $\exp(-i\hat{H}dt)$ during a single time step dt. While expansions based on Chebychev polynomials [105] are often used for evolving the Schrödinger equation, we found that a simple fourth-order Runge Kutta algorithm (RK4), which, for time-independent Hamiltonians, is equivalent to the fourth-order Taylor expansion

$$\exp(-i\hat{H}dt) \sim 1 - i\hat{H}dt - \frac{\hat{H}^2dt^2}{2!} + i\frac{\hat{H}^3dt^3}{3!} + \frac{\hat{H}^4dt^4}{4!}, \tag{3.46}$$

is stable and accurate for the purpose for dealing with quantum spin systems. This is one of the new results in this work. Higher powers of $\hat{H}$ applied on the state vector $|\phi\rangle$, $|\phi^n\rangle = \hat{H}^n|\phi\rangle$, are obtained progressively through $|\phi^i\rangle = H|\phi^{i-1}\rangle$. Clearly, this procedure requires only direct matrix-vector multiplications to evolve the wave function. Other methods which are frequently used include the Suzuki Trotter formalism [106] and the short iterative Lancoz algorithm [107].

We verify the accuracy of the Runge-Kutta method in two ways. For a small spin cluster, we evolve the same initial state using exact diagonalization and Runge-Kutta method. At each time step, we verify that the overlap between the two states is equal to unity. For large systems, we evolve the same initial state with two different time steps and verify that the state evolved with the smaller time step, $|\psi_1(t)\rangle$, is almost identical to the other one, $|\psi_2(t)\rangle$, by confirming that they completely overlap at each respective instant, $\langle\psi_1(t)|\psi_2(t)\rangle = 1$. This routine is optimal when the system is too big to be diagonalized in a reasonable time, but not extremely big so that its full Hamiltonian can be stored as a large sparse matrix. Our approach can be combined with other numerical techniques, i.e., Krylov space methods [108], to deal with larger systems where memory is not sufficient for storing the Hamiltonian.

We show in Fig. 3.3 the results of both tests for a Heisenberg spin 1/2 chain consisting of 20 and 29 spins, with nearest neighbor interaction Hamiltonian $\mathcal{H} =$

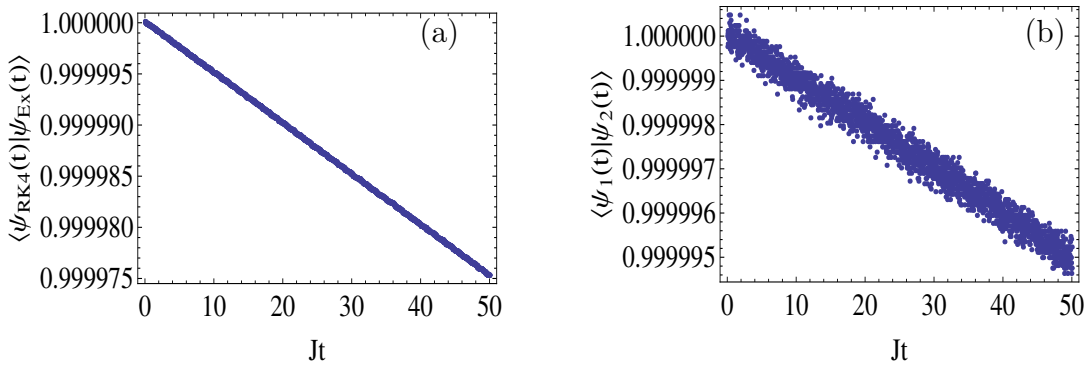

Figure 3.3: Tests of numerical accuracy of the direct integration of the Schrödinger equation using the fourth-order Runge Kutta method. (a) The overlap between two initially identical wave functions for a Heisenberg spin 1/2 chain consisting of 20 spins, $|\Psi_{\mathrm{Ex}}(t)\rangle$ and $|\Psi_{\mathrm{RK4}}(t)\rangle$, computed using the complete diagonalization and the Runge Kutta method respectively. (b) Overlap between two initially identical wave functions for the Heisenberg chain of 29 spins 1/2, $|\Psi_1(t)\rangle$ and $|\Psi_2(t)\rangle$, both computed using the Runge Kutta method with discretization time steps $\Delta t_1 = 0.01/J$ and $\Delta t_2 = 0.02/J$ respectively [4].

$J\sum_i \mathbf{S_i}\cdot\mathbf{S_{i+1}}$. For the 20-spin system, we evolve two identical initial states by the RK4 routine and by exact diagonalization of the Hamiltonian, and compute $|\Psi_{\mathrm{Ex}}(t)\rangle$ and $|\Psi_{\mathrm{RK4}}(t)\rangle$ at each time step. For the 29-spin system, we evolve two identical initial states by the RK4 routine with different time steps, $\Delta t_1 = 0.01/J$ and $\Delta t_2 = 0.02/J$, and compute $|\Psi_1(t)\rangle$ and $|\Psi_2(t)\rangle$. The closeness of both overlap functions to unity confirms the accuracy of the RK4 routine. In all the quantum simulations that use this method in the rest of this thesis, we use a time step in the order of $0.01J^{-1}$, where J is the typical coupling constant of the Hamiltonian.

3.4.2 Numerical verification of Onsager regression relation applied on pure quantum states

In this section, we show numerically that ORR is applicable on the level of pure state evolution of an isolated quantum system, as described by Eq. 3.29. In particular, we demonstrate the coincidence between the relaxation of the expectation value of a certain observable calculated from a single pure state picked randomly from slightly out-of-equilibrium conditions and its temporal correlation function at infinite temperature.

This coincidence can be the basis for a new algorithm to compute the correla-

tion function for systems for which we can not compute $\mathrm{Tr}\left\{\hat{A}(t)\hat{A}(0)\right\}$ directly. The core of the proposed algorithm to evaluate $\mathrm{Tr}\left\{\hat{A}(t)\hat{A}(0)\right\}$ for an observable $\hat{A}$ is to pick a random pure state representative of $\hat{\rho}_{neq}$, corresponding to a small deviation from equilibrium, and simply evolve it in time to evaluate the time dependence of $\langle\hat{A}\rangle$. This noticeably simple method would only require evolving the time-dependent Schrödinger equation with any numerical technique (i.e., Runge Kutta method) for the same time interval during which we want to evaluate $\mathrm{Tr}\left\{\hat{A}(t)\hat{A}(0)\right\}$, that would otherwise require exact diagonalization of the whole system. Since an accurate numerical evolution of the Schrödinger equation requires storing the Hamiltonian matrix as a sparse matrix (i.e., not necessarily a dense matrix) the memory required to compute a correlation function with this algorithm is roughly the memory required to store the nonzero elements of the Hamiltonian, i.e., the number of rows multiplied by the number of nonzero elements per row. This number scales as $N(\log N)^2$ for systems with long range interaction and $N(\log N)$ for systems with short range interaction. Although we apply our algorithm solely to quantum spin systems, the method is applicable to a generic strongly interacting many-body system.

A typical relaxation experiment for an observable $\hat{A}$ would involve switching on a perturbation proportional to $\hat{A}$ in the infinite past and switching it off at time $t = 0$ letting the system relax to equilibrium. This process corresponds to letting the system equilibrate under the Hamiltonian $\hat{\mathcal{H}}' = \hat{\mathcal{H}} + \epsilon\hat{A}$, where ϵ is a small coupling parameter, leading to an initial density matrix $\hat{\rho}\,(0) = e^{-\left(\hat{\mathcal{H}}+\epsilon\hat{A}\right)\alpha}$, with $\alpha = 1/kT$. Assuming that $\epsilon\hat{A} \gg \mathcal{H}$, as in NMR experiments, the initial density matrix is given by $\hat{\rho}\,(0) = e^{-\alpha\hat{A}}$.

We consider a 1D chain consisting of N_s spins 1/2 interacting by the nearest neighbor Heisenberg interaction, $\mathcal{H} = J\sum_i \mathbf{S_i}\cdot\mathbf{S_{i+1}}$ with periodic boundary condition. Here J is the coupling constant, and $\mathbf{S_i}$ is the spin operator on the $i^{\underline{\text{th}}}$ chain site. Such a chain admits periodic spin modulations with wave numbers $q = 2\pi n/N_s$, where n is an integer number taking values $0, 1, ..., N_s - 1$. For a given wave number q, the intermediate dynamic structure factor $I_q(t)$ at infinite temperature is defined as

$$I_q(t) \cong \mathrm{Tr}\left\{\hat{A}_{\{q\}}(t)\ \hat{A}_{\{-q\}}(0)\right\}, \tag{3.47}$$

where $\hat{A}_{\{q\}} = \frac{1}{\sqrt{N}}\sum_m \exp(iqm)S^x_m$. Since we have translation symmetry combined with periodic boundary conditions, we can show that $I_q(t)$ is also equivalent to

$\mathrm{Tr}\left\{\hat{A}_{\{q\}}(t)\ \hat{A}_{\{q\}}(0)\right\}$, where $\hat{A}_{\{q\}}$ is now defined as $\hat{A}_{\{q\}} = \frac{1}{\sqrt{2N}}\sum_m \cos(qm) S^x_m$.

In general, to generate an initial state $|\Psi_{\mathrm{neq}}\rangle$ for a generic operator $\hat{A}$, we can implement an imaginary-time Runge-Kutta algorithm to evaluate $|\Psi_{\mathrm{neq}}\rangle = \exp\left(-\hat{A}\alpha/2\right)|\Psi_{eq}\rangle$, where $|\Psi\rangle_{eq}$ is picked from an infinite temperature ensemble [109]. In our case, we select the basis to represent wavefunctions and operators such that $\hat{A}$ and consequently $\exp\left(-\hat{A}\alpha/2\right)$ are diagonal matrices, making the evaluation of $\exp\left(-\hat{A}\alpha/2\right)|\Psi_{eq}\rangle$ trivial.

We demonstrate in Fig. 3.4 the comparison between $I_q(t)$ evaluated by exact diagonalization for a 20 spin-1/2 chain and the relaxation function $\langle\Psi_{\mathrm{neq}}|\hat{A}(t)|\Psi_{\mathrm{neq}}\rangle$ for single pure states of Heisenberg chains consisting of 20 spins and 28 spins respectively. We see in this figure the excellent agreement between $\langle\Psi_{\mathrm{neq}}|\hat{A}(t)|\Psi_{\mathrm{neq}}\rangle$ and $I_q(t)$ that covers two orders of magnitude in the first case and three orders of magnitude in the second case. This excellent agreement demonstrates simultaneously the validity of Onsager regression relation (3.4) on the level of single pure states and the dynamical typicality relation (3.28). The difference between the accuracies of the two spin chains is consistent with the order of magnitude of the error in (3.28). The accuracy of the short spin chain can of course be improved by averaging over many pure states.

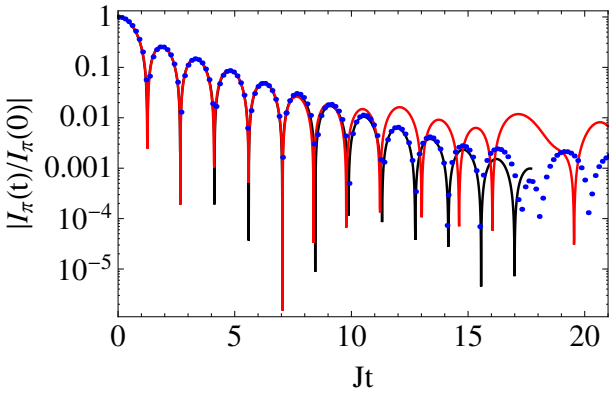

Figure 3.4: Intermediate dynamic structure factor $I_\pi(t)$ of the Heisenberg chain consisting of 20 spins 1/2, based on the exact trace formula (3.47) (dotted blue). The solid lines represent the relaxation of a single pure state $\langle\Psi_{\mathrm{neq}}|\hat{A}(t)|\Psi_{\mathrm{neq}}\rangle$ picked initially from a nonequilibrium ensemble towards equilibrium for a Heisenberg chain consisting of 20 spins (red) and 28 spins (black). The initial nonequilibrium ensemble is $\hat{\rho}(0) = \frac{1}{N}e^{-\alpha\hat{A}}$ with $\alpha = 1/12$ in the first case and $\alpha = 1/4$ in the second case. The good agreement between $\langle\Psi_{\mathrm{neq}}|\hat{A}(t)|\Psi_{\mathrm{neq}}\rangle$ and the exact trace formula demonstrates both the validity of the Onsager regression relation (3.4) on the level of single pure states and also the validity of the dynamical typicality relation (3.28).

3.4.3 Classical versus quantum: Numerical efficiency of computing correlation functions based on Onsager relation

Computing the correlation function in quantum systems using ORR has a clear numerical advantage over doing the same thing in classical systems. The mean square value of the equilibrium fluctuations in quantum systems is inversely proportional to the size of its Hilbert space. This is an essential quantum mechanical feature due to the fact that quantum evolution incorporates an evolution of a parallel superposition of all basis states of the Hilbert space. This severely suppresses the level of statistical fluctuations at equilibrium, leaving an ample range for the observable to relax from a relatively large nonequilibrium value, which still belongs to the linear response regime, to equilibrium. The idea of exploiting *quantum parallelism* and its self-averaging property has proved useful in other contexts [110]. In what follows, we give concrete arguments for the above statement.

From the central limit theorem, if we have N independent random variables, x_i, described by the same probability distribution having mean μ and standard deviation σ, then the average quantity $\bar{x} = \frac{1}{N}\Sigma_i x_i$ is described by a probability distribution having mean $= \mu$ and standard deviation $\frac{\sigma}{\sqrt{N}}$. The variable $X = \Sigma_i x_i$ is described by a probability distribution having mean $= N\mu$ and standard deviation $\sqrt{N}\sigma$. Applying this result to the fluctuations of the total magnetization of a classical spin system consisting of N_s spins at equilibrium, we find that the standard deviation of the fluctuations of the total magnetization at equilibrium is of order $\sqrt{N_s\langle S_{iz}^2\rangle}$. For a quantum spin $1/2$ system of the same size, the fluctuations of the total magnetization of a quantum state which is a weighted average of a superposition of 2^{N_s} eigenstates of $\hat{M}_x$ have an RMS of order $\frac{\sqrt{N_s\langle \hat{S}_{iz}^2\rangle}}{2^{N_s/2}} \simeq \frac{\sqrt{\mathrm{Tr}\{\hat{A}^2\}}}{N}$, where $\hat{A}$ represents the total magnetization operator. This result could have been reached directly from the correlation function $C(t,T)$ of the equilibrium fluctuations defined in 3.30. The RMS value of the amplitude fluctuations of $\langle\Psi_{\mathrm{eq}}|\hat{A}(t)|\Psi_{\mathrm{eq}}\rangle$ equals $\sqrt{C(0,T)}$ (see: (3.30) and (3.31)).

We illustrate in Fig. 3.5 a comparison between the fluctuation noise of the total magnetization for a classical and quantum spin $1/2$ systems consisting of 8 spins, where the previous estimates can be verified.

In actual experiments, the time series resulting from monitoring of the total magnetization at equilibrium (known as spin noise) is different than $\langle\Psi_{\mathrm{eq}}|\hat{A}(t)|\Psi_{\mathrm{eq}}\rangle$. Monitoring a small quantum system continuously would interfere severely with its

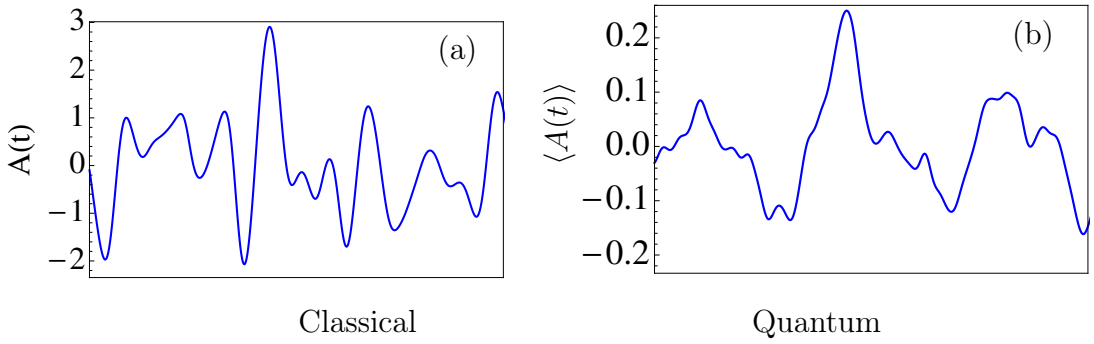

Figure 3.5: A comparison between the fluctuation noise of the total magnetization for a classical and quantum spin 1/2 systems consisting of 8 spins.

free evolution, and the measured signal of $\langle \hat{A}(t) \rangle$ would be far from the true equilibrium fluctuations of the perfectly isolated quantum system. It is legitimate to ask, how far does this apply to a macroscopic system that consists of a huge number of degrees of freedom? Does a monitoring of a single degree of freedom *damage* the information on the correlation function from the monitored signal? We have already seen that the RMS value of the fluctuations of an isolated system is expected to be of order $\frac{\sqrt{N_s \langle \hat{S}_{iz}^2 \rangle}}{2^{N_s/2}}$. On the other hand, the RMS value of spin noise in a monitored system consisting of N_s spins, as shown by F. Bloch [111]), is of order $\sqrt{N_s}$ i.e., exponentially larger than the former case. [1] Despite this difference, we expect that continuous monitoring of one single degree of freedom of the macroscopic system should not alter the dynamics that much and the information about $\mathrm{Tr}\left\{\hat{A}_\pi(t)\ \hat{A}_\pi(0)\right\}$ can still be retrieved from the monitored observable.

3.4.4 A more efficient method to compute correlation functions based on quantum dynamical typicality

Although the regression relation as implemented by (3.29) provides an accurate method to evaluate infinite temperature correlation functions, we provide an even more accurate method to evaluate $\mathrm{Tr}\left\{\hat{A}(t)\hat{A}(0)\right\}$, based on the dynamical typicality argument as well. The essence of this method is to pick an initial normalized state $|\Psi_{eq}\rangle$ from an equilibrium ensemble at infinite temperature and evaluate $\langle \Psi_{\rm eq}|\hat{A}(t)\hat{A}(0)|\Psi_{\rm eq}\rangle$. This amounts to approximating the Hilbert space average of

[1] The reason is that the system exists in a narrow range of the eigenstates of $\hat{M}_x$, according to the value of the measurement. Therefore, the RMS of the spin noise behaves like a classical spin system of the same size.

$\hat{A}(t)\hat{A}(0)$ by a single realization of $|\Psi_{\rm eq}\rangle$. From (3.24) and (3.25), we conclude that

$$\langle\Psi_{\rm eq}|\hat{A}(t)\hat{A}(0)|\Psi_{\rm eq}\rangle = \frac{1}{N}{\rm Tr}\left\{\hat{A}(t)\hat{A}(0)\right\} + \Delta, \tag{3.48}$$

where

$$\Delta^2 = \frac{1}{N+1}\left(\frac{{\rm Tr}\{\hat{A}(t)\hat{A}(0)\hat{A}(t)\hat{A}(0)\}}{N} - \left(\frac{{\rm Tr}\{\hat{A}(t)\hat{A}(0)\}}{N}\right)^2\right). \tag{3.49}$$

Noticing that the two terms in the RHS of (3.49) are of same order of magnitude, we can write

$$\langle\Psi_{\rm eq}|\hat{A}(t)\hat{A}(0)|\Psi_{\rm eq}\rangle = \frac{1}{N}{\rm Tr}\left\{\hat{A}(t)\hat{A}(0)\right\}\left[1 + O\frac{1}{\sqrt{N}}\right]. \tag{3.50}$$

By comparing (3.50) and (3.29), we observe that the statistical accuracy of this method is better than the one based on the regression relation by a factor $1/\alpha$.

To generate an initial state $|\Psi_{\rm eq}\rangle$ that samples an equilibrium infinite temperature ensemble, we consider an orthonormal eigenbasis $\{|\phi_k\rangle\}$ and generate

$$|\Psi_{\rm eq}\rangle = \sum_{k=1}^{N} a_k|\phi_k\rangle, \tag{3.51}$$

where a_k are quantum amplitudes whose magnitudes are drawn from the exponential probability distribution [112]

$$P(|a_k|^2) = N\exp(-N|a_k|^2), \tag{3.52}$$

and phases are chosen completely randomly. To draw random numbers $\{a_k\}$ that samples $P(|a_k|^2)$, we follow the inverse transform sampling method [113] as follows: We first draw a set of random numbers $\{r_k\}$ from a uniform probability distribution in the interval $[0,1]$, and equate each of them with the cumulative distribution function $C(|a_k|^2) = 1-\exp(-N|a_k|^2)$ corresponding to $P(|a_k|^2)$. Letting $r'_k = 1-r_k$, we find the values of $|a_k|^2$ from $|a_k|^2 = -\log(r'_k)/N$. The statistical fluctuations associated with $|a_k|^2$ cause the norm of $\Psi_{\rm eq}$ to slightly deviate from unity, $|\Psi_{\rm eq}|^2 = 1 + O(1/\sqrt{N})$. This deviation makes the statistical uncertainty in evaluating ${\rm Tr}\left\{\hat{A}(t)\hat{A}(0)\right\}$ to slightly differ from (3.49) according to

$$\langle\Psi_{\rm eq}|\hat{A}(t)\hat{A}(0)|\Psi_{\rm eq}\rangle = \frac{1}{N}{\rm Tr}\left\{\hat{A}(t)\hat{A}(0)\right\} + \Delta_2, \tag{3.53}$$

where

$$\overline{\Delta_2^2} = \frac{1}{N^2}{\rm Tr}\left\{\hat{A}(t)\hat{A}(0)\hat{A}(t)\hat{A}(0)\right\}. \tag{3.54}$$

To show this, let $\hat{A}(t)\hat{A}(0) = \hat{X}$, and consider the evaluation of $\langle\Psi_{\rm eq}|\hat{X}|\Psi_{\rm eq}\rangle$ in the eigenbasis of $\hat{X}$, which evolve with time. The variance of $\langle\Psi_{\rm eq}|\hat{X}|\Psi_{\rm eq}\rangle$ is given by

$$\overline{\Delta_2^2} = \overline{\left(\langle\Psi_{\rm eq}|\hat{X}|\Psi_{\rm eq}\rangle - \overline{\langle\Psi_{\rm eq}|\hat{X}|\Psi_{\rm eq}\rangle}\right)^2}, \tag{3.55}$$

where $\overline{\langle\Psi_{\rm eq}|\hat{X}|\Psi_{\rm eq}\rangle} = \sum_m \overline{|a_m|^2} X_{mm}$. According to the probability distribution (3.52), $\overline{|a_m|^2} = \frac{1}{N}$ and $\overline{|a_m|^4} = \frac{2}{N^2}$, therefore we have

$$\overline{\Delta_2^2} = \overline{\sum_m (|a_m|^2 - \frac{1}{N}) X_{mm} \sum_n (|a_n|^2 - \frac{1}{N}) X_{nn}}. \tag{3.56}$$

Since $\{|a_m|^2\}$ are uncorrelated, we find that for $m \neq n$, $\overline{(|a_m|^2 - \frac{1}{N})(|a_n|^2 - \frac{1}{N})} \cong 0$, and we are left with

$$\begin{aligned} \overline{\Delta_2^2} &= \sum_m \overline{\left(|a_m|^2 - \frac{1}{N}\right)^2} X_{mm}^2 \\ &= \sum_m \left(\overline{|a_m|^4} - \frac{1}{N^2}\right) X_{mm}^2 \approx \frac{1}{N^2} Tr\{\hat{X}^2\}, \end{aligned} \tag{3.57}$$

which is identical to (3.54). Imposing the normalization of $|\Psi_{\rm eq}\rangle$ will introduce correlations between $\{|a_m|^2\}$ and $\{|a_n|^2\}$. In this case, we have

$$\sum_{m\neq n} \overline{(|a_m|^2 - \frac{1}{N})(|a_n|^2 - \frac{1}{N})} X_{mm} X_{nn} \cong \left(\overline{(|a_m|^2|a_n|^2)} - \frac{1}{N^2}\right) \sum_{m\neq n} X_{mm} X_{nn} \tag{3.58}$$

For a normalized state, we know from Ref. [114] that $\overline{(|a_m|^2|a_n|^2)} = \frac{1}{N(N+1)}$. By letting $\sum_{m\neq n} X_{mm}X_{nn} \approx {\rm Tr}\{X^2\}^2$, we see that the term which remains amounts to the difference between $\overline{\Delta_2^2}$ in (3.54) and $\overline{\Delta^2}$ as defined in (3.49).

On the numerical side, the procedure to generate an evolution of $\langle\Psi_{\rm eq}|\hat{A}(t)\hat{A}(0)|\Psi_{\rm eq}\rangle$ for a single pure state proceeds as follows: First, we select $|\Psi_{\rm eq}\rangle$ from the equilibrium ensemble ρ_{eq} as explained earlier. We then define another state $|\Phi(0)\rangle = \hat{A}|\Psi_{\rm eq}(0)\rangle$ (i.e. $|\Phi(0)\rangle$ is not normalized). The quantity of interest $\langle\Psi_{\rm eq}|\hat{A}(t)\hat{A}(0)|\Psi_{\rm eq}\rangle$ is then evaluated as $\langle\Psi_{\rm eq}(t)|\hat{A}|\Phi(t)\rangle$, where $|\Phi(t)\rangle = \exp(-i\mathcal{H}t)|\Phi(0)\rangle$, and $|\Psi_{\rm eq}(t)\rangle = \exp(-i\mathcal{H}t)|\Psi_{\rm eq}(0)\rangle$. In Fig. 3.6, we show the result of such a computation for a Heisenberg chain consisting of 20 spins, compared with the trace formula for $I_\pi(t)$, both computed via exact diagonalization. This plot demonstrates clearly the improved performance of using $\langle\Psi_{\rm eq}|\hat{A}(t)\hat{A}(0)|\Psi_{\rm eq}\rangle$ over the relaxation function $\langle\Psi_{\rm neq}|\hat{A}(t)|\Psi_{\rm neq}\rangle$ in Fig. 3.4 for the same system size.

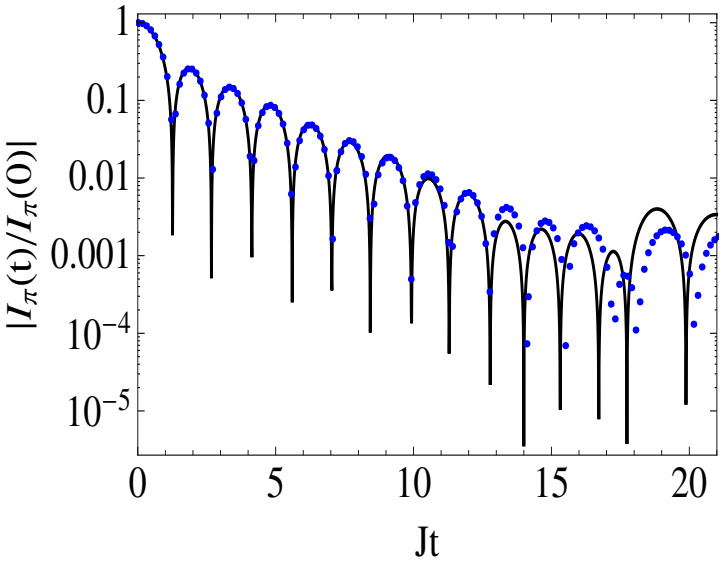

Figure 3.6: Intermediate dynamic structure factor $I_\pi(t)$ of a Heisenberg chain consisting of 20 spins 1/2, based on the exact trace formula (3.47) (dotted blue). The solid line represents the evolution of a single realization of $\langle\Psi_{\rm eq}|\hat{A}(t)\hat{A}(0)|\Psi_{\rm eq}\rangle$ computed for the same system by exact diagonalization. $|\Psi_{\rm eq}\rangle$ is picked from the equilibrium ensemble defined by (3.52). The agreement between $\langle\Psi_{\rm eq}|\hat{A}(t)\hat{A}(0)|\Psi_{\rm eq}\rangle$ and $I_\pi(t)$ is better than the relaxation function $\langle\Psi_{\rm neq}|\hat{A}(t)|\Psi_{\rm neq}\rangle$ for the same system size by a factor $1/\alpha$ that defines the initial nonequilibrium ensemble, $\rho_{\rm neq} = \frac{1}{N}\exp(-\alpha\hat{A})$, from which $|\Psi_{\rm neq}\rangle$ is selected.

3.4.5 Comparison between three numerical methods to compute correlation functions

In Fig. 3.7, we present a comparison between the three methods presented so far to approximate the exact trace formula for the infinite temperature correlation functions, namely:

1. The relaxation function $\langle\Psi_{\rm neq}|\hat{A}(t)|\Psi_{\rm neq}\rangle$ from a nonequilibrium to an equilibrium state (Eq. 3.29).

2. The expectation value of $\hat{A}(t)\hat{A}(0)$ evaluated from a single pure state picked from an infinite temperature ensemble, $\langle\Psi_{\rm eq}|\hat{A}(t)\hat{A}(0)|\Psi_{\rm eq}\rangle$ (Eq. 3.53).

3. The correlation function $C(t,T_0)$ defined in (3.30).

All of the computations were done by exact diagonalization based on single pure states (i.e., no averaging). In case of $C(t,T_0)$, the value of T_0 is $4200/J$. It is evi-

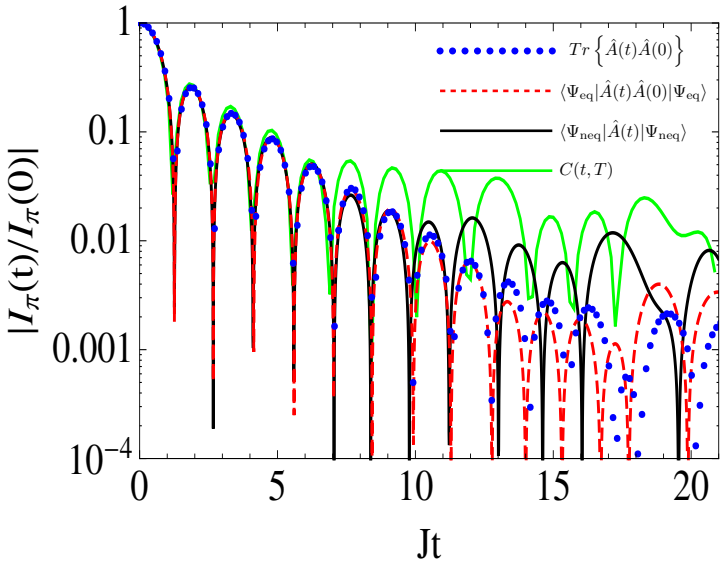

Figure 3.7: Intermediate dynamic structure factor $I_\pi(t)$ of the Heisenberg chain of 20 spins 1/2. The calculation based on the exact trace formula $\mathrm{Tr}\left\{\hat{A}_\pi(t)\ \hat{A}_\pi(0)\right\}$ is compared with the relaxation function $\langle\Psi_{\mathrm{neq}}|\hat{A}(t)|\Psi_{\mathrm{neq}}\rangle$ from a nonequilibrium to an equilibrium state (Eq. 3.29), the correlation function $C(t,T_0)$ defined in (3.30) and $\langle\Psi_{\mathrm{eq}}|\hat{A}(t)\hat{A}(0)|\Psi_{\mathrm{eq}}\rangle$ (Eq. 3.53). All calculations are based on the complete diagonalization of the Hamiltonian $\mathcal{H}$. Each of the three approximate calculations is done with a single pure state. In the case of Eq. (3.29), $\alpha = 0.083$, corresponding to an initial polarization equal to approximately 4 percent of the maximum polarization. In the case of Eq. (3.30), $T_0 = 4200/J$. As expected theoretically, the approximation based on Eq.(3.53) gives the most accurate agreement with the exact result. The accuracy of all three approximations can be improved by averaging over more pure states [4].

dent that $\langle\Psi_{\mathrm{eq}}|\hat{A}(t)\hat{A}(0)|\Psi_{\mathrm{eq}}\rangle$ gives the most accurate prediction for $\mathrm{Tr}\left\{\hat{A}_\pi(t)\ \hat{A}_\pi(0)\right\}$, in agreement with our theoretical expectation.

3.5 Summary

We investigated the Onsager regression relation on the level of pure quantum states close to equilibrium at high temperatures. We showed that the relaxation of pure states can serve as a simple and powerful technique to compute infinite temperature correlation functions in many-body quantum systems (Eq. 3.29). The validity of that technique is justified using the notion of quantum dynamical typicality, which states that the evolution of the expectation value of operators

computed by random pure states serve as a good approximation for the average over Hilbert space.

Our investigations of pure state relaxations and correlations of equilibrium fluctuations of observables led us to introduce a modified regression relation (Eq. 3.33). This relation connects the relaxation to equilibrium with the correlation of the equilibrium fluctuations treated as a classical time series.

The above results indicate that the quantum correlation function of some observable can be extracted from the time series of the expectation value of that observable generated by a single pure state.

Qantum dynamical typicality was employed in section 3.4.3 to introduce an even more efficient technique to compute correlation functions (Eq. 3.48) than the one based on ORR. A comparison between the efficiency of the two approaches is given in Fig. 3.7.

We anticipate that the recent progress in nonequilibrium dynamics of closed interacting quantum systems [115] will make use of the relaxation approach described in this chapter in quantum simulation experiments to evaluate correlation functions of complex many-body systems.

Most investigators accept the lack of chaos in finite, bounded, undriven, quantum systems with the same ease they accept the statement that a simple closed curve divides the plane into an inside and an outside. Yet the proof of both these results contains many subtleties [116].

Joseph Ford and Matthias Ilg

4

Sensitivity of quantum spin systems to small perturbations

As discussed in the first chapter, many criteria for chaotic behavior in nonintegrable quantum systems have been devised to discriminate it from integrable systems. Nevertheless, there is no consensus about how the basic indicator of chaos, that is exponential sensitivity to small perturbations, carries over to quantum systems (e.g., quantum spin systems).

A popular indicator of sensitivity to small perturbations in quantum systems is the quantum fidelity, defined as the overlap between the wavefunctions of perturbed and unperturbed systems. In this chapter, we first describe our investigations of the fidelity of quantum spin systems, from which we were not capable to discriminate integrable from nonintegrable dynamics. Afterwards, we follow a pedagogical approach and present initial trials to generalize the concept of distance between perturbed and unperturbed states in phase space to the quantum domain. Finally, we investigate manifestations of chaos under imperfect time reversal of spin dynamics, known as Loschmidt echo, in the behavior of the total magnetization. We show that for classical spin clusters, Loschmidt echo exhibits the exponential sensitivity to small perturbations characterized by the largest Lya-

punov exponent of the system. On the other hand, we show that quantum spin 1/2 systems do not exhibit exponential sensitivity to small perturbations in imperfect Loschmidt echo experiments.

Some of the indicators for quantum chaos proposed in this chapter are also applied to quantum spin systems with spin quantum number $S > 1/2$. The objective of investigating these systems is two-fold. First, to investigate the quantum to classical transition in quantum spin systems with regard to the onset of chaos. Second, to investigate whether the chaotic signatures of such a transition can be detected in NMR experiments on nuclear isotopes whose values of S are of the order of $S = 3$.

It is commonly believed that the classical behavior is reproduced by increasing the relevant quantum number of the problem. In the case of a quantum spin system, the classical limit is obtained by increasing the quantum spin number [117, 118], with the proper normalization of the spin operators, such that the energy spectrum approaches a continuum in the classical limit. Some of the questions relevant to chaos in the quantum-classical transition are: Do Lyapunov exponents exhibit a smooth transition towards their limiting values in the classical limit or a sharp transition? Can the exponential sensitivity to small perturbations be detected in numerical simulations performed on small clusters of large spins, without the need for taking the limit of large system sizes?

The main result of this chapter is that quantum spin 1/2 systems exhibit no exponential sensitivity to small perturbations.

4.1 Quantum fidelity

The defining property of chaos in classical dynamical systems is the instability of classical trajectories in phase space under small perturbations to the initial conditions. A possible generalization of this property to quantum systems can be given in terms of the stability of the wavefunction of the system $|\psi(t)\rangle$ under perturbations to the Hamiltonian itself. The standard way to measure the *closeness* between $|\psi(t)\rangle$ evolved by the Hamiltonian H and $|\psi'(t)\rangle$ evolved by the Hamiltonian $H + \delta H(t)$, i.e., the fidelity of the evolution, is to measure the overlap between $|\psi(t)\rangle$ and $|\psi'(t)\rangle$

$$\mathcal{O}(t) = |\langle\psi(t)|\psi'(t)\rangle|.^{1} \tag{4.1}$$

[1] Fidelity is normally defined as the square of this quantity.

In 1984, Asher Peres proposed that the fidelity function has the promise to distinguish integrable from nonintegrable systems [25]. Peres suggested that $\mathcal{O}(t)$ decays more substantially for a nonintegrable system than an integrable one, i.e., nonintegrable systems are less stable to perturbations. In the more general case where the initial state is a mixed state represented by the density matrix $\rho(0)$, the overlap between the perturbed and unperturbed systems is given by $\mathcal{O}(t) = \mathrm{Tr}\{\rho'(t)\rho(t)\}^{1/2}$.

The concept of fidelity is closely connected with the Loschmidt echo experiments [119] which measure the reversibility of the dynamics subject to perturbations [120]. When the system is propagated for a time t with the unperturbed Hamiltonian H and then propagated backward for time t with the perturbed Hamiltonian H_δ, the fidelity of the evolution is defined in terms of the overlap between the initial and final state,

$$\mathcal{O}(t) = |\langle\psi(0)|e^{iH_\delta t/\hbar}e^{-iHt/\hbar}|\psi(0)\rangle|. \tag{4.2}$$

When the initial state is a Gaussian wavepacket, the overlap between the perturbed and unperturbed evolutions was indeed shown to decay exponentially in quantum systems whose classical counterpart is chaotic (more precisely when the initial state of the wavepackets correspond to chaotic region in the mixed phase space of the classical system) [121] and the rate of exponential decay was even connected with the Lyapunov exponent in the classical limit [122].

In the following, we acquaint ourselves with the behavior of $\mathcal{O}(t)$ for different types of perturbations to quantum spin systems and in the next subsection we compare the behavior of $\mathcal{O}(t)$ for integrable and nonintegrable systems.

First, let us consider a time-independent perturbation $\delta H(t) = \delta H$. The time evolution operator of the perturbed Hamiltonian is given by:

$$U(t) = e^{-\frac{i}{\hbar}(H+\delta H)t}. \tag{4.3}$$

According to the Baker-Campbell-Hausdorff theorem[123], $U(t)$ is equivalent to $e^{-\frac{i}{\hbar}Ht}e^{-\frac{i}{\hbar}(\delta H)t}$ only when $[H, \delta H] = 0$. In this case, $\mathcal{O}(t) = \langle\psi(0)|e^{-\frac{i}{\hbar}\delta Ht}|\psi(0)\rangle$.

Consider a quantum spin chain with the nearest neighbor interaction Hamiltonian

$$H = \sum_i J_x \mathbf{S_i}^x \mathbf{S_{i+1}}^x + J_y \mathbf{S_i}^y \mathbf{S_{i+1}}^y + J_z \mathbf{S_i}^z \mathbf{S_{i+1}}^z,$$

and a perturbation field that couples to the total spin polarization, $\delta H = \delta \sum_i \mathbf{S_i}^z$. We let $\hbar = 1$ in the rest of this chapter. We show in Fig. 4.1 that $\mathcal{O}(t)$ can ex-

hibit both oscillatory behavior and monotonic decay, depending on the interaction coefficients of the system, J_x, J_y and J_z.

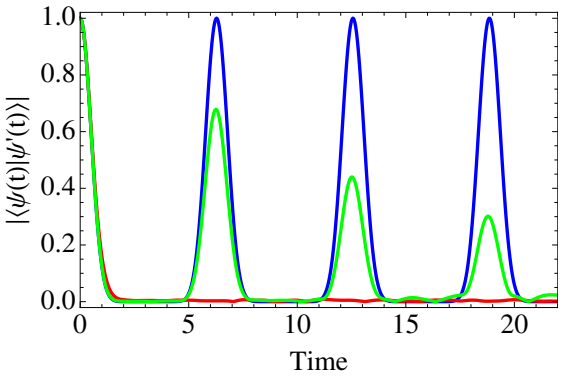

Figure 4.1: The overlap function $\mathcal{O}(t)$ for the wave functions of the perturbed and unperturbed quantum spin chains consisting of 16 spins whose Hamiltonian is $H = \sum_i J_x \mathbf{S_i}^x \mathbf{S_{i+1}}^x + J_y \mathbf{S_i}^y \mathbf{S_{i+1}}^y + J_z \mathbf{S_i}^z \mathbf{S_{i+1}}^z$ and perturbation Hamiltonian $\delta H = \delta \sum_i \mathbf{S_i}^z$. The vlaues of the coupling coefficients are $J_x = J_y = \sqrt{3}, J_z = 0$ (blue), $J_y = J_z = \sqrt{3}, J_x = 0$ (red) and $J_x = \sqrt{2}, J_y = \sqrt{6/5} J_z = \sqrt{14/5}$ (green). In all cases, $\delta = 1.0$ and the initial state $|\psi(0)\rangle$ is a completely random state.

We notice from the blue curve in Fig. 4.1 that $\mathcal{O}(t)$ exhibits complete recurrences in the case when $[H, \delta H] = 0$. We may anticipate that the more accurately the time evolution operator of the perturbed system can be approximated by the product $e^{-\frac{i}{\hbar}(H)t} e^{-\frac{i}{\hbar}(\delta H)t}$, the stronger the recurrences in $\mathcal{O}(t)$. We illustrate this expectation by computing the difference between the exact evolution operator and the product $e^{-\frac{i}{\hbar}(H)t} e^{-\frac{i}{\hbar}(\delta H)t}$ for $t = \hbar = 1$ and $\delta = 0.1$ for both the anisotropic XYZ model, which exhibits recurrences, and the YY model, which does not exhibit recurrences in the case of a 2-spin system

$$e^{-i(H_{XYZ}+\delta H)t} - e^{-iH_{XYZ}t} e^{-i\delta Ht} = \begin{bmatrix} 0.00021e^{0.65\pi i} & 0 & 0 & 0.0079e^{-0.85\pi i} \\ 0 & 0 & 0 & 0 \\ 0 & 0 & 0 & 0 \\ 0.0079e^{0.12\pi i} & 0 & 0 & 0.00021e^{-0.38\pi i} \end{bmatrix},$$

$$e^{-i(H_{YY}+\delta H)t} - e^{-iH_{YY}t} e^{-i\delta Ht} = \begin{bmatrix} 0.0061e^{0.38\pi i} & 0 & 0 & 0.042e^{-0.13\pi i} \\ 0 & 0 & 0 & 0 \\ 0 & 0 & 0 & 0 \\ 0.042e^{0.85\pi i} & 0 & 0 & 0.0061e^{-0.65\pi i} \end{bmatrix}. \quad (4.4)$$

We note that the elements of the difference matrix in the first case are one order of magnitude smaller than in the second case, which confirms the claim made above.

As for the rate of decay of $\mathcal{O}(t)$, the higher the strength of δH (i.e., stronger perturbation), the faster the overlap decays to zero.

On the dynamic side, when the perturbation is time-dependent, $\delta H(t) = \delta H f(t)$, the slower the variation of $f(t)$ (i.e., adiabatic perturbation) the faster the decay of $\mathcal{O}(t)$. In Fig. 4.2 , we illustrate the overlap for a generic nonintegrable quantum spin chain with next nearest neighbor interaction, for constant perturbation compared with the same perturbation modulated sinusoidally at different frequencies.

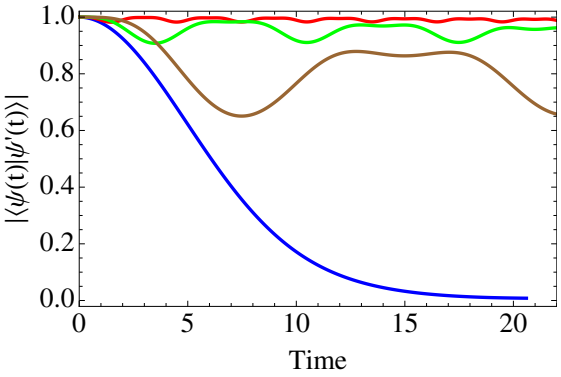

Figure 4.2: The overlap function $\mathcal{O}(t)$ for the wave functions of the perturbed and unperturbed nonintegrable quantum spin chains consisting of 16 spins 1/2 with Hamiltonian $H = \sum_i J_x \mathbf{S_i}^x \mathbf{S_{i+1}}^x + J_y \mathbf{S_i}^y \mathbf{S_{i+1}}^y + J_z \mathbf{S_i}^z \mathbf{S_{i+1}}^z + 0.3(J_x \mathbf{S_i}^x \mathbf{S_{i+2}}^x + J_y \mathbf{S_i}^y \mathbf{S_{i+2}}^y + J_z \mathbf{S_i}^z \mathbf{S_{i+2}}^z) + \sum_i h_i \mathbf{S_i}^z$ where h_i is a random field in the range $[-0.1, 0.1]$. The perturbations to the Hamiltonian are $\delta H(t) = \delta H \equiv 0.1 \sum_i \mathbf{S_i}^z$ (blue), $\delta H(t) = \delta H \sin(\frac{2\pi}{3} t)$ (red), $\delta H(t) = \delta H \sin(\frac{2\pi}{7} t)$ (green) and $\delta H(t) = \delta H \sin(\frac{2\pi}{15} t)$ (brown).

We now pose an important question: Can we find for a certain Hamiltonian H and perturbation δH *a resonance frequency* at which $\mathcal{O}(t)$ decays faster than lower frequencies as well as higher frequencies? From a simple scan over frequencies, the answer to this question seems negative; i.e., there is no *quantum resonance* in the sense defined above [2]. No further investigations of the above questions is presented in this thesis.

[2]This definition of resonance should be distinguished from quantum resonances in NMR experiments where the total magnetic polarization, not the wave function, is the quantity of interest and also from the nonlinear quantum resonances discussed in [124].

4.1.1 Fidelity decay for integrable and nonintegrable quantum spin systems

We examine in this part the decay of $\mathcal{O}(t)$ for both integrable and nonintegrable quantum spin lattices. The strength of the perturbation Hamiltonian has to be sufficiently weak so that it does not change the character of the dynamics (e.g., break the integrability), and in the same time not extremely weak so that we can observe a considerable decay of $\mathcal{O}(t)$ in a finite time.

We consider for the integrable system an XXZ spin chain consisting of 24 spins and for the nonintegrable system a 2D XXZ spin lattice consisting of 4×6 spins. The coupling constants are $J_x = J_y = \sqrt{2/3}$, $J_z = -\sqrt{5/3}$ while the perturbation is taken to be a longitudinal magnetic field in the z direction of strength =0.1. It is evident that the perturbation does not change the type of integrability in both cases since it commutes with the Hamiltonian.

In Fig. 4.3, we show the level spacing distribution $P(s)$ for a single matrix block of the later system in the translation-invariant basis corresponding to wavevectors $k_x = 2\pi/4$, $k_y = 2\pi/6$ (see chapter 1) and total magnetization in the z-direction $\sum_i S_i^z = 8.5$. This figure shows that $P(s)$ follows closely the Wigner-Dyson distribution of the Gaussian orthogonal ensemble, $P(s) = \frac{\pi s}{2} e^{-\pi s^2/4.0}$. This implies an underlying nonintegrable dynamics according to the Bohigas-Giannoni-Schmit conjecture [28].

We found out, as depicted in Fig. 4.4, that the decay of $\mathcal{O}(t)$ is almost indistinguishable for the integrable and nonintegrable cases. That confirms the belief that fidelity is not in general a good measure for quantum chaos or the complexity of quantum motion [125].

To investigate whether this quantity shows better distinction between integrable and nonintegrable systems in the classical limit (i.e., large values of the spin quantum number S), we considered two chains of spin-10. The first one is an Ising chain, which is guaranteed to be integrable for an arbitrary S, and the second one has an XXZ Hamiltonian, which is known to have a nonzero Lyapunov exponent in the classical limit [19]. The comparison of $\mathcal{O}(t)$ depicted in Fig. 4.4-b for the two systems illustrates again that $\mathcal{O}(t)$ is incapable of distinguishing between them.

We point out that this observation contradicts the conclusion of J. Emerson et. al. in [126] from studying kicked tops that "exponential (nonexponential) fidelity decay can be correlated with the presence (absence) of characteristic RMT

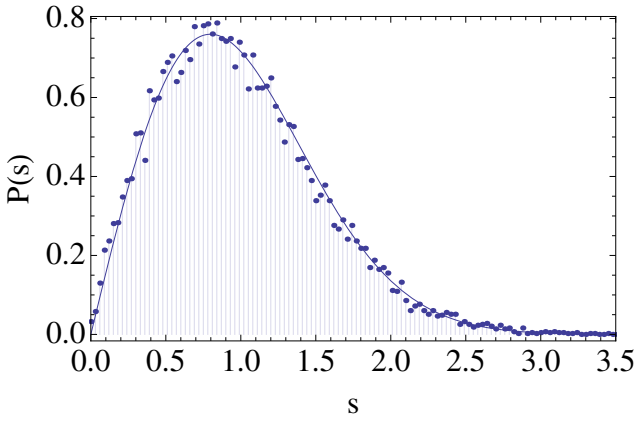

Figure 4.3: The probability of the level spacing s of the energy levels for the Hamiltonian matrix block corresponding to $K_x = 2\pi/4$, $K_y = 2\pi/6$ and $S_z^T = 8.5$ of an XXZ spin 1/2 lattice consisting of 6x4 spins. The solid curve is the Wigner-Dyson distribution function $\frac{\pi s}{2} e^{-\pi s^2/4.0}$. The energy levels have been renormalized (unfolded) such that the mean level spacing =1.

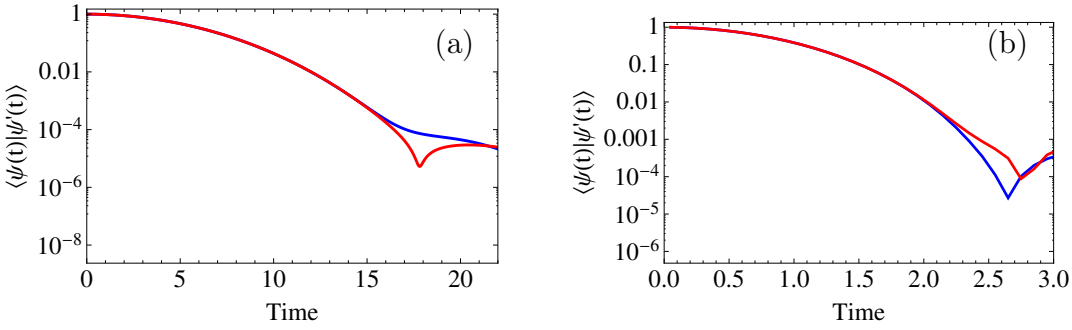

Figure 4.4: **(a)**: The overlap function $\mathcal{O}(t)$ for an integrable XXZ spin chain consisting of 24 spins with coupling constants $J_x = J_y = \sqrt{2/3}$, $J_z = -\sqrt{5/3}$, (blue) compared to a nonintegrable 6×4 XXZ spin lattice on logarithmic scale(red). **(b)**: $\mathcal{O}(t)$ for a 5 spin-10 chain with Ising coupling coefficients (blue) and XXZ coupling coefficients (red). The perturbation is taken to be a longitudinal magnetic field (in the z direction) of strength =0.1.

(random matrix theory) spectral fluctuations in the unperturbed system provided that the applied perturbation commutes with a system coordinate".

We finally investigate whether the survival probability $P(t)$, defined as $|\langle\psi(t)|\psi(0)\rangle|^2$, behaves differently for integrable and nonintegrable quantum spin systems. The quantity $P(t)$ vaguely defines the memory that the system retains of its initial conditions. We observe in Fig. 4.5 that $P(t)$ behaves qualitatively the same in

the integrable 1D XXZ and nonintegrable 2D XXZ systems.

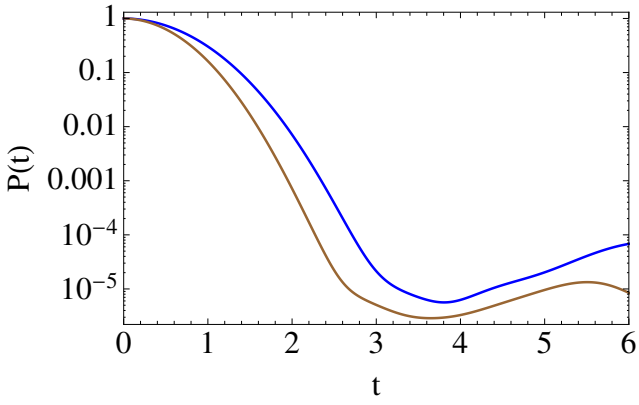

Figure 4.5: The survival probability $P(t)$ for an integrable XXZ spin chain, with coupling coefficients $J_x = J_y = 0.612$ and $J_z = -0.5$ (blue) compared to a nonintegrable 5×4 XXZ spin lattice with coupling coefficients $J_x = J_y = 0.433$ and $J_z = -0.353$ (brown) on logarithmic scale. In both cases, $P(t)$ is computed by averaging over 10 initial conditions.

4.2 Elementary attempts to define a quantum Lyapunov exponent

Do quantum systems exhibit an exponential sensitivity to perturbations or initial conditions analogous in any form to the exponential sensitivity that characterizes classical chaotic systems? This is an unsettled issue. Let us discuss the various points of view.

The primary argument for those who support the absence of exponential sensitivity in quantum systems is that quantum mechanics is intrinsically linear, and therefore the quantum amplitudes, which define all measurable properties, do not suffer from the nonlinearity which dominates the behavior of chaotic classical systems and leads to exponential sensitivity. Therefore, exponential sensitivity should not appear even in quantum systems which have chaotic classical limits, as another *quantum chaos* signature. Moreover, the very nature of quantum mechanics and the Heisenberg uncertainty principle makes the notion of arbitrarily close points in a phase space meaningless [127]. In addition, the discreteness of energy spectrum of bound quantum systems makes the evolution of any observable periodic or quasi-periodic, and this opposes the randomness generated by the Lyapunov

instability.

On the other hand, it is widely believed that at the proper limits of large quantum numbers or small Planck's constant, the classical behavior should be restored from the quantum laws of motion. If a quantum system that has a chaotic classical counterpart is initialized with a very narrow wavepacket, the evolution of the wavepacket will follow the classical trajectory for a finite time interval (and hence exhibits hypersensitivity to initial conditions) as outlined in chapter 1. Moreover, the force that govern all of the classical effects observable on everyday scale is the electromagnetic force, which is fundamentally described by quantum electrodynamics. Even when decoherence effects through the interaction with some environment are invoked in order to reproduce classical behavior [3], one might argue that the environment itself is inherently described by the quantum laws.

Blümel and Esser [128] have introduced an important classification of quantum systems with respect to their ability to incur exponential sensitivity. Type I includes quantum systems which are chaotic in the classical limit, and exhibits quasi-periodic behavior and no exponential sensitivity (at least in the long time limit), despite showing some or all of the quantum chaology hallmarks. Type II are quantum systems which are coupled to classical degrees of freedom and show exponential sensitivity. Type III are quantum systems that intrinsically exhibit exponential sensitivity as a pure quantum effect. At the time of writing their paper, Blumel and Esser admitted that type III was an empty set, in their words "fully quantized systems exhibiting all the ear-marks of classical chaos are presently not known". It is the aim of this section to investigate whether nonintegrable quantum spin systems belong to type III.

The basic idea of our investigation is to try to compensate for the lack of the notion of a phase space in macroscopic quantum spin systems by exploiting the huge number of degrees of freedom to define new quantities that behave in a classical manner. This agenda is similar to the vision of Mendes [129] who declares that "non-trivial statements (about the sensitivity of quantum systems to perturbations) have necessarily to involve expectation values of operators". It is for these considerations that many researchers [122, 129–132] over the last two decades have not given up on defining Lyapunov exponents for quantum systems. We admit that any time-independent quantum spin system consisting of a finite

[3] M. Berry phrases it as "'decoherence' suppresses the quantum suppression of chaos" [44].

number of spins is integrable [133], and true chaotic behavior can only appear in the limit of infinite number of spins or infinite quantum spin number. However, the hope is to detect any precursors of this chaotic behavior during the transition to either of these limits.

The aim of this section is to try to define an intrinsic quantum quantity that exhibits exponential growth, exclusive for nonintegrable systems, analogous to the exponential growth of distance between orbits in the classical phase space for chaotic classical systems. Previous trials to define quantal Lyapunov exponents in this spirit made use of Bohmian trajectories to introduce a meaningful distance measure [132]. It is clear that for small enough perturbations that does not resolve the spacings between the energy levels of the quantum system, there is no big chance to find exponential sensitivity. However, the hope is to find some regime of perturbations where this sensitivity will show up. The ultimate goal is to find some macroscopic quantity that depends sensitively on small perturbations of the quantum system and can be measured in NMR experiments.

We consider two types of perturbations:

(i) Perturbations in the initial state $|\psi(0)\rangle$.

(ii) Perturbations in the Hamiltonian $\mathcal{H}$.

We concentrate mainly on spin 1/2 systems, but show also simulation results for spin higher than 1/2 in order to investigate the transition to the classical spin limit.

Let us suppose that a random wavefunction $|\psi\rangle$ is subjected to a small perturbation. A possible way to implement perturbation in quantum spin systems is to rotate each spin slightly around some random axis. We take the rotation axis for each spin to be either $\vec{x}$, $\vec{y}$ or $\vec{z}$. Therefore, we can write the perturbed state $|\psi'\rangle$ as

$$|\psi'\rangle = \hat{\mathcal{R}}|\psi\rangle, \tag{4.5}$$

where $\hat{\mathcal{R}} = \prod_i e^{-i\theta_i S_i^{\hat{\alpha}_i}}$, i is an index running over all spins, α_i is either x, y, or z and θ_i is a small random angle. When a classical system is perturbed, the new state of the system is completely distinguishable from the old state. To approximate this condition in quantum systems, we let one of the rotation angles θ_i be $\pi/2$.

If we consider a nonintegrable classical spin system and denote a trajectory by the coordinates of all spins, $\bar{\mathbf{X}} \equiv \{S_{1x}, S_{1y}, S_{1z}, S_{2x}, S_{2y}, S_{2z}, ...\}$, and the distance vector between two trajectories by $\bar{\mathbf{D}}(t)$, where

$$\bar{\mathbf{D}}(t) \equiv \bar{\mathbf{X}}\left(t, \bar{\mathbf{X}}_0 + \bar{\mathbf{D}}_0\right) - \bar{\mathbf{X}}\left(t, \bar{\mathbf{X}}_0\right), \tag{4.6}$$

then $|\bar{\mathbf{D}}(t)|^2$ would grow exponentially by a rate determined by twice the maximum Lyapunov exponent, as shown in Fig. 4.6-d.

The naive attempt to define a distance $d(t)$ for a quantum system between perturbed and unperturbed evolution in the Euclidean sense leads to

$$d^2(t) = \sum_{i,\alpha_i} \left(\langle \psi'(t) | \hat{S_i^{\alpha_i}} | \psi'(t) \rangle - \langle \psi(t) | \hat{S_i^{\alpha_i}} | \psi(t) \rangle \right)^2, \tag{4.7}$$

which can be rewritten in terms of the time evolution operator as

$$d^2(t) = \sum_{i,\alpha_i} \left(\langle \psi(0) | \mathcal{R}^* e^{i\mathcal{H}t} \hat{S_i^{\alpha_i}} e^{-i\mathcal{H}t} \mathcal{R} | \psi(0) \rangle - \langle \psi(0) | e^{i\mathcal{H}t} \hat{S_i^{\alpha_i}} e^{-i\mathcal{H}t} | \psi(0) \rangle \right)^2. \tag{4.8}$$

A proper measure of any exponential growth of $d(t)$ should take into account averaging over many initial states $|\psi(0)\rangle$. It is clear that, in experiments, we do not have access to the measurement of all the components $S_i^{x,y,z}$, and a more realistic situation would be to consider one macroscopic operator such as $\sum_i \hat{S_i^x}$. We will adopt this approach in the next section.

We show in Fig. 4.6-a a comparison of $d^2(t)$ for an XXZ system of 4×3 spins with coupling coefficients $J_x = J_y = \sqrt{\frac{3}{16}}$ and $J_z = -\frac{1}{8}$ and an integrable XXZ spin chain consisting of 12 spins with coupling coefficients $J_x = J_y = \sqrt{\frac{3}{8}}$ and $J_z = -0.5$. Each plot represents averaging over 100 different initial states. The figure indicates a difference in $d^2(t)$ between the two systems. However, trying with another nonintegrable system which is an XYZ chain with coupling coefficients $J_x = \sqrt{\frac{1}{3}}$, $J_y = \sqrt{\frac{1}{5}}$ and $J_x = -\sqrt{\frac{7}{15}}$ and next nearest neighbor of strength 30% of the nearest neighbor coefficients, we notice, as in Fig. 4.6-b, that it almost coincides with the integrable XXZ chain. Therefore, we attribute the difference in Fig. 4.6-a to the dimensionality rather than the integrability. In Fig. 4.6-c, we show the level spacings statistics for the eigenvalues of the XYZ chain, to demonstrate its nonintegrability.

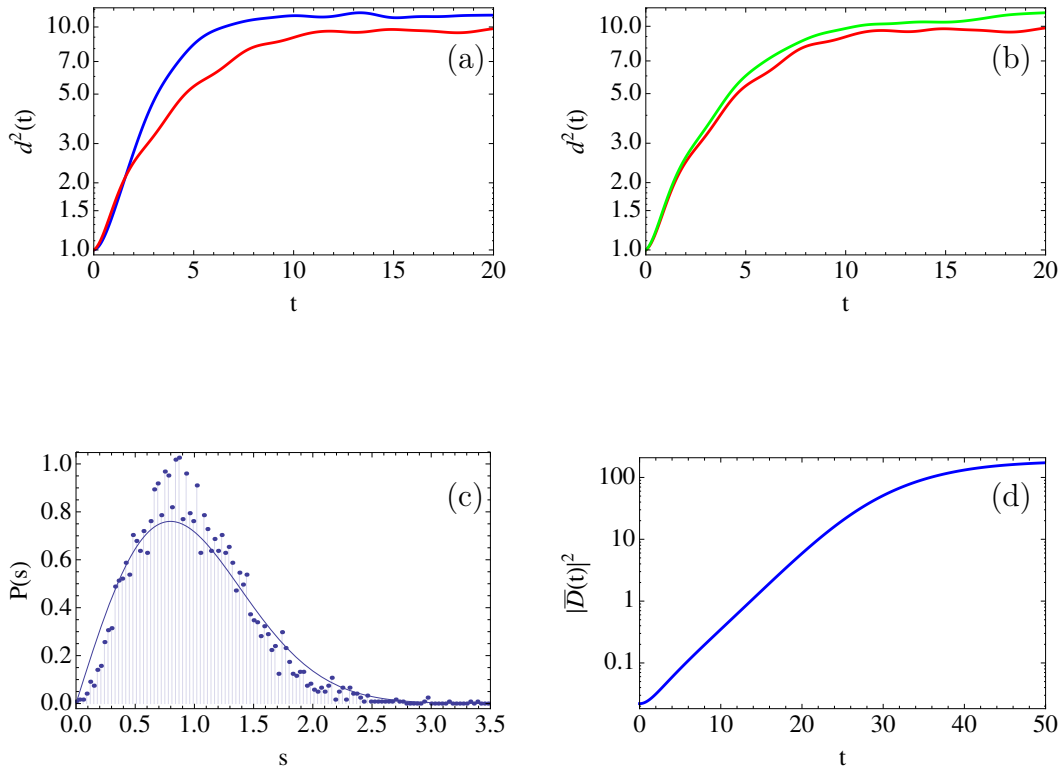

Figure 4.6: **(a)** $d^2(t)$ computed for a 2D spin 1/2 XXZ lattice consisting of 4×3 spins with coupling coefficients $J_x = J_y = \sqrt{\frac{3}{16}}$ and $J_z = -\frac{1}{8}$, (blue) and a spin 1/2 XXZ chain consisting of 12 spins, with coupling coefficients $J_x = J_y = \sqrt{\frac{3}{8}}$ and $J_z = -0.5$, (red). **(b)** Same as (a), for a nonintegrable XYZ chain with coupling coefficients $J_x = \sqrt{\frac{1}{3}}$, $J_y = \sqrt{\frac{1}{5}}$ and $J_x = -\sqrt{\frac{7}{15}}$ and next nearest neighbor (NNN) interaction of strength 30% of the nearest neighbor coefficients (green) and an XXZ chain (red). **(c)** Level spacing statistics for the XYZ with NNN coupling Hamiltonian computed for a single Hamiltonian matrix block corresponding to $k_x = \frac{2\pi}{18}$ of an 18-spin chain. **(d)** The phase space distance $|\bar{\mathbf{D}}(t)|^2$ between a perturbed and unperturbed trajectory for a nonintegrable classical spin chain consisting of 100 spins, averaged over 10000 trajectories. The perturbation is done by rotating each spin randomly around a random direction by an angle in the range $[-\pi/100, \pi/100]$.

4.2.1 Novel quantifiers of sensitivity in quantum systems

As a first improvement, we define a new quantity, $\wp(t)$, which captures the essence of $d^2(t)$ and implements the averaging as a trace operation over the whole Hilbert

space as

$$\wp(t) = \mathrm{Tr} \sum_{i,\alpha_i} \left(\mathcal{R}^* e^{i\mathcal{H}t} \hat{S_i^{\alpha_i}} e^{-i\mathcal{H}t} \mathcal{R} - e^{i\mathcal{H}t} \hat{S_i^{\alpha_i}} e^{-i\mathcal{H}t} \right)^2 . \tag{4.9}$$

In this step, we have replaced the classical variables in the phase space distance by quantum operators rather than quantum expectation values as in Eq. 4.7. To compute this quantity, we work in the eigenbasis of the Hamiltonian in order to be able to evaluate the time evolution operators $e^{\pm i\mathcal{H}t}$. Therefore, we are limited to a small number of spins.

In the rest of this section, we choose as a benchmark for an integrable system the Bethe integrable XXZ spin $\frac{1}{2}$ chain with coupling coefficients $J_x = J_y = \sqrt{\frac{3}{8}}$ and $J_z = -0.5$. We choose two types of nonintegrable systems. The first is an XYZ chain with coupling coefficients $J_x = \frac{1}{\sqrt{14}}$, $J_y = \frac{2}{\sqrt{14}}$ and $J_x = -\frac{3}{\sqrt{14}}$ and next nearest neighbor of strength 30% of the nearest neighbor coefficients. The second nonintegrable system is a 2D XXZ lattice with coupling coefficients equal to $\frac{1}{\sqrt{2}}$ of the coefficients of the integrable system. When comparing quantum spin systems with different spin quantum number, the coupling constants of the Hamiltonians should be scaled such that the time scale of different systems is the same. This is achieved by dividing the coupling constants by $\sqrt{S(S+1)}$, where S is the quantum spin number.

We show in Fig. 4.7 $\wp(t)$ computed for the three spin 1/2 systems. We notice that $\wp(t)$ exhibits a very similar behavior for the integrable and nonintegrable spin 1/2 chains. On the other hand, there is a noticeable difference in $\wp(t)$ between 1D and 2D systems.

In Fig. 4.8, we present the results for $\wp(t)$ computed for XXZ chains with spin quantum numbers: $1/2, 1$ and $3/2$. Note that in this case, all rotations are implemented around the z-direction. The reason is that the elementary basis in which the eigenbasis of the Hamiltonian is represented is the Ising basis in the z-direction, and in this case $\mathcal{R}$ is diagonal. While for spin-1/2, the operator $R_\alpha(\mathbf{n}) = \exp(-i\frac{\alpha}{2}\vec{\sigma}\cdot\mathbf{n})$ has a simple form: $R_\alpha(\mathbf{n}) = \cos\left(\frac{\alpha}{2}\right) - i\vec{\sigma}\cdot\mathbf{n}\sin\left(\frac{\alpha}{2}\right)$, there is no such simple form for rotation operators of higher spins. We notice a clear contrast between spin 1/2 and higher spins. This difference may not be associated with the breaking of integrability, as we noticed in Fig. 4.7-b. The limited range available for the growth of $\wp(t)$ in the higher spin case, which depends on the number of spins in the system, makes it difficult to detect any sign of extended exponential growth.

In order to compute $\wp(t)$ for bigger spin clusters, we resort to the quantum

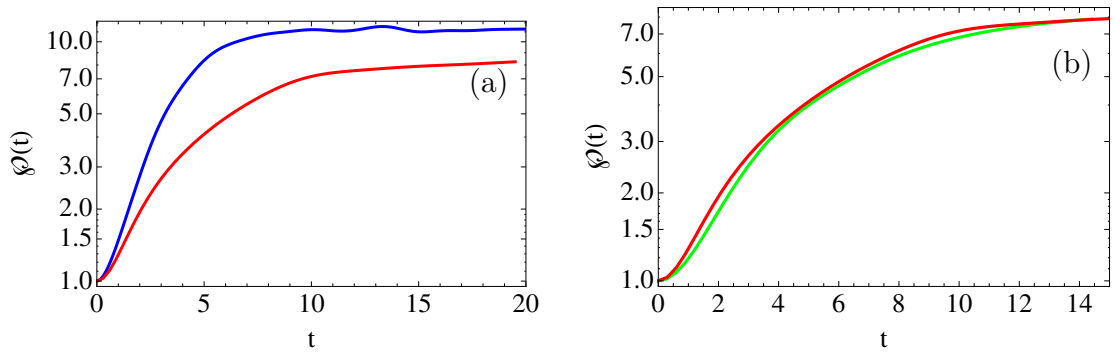

Figure 4.7: **(a)** $\wp(t)$ computed for a 2D spin 1/2 XXZ lattice consisting of 4×3 spins (blue) and a spin 1/2 XXZ chain composed of 13 spins (red). **(b)** Same as (a), for a nonintegrable XYZ chain consisting of 13 spins 1/2 with next nearest neighbor interaction (green) and an XXZ spin 1/2 chain (red). See the text for the parameters of the Hamiltonians.

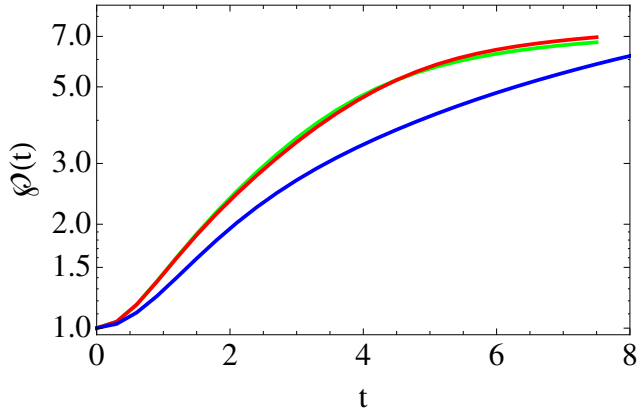

Figure 4.8: $\wp(t)$ computed for an XXZ 13-spin chain, spin quantum number 1/2 (blue), 7-spin chain, spin quantum number 1 (red) and 6-spin chain, spin quantum number 3/2 (green).

typicality approach described in chapter 3. Instead of computing the trace over the whole Hilbert space, we consider one single wavefunction, $|\psi\rangle$ and use it to compute the expectation value of the 'traced' operator in Eq. 4.9. Let us define the new quantity $\chi(t)$ that computes $\wp(t)$ based on a single pure state calculation.

After expanding the square bracket in 4.9, we arrive at

$$\begin{aligned}\wp(t) \approx \chi(t) \equiv \sum_{i,\alpha_i} & \langle\psi|e^{i\mathcal{H}t}{\hat{S_i^{\alpha_i}}}^2 e^{-i\mathcal{H}t}|\psi\rangle + \langle\psi|\mathcal{R}^* e^{i\mathcal{H}t}{\hat{S_i^{\alpha_i}}}^2 e^{-i\mathcal{H}t}\mathcal{R}|\psi\rangle \\ & - \langle\psi|\mathcal{R}^* e^{i\mathcal{H}t}\hat{S_i^{\alpha_i}} e^{-i\mathcal{H}t}\mathcal{R} e^{i\mathcal{H}t}\hat{S_i^{\alpha_i}} e^{-i\mathcal{H}t}|\psi\rangle \\ & - \langle\psi|e^{i\mathcal{H}t}\hat{S_i^{\alpha_i}} e^{-i\mathcal{H}t}\mathcal{R}^* e^{i\mathcal{H}t}\hat{S_i^{\alpha_i}} e^{-i\mathcal{H}t}\mathcal{R}|\psi\rangle.\end{aligned} \tag{4.10}$$

By noticing that for spin 1/2, ${S_i^{\alpha_i}}^2 = \mathbb{1}$, which makes the first two terms constants, and that the last two terms are the complex conjugate of each other, we can write $\chi(t)$ as

$$\chi(t) = \sum_{i,\alpha_i} \left(0.5 - 2\ Re\langle\psi|e^{i\mathcal{H}t}\hat{S_i^{\alpha_i}} e^{-i\mathcal{H}t}\mathcal{R}^* e^{i\mathcal{H}t}\hat{S_i^{\alpha_i}} e^{-i\mathcal{H}t}\mathcal{R}|\psi\rangle\right). \tag{4.11}$$

To compute one single term from the sum in Eq. 4.11, we generate a random state $|\psi\rangle$ and define $|\theta\rangle = \mathcal{R}|\psi\rangle$. Afterwards, we propagate the two states simultaneously in time with the time evolution operator $e^{-i\mathcal{H}t}$. At the instant of time when we desire to compute the value of that term, we compute $|\theta'(0)\rangle = \hat{S_i^{\alpha_i}}|\theta(t)\rangle$ and $|\psi'(0)\rangle = \hat{S_i^{\alpha_i}}|\psi(t)\rangle$. Subsequently, we propagate each of $|\theta'\rangle$ and $|\psi'\rangle$ backward in time for an interval of time equal to the current time instant and the value of that term would be $0.5 - 2\ Re\langle\psi'(-t)|\mathcal{R}^*|\theta'(-t)\rangle$.

We show in Fig. 4.9 $\chi(t)$ computed for the same Hamiltonians of Fig. 4.7 for systems consisting of 18 spins. One difference between the calculations is that we have restricted the rotations directions to be along the z-direction. This figure confirms the findings of Fig. 4.7 that the quantities defined so far are more sensitive to the dimensionality of the system rather than the integrability.

Next, we consider evaluating $\chi(t)$ for XXZ spin chains with spin quantum number $> \frac{1}{2}$. Note that in this case, we can not use Eq. 4.11 since $\hat{S}^2$ is not proportional to a unity operator, therefore, we should use $\chi(t)$ as defined in Eq. 4.10. The results are illustrated in Fig. 4.10 for different values of S. We make several observations from this figure. First, we notice again that the level at which $\chi(t)$ saturates depends exclusively on the number of spins in the system. That in mind, we recognize from Fig. 4.10 that a system with $S = 1$ faithfully represents all higher S, and there is no systematic tendency towards an exponential growth in $\chi(t)$ as S is increased. We notice again, as in Fig. 4.8, the clear distinction between $S = 1/2$ and larger S.

In Fig. 4.11-b, we plot $\chi(t)$ for two nonintegrable systems of spin 1/2 and 3/2, where we see the same distinction between the two cases. Therefore, we

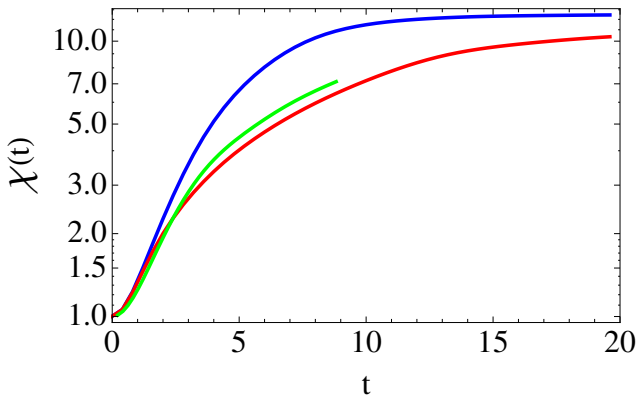

Figure 4.9: $\chi(t)$ computed for a 2D XXZ lattice consisting of 6×3 spins (blue), a 1D XXZ system composed of 18 spins (red) and a nonintegrable 1D XYZ system consisting of 15 spins with next nearest neighbor interaction (green). The Hamiltonian parameters are the same for figure 4.7.

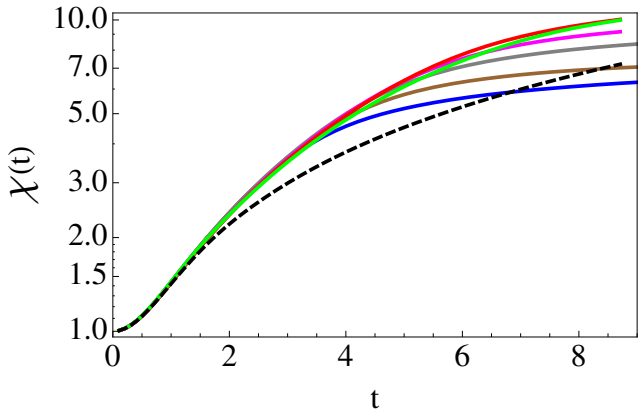

Figure 4.10: $\chi(t)$ computed for XXZ spin chains consisting of 5 spins 5 (blue), 6 spins 3 (brown), 7 spins 5/2 (gray), 8 spins 2 (magenta), 9 spins 3/2 (red), 11 spins 1 (green). The dashed line represents a spin 1/2 system consisting of 18 spins. The coupling coefficients of the Hamiltonian are scaled by $\frac{1}{\sqrt{S(S+1)}}$, where S is the quantum spin number.

conclude that this distinction is not related to the breaking of the integrability. This situation reminds us of the investigations of Gade and Lowe of the free induction decay of spin lattices of different spin quantum numbers S [134]. It was found that the free induction decay (FID) exhibits a change between $S = 1/2$ and $S = 1$, and no change as S is further increased.

Further investigation of $\chi(t)$ for other types of systems confirms that it is not related to Lyapunov sensitivity in the classical limit. In Fig. 4.11-a, we plot $\chi(t)$ for different 1D and 2D spin systems of different quantum spin numbers. The

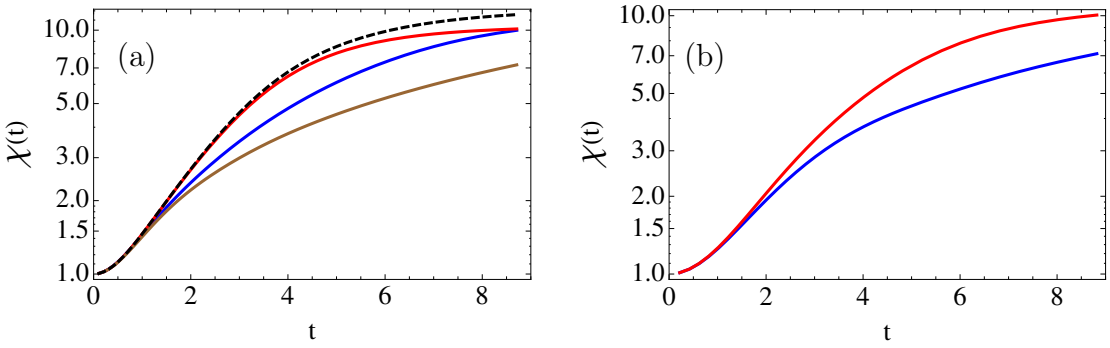

Figure 4.11: **(a)** $\chi(t)$ computed for a 1D lattice consisting of 18 spins 1/2 (brown), 1D lattice consisting of 11 spins 1 (blue), 2D lattice consisting of 3×3 spins 1 (red), and 2D lattice consisting of 3×3 spins 3/2 (dashed), all with XXZ Hamiltonians. The coupling coefficients are chosen such that the 1D and 2D systems have the same maximum Lyapunov exponent in the classical limit. **(b)** $\chi(t)$ computed for a 1D lattice consisting of 15 spins 1/2 (blue) and a 1D lattice consisting of 8 spins 3/2 (red) both with an anisotropic Heisenberg Hamiltonian with coupling coefficients $J_x = \frac{1.0}{\sqrt{14.0}}, Jy = \frac{2.0}{\sqrt{14.0}}, Jz = \frac{-3.0}{\sqrt{14.0}}$ and next nearest neighbor coupling with strength 30% of the nearest neighbor coupling. The figures confirm two things: (i) The distinction in the behavior of $\chi(t)$ between the spin 1/2 and higher spin systems and between systems of different dimensionality. (ii) This distinction is probably not related to the breaking of integrability.

coupling coefficients of the 2D system are scaled such that in the classical limit it yields the same value of the maximum Lyapunov exponent as the 1D systems. We notice again that $\chi(t)$ exhibits distinct behaviors for the systems with different dimensions.

The distinction between spin 1/2 and higher spin systems in the quantities defined in this section is very interesting. The explanation of this distinction is not clear to us. We saw already that it is not generally associated with the breaking of integrability neither with the Lyapunov exponent in the classical limit. If both $\chi(t)$ and $\wp(t)$ are not related to the Lyapunov instability in the classical limit, then which property controls their behavior? Can we define a new quantum quantity that do represent the Lyapunov instability in the classical limit? While the first question is left open, we attempt to answer the second question in the following section.

4.3 Sensitivity of Loschmidt echoes to small perturbations

In this section we set out to investigate any possible signature of exponential sensitivity in macroscopic observables of quantum systems. The intuition behind this investigation is that macroscopic variables of quantum systems should have properties similar to classical macroscopic observables. Therefore, we first investigate how to detect chaotic behavior from a measurable macroscopic behavior in spin echo experiments performed on fictitious classical spin systems. In other words, we wish to judge whether a macroscopic system is chaotic or not without having access to the coordinates of its individual microscopic degrees of freedom, but only to macroscopic quantities like total magnetization. We require that such a scheme can be implemented in a manner applicable to spin echo experiments, so that we can do the same test on macroscopic quantum systems.

The stimulating factor that has encouraged us to look into this direction is the overwhelming similarity between the long time behavior of classical and quantum spin lattices [12, 135]. The main finding of this section is that despite this similarity, macroscopic systems of spin 1/2 do not exhibit exponential sensitivity to small perturbation [5]. Systems having spin higher than 1/2, do show tendency towards an exponential sensitivity very similar to the classical behavior [4].

4.3.1 Computing the maximum Lyapunov exponent from the behavior of macroscopic observables of classical spin systems

The standard method to compute Lyapunov exponents is to measure the rate of divergence of the distance between phase space trajectories as in Eq. 1.2. We noticed, however, that by measuring the projection of the vector $\bar{\mathbf{D}}(t)$ (defined in section 1.1.2) on the direction of some observables such as the total magnetization or even the polarization of one single spin, we can compute the value of $\lambda_{\max}$ very accurately. The explanation for this behavior is simple: Since the absolute value of $\bar{\mathbf{D}}(t)$ grows exponentially in the Lyapunov regime, its projection on some

[4] Many of the investigations of classical spin systems in this section were performed by Chahan Kropf, and reproduced here with my own simulation, see [5]. The Lyapunov exponents were computed by Astrid de Wijn.

directions in phase space grows exponentially as well. The Lyapunov regime is valid when both quantities are small with respect to the dimensions of the phase space of the system.

Consider the macroscopic variable to be the total magnetization M_x. In this case, the projection of $\bar{\mathbf{D}}(t)$ on $\bar{d}_{M_x}$, a unit vector in the direction of M_x, is equivalent to the absolute difference between M_x of two different trajectories. We illustrate in Fig. 4.12 two samples of the magnetization noises $|M_{x0}(t)|$ and $|M_{x1}(t)|$ of an XXZ classical spin system consisting of $16 \times 16 \times 16$ spins and defined by the Hamiltonian

$$\mathcal{H}_0 = \sum_{i<j}^{\mathrm{NN}} J_x S_{ix} S_{jx} + J_y S_{iy} S_{jy} + J_z S_{iz} S_{jz} \ , \tag{4.12}$$

where $(S_{ix}, S_{iy}, S_{iz}) \equiv \mathbf{S}_i$ is a normalized classical spin vector, with coupling coefficients $J_x = -0.41$, $J_y = -0.41$, $J_z = 0.82$. One of the samples is obtained from a completely random state, and the other is obtained from the same state after being slightly perturbed. The perturbation is implemented by rotating each spin around a random axis by a small angle in the range $[-10^{-4}, 10^{-4}]$. Such a small perturbation makes $\bar{\mathbf{D}}(0)$ sufficiently small so that the growth of $|\bar{\mathbf{D}}(t)|$ is controlled by $\lambda_{\max}$.

In the same figure, the difference between the two magnetization noises $|\Delta M_x(t)|$ is plotted together with an exponential function of the estimated maximum Lyapunov exponent of this system. The good agreement between the two plots already from a single noise sample indicates that this method can accurately predict the value of $\lambda_{\max}$ by averaging over a sufficiently large number of independent samples.

We show in Fig. 4.13 the result for averaging over 1000 independent samples with the same perturbation mechanism described above for the same XXZ system and an XYZ system with coupling coefficients $J_x = 0.873$, $J_y = -0.436$, $J_z = 0.218$ together with a function of the form $c\, e^{\lambda_{\max} t}$. The very accurate agreement between the three plots establishes the robustness of this method and confirms the findings in [19] that away from the integrable Ising limit, $\lambda_{\max}$ is insensitive to the coupling coefficients in lattices with nearest neighbor coupling.

In accordance with the expectation that chaotic classical systems exhibit Lyapunov instability associated with perturbations to the Hamiltonian as well as to the initial conditions [136], we verified that the same behavior can be obtained when the *test trajectory* is evolved starting from the same state, but with a slightly perturbed Hamiltonian as shown in Fig. 4.14.

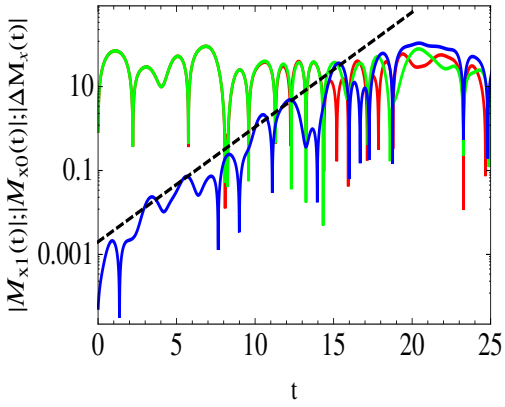

Figure 4.12: The magnetization noise $|M_{x0}(t)|$ for a classical spin system consisting of $16 \times 16 \times 16$ with coupling coefficients $J_x = -0.41$, $J_y = -0.41$, $J_z = 0.82$ (red), the magnetization noise $|M_{x1}(t)|$ for the same system started with a slightly perturbed state (green) and the absolute difference between the two signals $|\Delta M_x(t)|$ (blue). The dashed line represents $constant \times e^{\lambda_{\max} t}$ where $\lambda_{\max} = 0.63$ is the maximum Lyapunov exponent.

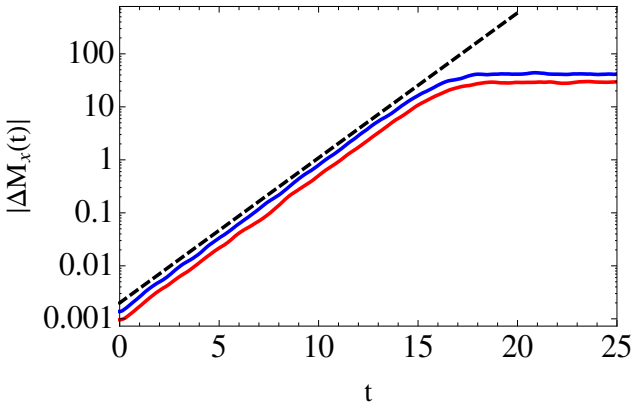

Figure 4.13: $|\Delta M_x(t)|$ averaged over 1000 independent runs for the same system in Fig. 4.12 (blue) and for classical spin system consisting of $16 \times 16 \times 16$ with anisotropic coupling constants $J_x = 0.873$, $J_y = -0.436$, $J_z = 0.218$ (red) shifted vertically for the sake of clarity. The dashed line represents the function $constant \times e^{\lambda_{\max} t}$ with $\lambda_{\max} = 0.63$.

4.3.2 Extracting the maximum Lyapunov exponent from Loschmidt echo experiments

Now, comes the question of how to apply this procedure experimentally to macroscopic systems of quantum spins to detect whether they exhibit exponential sen-

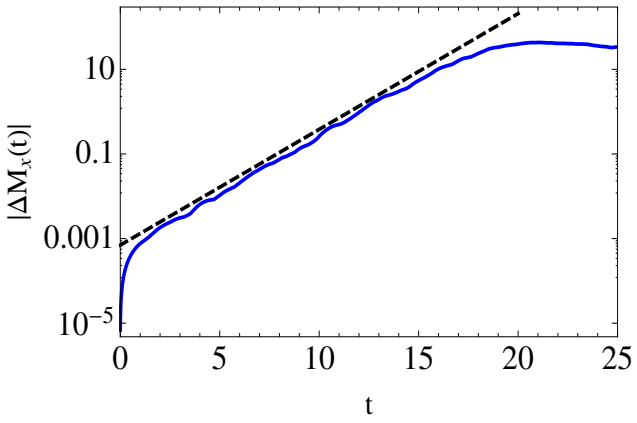

Figure 4.14: $|\Delta M_x(t)|$ averaged over 80 independent runs for a classical spin lattice consisting of $16 \times 16 \times 16$ spins with the coupling coefficients $J_x = 0.873$, $J_y = -0.436$, $J_z = 0.218$. $|\Delta M_x(t)|$ represents the difference between total magnetizations of two systems starting from the same initial condition, with the Hamiltonian of one of them perturbed by the term $\sum_k h_k S_{kz}$, where each h_k is randomly selected from the interval $[-2\ 10^{-4}, 2\ 10^{-4}]$. The dashed line represents the function $constant \times e^{\lambda_{\max} t}$ with $\lambda_{\max} = 0.63$.

sitivity or not. The answer to this question is readily provided by the magic echo technique in NMR experiments pioneered by Rhim, A. Pines and Waugh [137, 138]. In this technique, the decay of the macroscopic polarization of spins can be reversed by applying a specific sequence of radio frequency (RF) pulses that effectively reverses the sign of the Hamiltonian of the dipole-dipole interaction. The motivation to use this platform to detect chaotic behavior came from the proposal of Pastawski et. al. [139] to make use of the polarization echo in NMR experiments as a probe to the fidelity decay defined earlier in this chapter. He suggested that the inability to completely recover magnetization in polarization echo experiments is explained by an underlying chaotic dynamics.

Although the previous treatment on the exponential growth of the projection of $|\bar{\mathbf{D}}(t)|$ on $\bar{d}_{M_x}$ was carried in an equilibrium ensemble while NMR experiments normally probe nonequilibrium dynamics of macroscopic spin systems, we can still make use of NMR experiments to detect $\lambda_{\max}$ when it is nonzero. In a typical NMR experiment, the system starts with a slightly polarized state and evolves under the dipole-dipole interaction Hamiltonian for a certain time τ. At this point in time, let us call it t_0, the RF pulse sequence is applied and the sign of the Hamiltonian is effectively reversed and after the same interval τ, the value of M_x is registered. Therefore, the previous technique of detecting Lyapunov exponent

in classical spin lattices can be mapped to quantum spin lattices as the difference between the perfectly reversed signal, $M_x(t_0 - \tau)$ (the original FID signal), and the imperfectly reversed signal, $M_x(t_0 + \tau)$.

Normally, the reversal of the sign of the Hamiltonian is not perfect in realistic setups [140]. The imperfections can be modelled by two factors:
(i) A perturbation to the state of the system, by some operator $\mathcal{R}$, before the backward propagation starts.
(ii) A perturbation to the Hamiltonian during the backward time evolution, modelled by a term Δ added to the Hamiltonian.

For a classical spin system, each of these factors leads to the emergence of Lyapunov instability as illustrated above when the initial state is picked from equilibrium ensemble. In this case, the growth of $|M_x(t_0 - \tau) - M_x(t_0 + \tau)|$ as $\sim e^{\lambda_{\max}\tau}$ implies that $\langle [M_x(t_0 - \tau) - M_x(t_0 + \tau)]^2 \rangle$ grows as $\sim e^{2\lambda_{\max}\tau}$. After expanding the square bracket and noticing that in equilibrium, $\langle M_x^2(t_0 - \tau) \rangle = \langle M_x^2(t_0 + \tau) \rangle \equiv \langle M_x^2 \rangle$, we can write

$$\frac{\langle M_x(t_0 - \tau) M_x(t_0 + \tau) \rangle}{\langle M_x^2 \rangle} = 1 - Ce^{2\lambda_{\max}\tau}, \tag{4.13}$$

where C is a constant. The LHS of Eq. 4.13 represents an equilibrium correlation function that can be approximated based on the linear response theory of the previous chapter by a detectable NMR signal.

If we start with an initial state selected from the nonequilibrium density matrix $\rho_0 \cong e^{-\alpha M_x}$, where α is a small parameter, then in the linear response regime, the function

$$F(\tau) = \frac{\langle M_x \rangle_f}{\langle M_x \rangle_0}, \tag{4.14}$$

where $\langle \rangle_0$ represents an average computed with respect to the density matrix ρ_0 while $\langle \rangle_f$ represents an average computed with respect to the density matrix $\rho_f = \hat{U}_{-\mathcal{H}_0}(\tau)\, \hat{U}_R\, \hat{U}_{\mathcal{H}_0}(\tau)\, \rho_0$, is equivalent to the LHS of Eq. 4.13. In this notation, ρ_f represents the density matrix of the system after evolving forward in time by an interval τ, then perturbed by an operator $\mathcal{R}$ and propagating backward by the same interval τ. We call the quantity $1 - F(\tau)$ the imperfect Loschmidt echo and from Eq. 4.13 we expect that it grows exponentially as $Ce^{2\lambda_{\max}\tau}$ when Lyapunov instability exists.

In Fig. 4.15, we show the free induction decay (FID) of a classical spin system, where the initial state is polarized at 15% of the maximum polarization. In Fig.

4.16, we illustrate that $1 - F(\tau)$ grows exponentially by the correct Lyapunov exponent for a classical spin system consisting of $16 \times 16 \times 16$ spins.

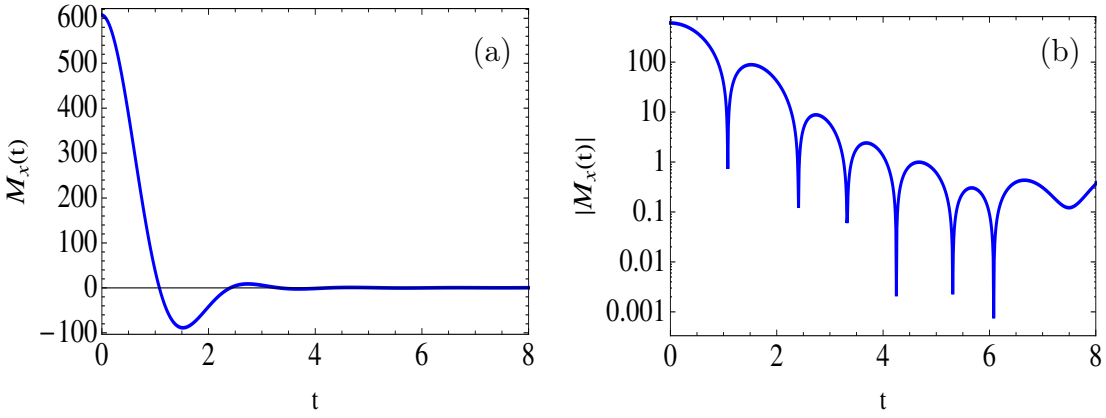

Figure 4.15: The free induction decay (FID) for a classical spin lattice consisting of $16 \times 16 \times 16$ spins with nearest neighbor interactions and coupling constants $J_x = -0.41$, $J_y = -0.41$, $J_z = 0.82$ and initial polarization 15% of maximum polarization plotted with a linear scale **(a)** and semi-log scale **(b)**.

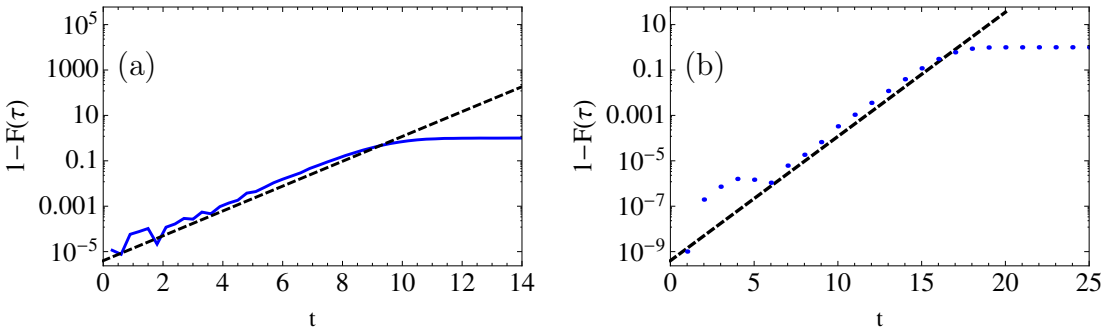

Figure 4.16: (a) Imperfect Loschmidt echo $1 - F(\tau)$ for the same classical spin lattice in Fig. 4.15 (blue) where the state is perturbed by rotating all spins slightly around a random direction by an angle in the interval $[-0.01, 0.01]$ before reversing the sign of the Hamiltonian, averaged over 10^4 runs. (b) Same as (a) except for the perturbation, which is done by perturbing the Hamiltonian during the backward evolution, by the term $\sum_k h_k S_{kz}$, where each h_k is randomly selected from the interval $[-2 \times 10^{-4}, 2 \times 10^{-4}]$. The dashed line represents *constant* $\times\, e^{2\lambda_{\max} t}$ with $\lambda_{\max} = 0.63$.

4.3.3 Are Loschmidt echoes of quantum spin systems sensitive to small perturbations?

We are now in a good position to examine the above findings applied on quantum spin systems. In general, we are interested in the regime where the effect of the perturbation on the total magnetization is small, and still causes the overlap between the perturbed and unperturbed wave functions to vanish in macroscopic systems. The quantum expression for the echo function $F(\tau)$ is

$$F(\tau) = \frac{\mathrm{Tr}\left\{e^{i\mathcal{H}_0\tau}\ \mathcal{R}^\dagger\ e^{-i\mathcal{H}_0\tau}\ M_x\ e^{i\mathcal{H}_0\tau}\ \mathcal{R}\ e^{-i\mathcal{H}_0\tau}\ M_x\right\}}{\mathrm{Tr}\left\{M_x^2\right\}}, \tag{4.15}$$

where

$$\mathcal{R} = \prod_k e^{-i\delta\theta_k S_{kz}} \approx \prod_k \left(\mathbb{1} - i\delta\theta_k S_{kz}\right). \tag{4.16}$$

We notice the apparent similarity between $1 - F(\tau)$ and individual terms in the sum in Eq. 4.11 when written as trace formulae, except for the nature of the magnetization operator involved in the trace formulae.

In the following, we give qualitative and analytical arguments that, contrary to the classical case, the effect of the perturbation $\mathcal{R}$ on the quantum system is equivalent to the effect of flipping a few spins randomly located in the lattice. In the next subsection, we will show numerically that the flipping of only one spin is already a large disturbance, even for a chaotic classical spin system, that falls outside the Lyapunov regime. Therefore, we expect not to get any exponential growth in the behavior of $1-F(\tau)$ in quantum systems subject to the perturbation $\mathcal{R}$.

Let us express the operator $\mathcal{R}$ as

$$\mathcal{R} = \sum_{m=0}^{N_s} A_m, \tag{4.17}$$

where A_m, as illustrated below, is a generic term of order $(\delta\theta_k)^m$ and consists of m spin operators S_{kz}. The effect of this term on the wavefunction is to flip the x-components of m spins, sparsely located in the lattice. This is a large perturbation that falls outside the Lyapunov regime, if it exists. If we consider only a single spin flip, the perturbation caused by this action will spread throughout the entire lattice as a "perturbation bubble" whose size grows in a power law manner rather than exponentially (the number of spins within this bubble, is proportional to $|\bar{\mathbf{D}}(t)|$ in the classical case). Therefore, the net disturbance on the total magnetization is not expected to grow exponentially.

Let the wavefunction before and after the effect of the perturbation be denoted by Ψ_- and Ψ_+ respectively, where $\Psi_+ = \mathcal{R}\Psi_-$. For all practical purposes, Ψ_- and Ψ_+ have no overlap with each other in macroscopic systems. Based on Eq. 4.17, we can write Ψ_+ as

$$\Psi_+ = \sum_\nu c_\nu \Psi_\nu, \tag{4.18}$$

where Ψ_ν is obtained from Ψ_- by flipping the x-components of a certain configuration of spins. We call the set of states $\{\Psi_\nu\}$ the perturbation basis. The above argument is valid when the main contribution to $\langle M_x \rangle_f$ comes from the "diagonal" elements $\langle \Psi_\nu | e^{-i\mathcal{H}_0\tau} M_x e^{i\mathcal{H}_0\tau} | \Psi_\nu \rangle$ while the interference components $\langle \Psi_{\nu'} | e^{-i\mathcal{H}_0\tau} M_x e^{i\mathcal{H}_0\tau} | \Psi_\nu \rangle$ do not contribute. We shall now show this explicitly.

By using the exact expression for $\mathcal{R}$, $\mathcal{R} = \prod_k [\mathbb{1}\cos(\delta\theta_k/2) - i\sigma_{kz}\sin(\delta\theta_k/2)] = \sum_{m=0}^{N_s} A_m$, we find that A_m is given by

$$\begin{aligned} A_m &= (-i)^m \sum_{\boldsymbol{\alpha}}^{L(m)} [\cos(\delta\theta_{\bar{\alpha}1}/2)\cos(\delta\theta_{\bar{\alpha}2}/2)...\cos(\delta\theta_{\bar{\alpha},N_s-m}/2)] \\ &\qquad \times [\sin(\delta\theta_{\alpha 1}/2)\sigma_{\alpha 1 z}\sin(\delta\theta_{\alpha 2}/2)\sigma_{\alpha 2 z}...\sin(\delta\theta_{\alpha m}/2)\sigma_{\alpha m z}] \\ &\approx \left(-\frac{1}{2}i\right)^m \sum_{\boldsymbol{\alpha}}^{L(m)} \exp\left\{-\frac{1}{8}\sum_p^{N_s-m} \delta\theta^2_{l_{\bar{\alpha}p}}\right\} (\delta\theta_{\alpha 1}\sigma_{\alpha 1 z}...\delta\theta_{\alpha m}\sigma_{\alpha m z}), \end{aligned} \tag{4.19}$$

which represents a sum over all the combinations of m spin operators. The number of these combinations, $L(m)$ is given by the binomial formula

$$L(m) = \frac{N_s!}{m!(N_s-m)!} \approx \frac{N_s!\; e^{-m(\ln m - 1) - (N_s-m)(\ln(N_s-m)-1)}}{2\pi\sqrt{m(N_s-m)}}. \tag{4.20}$$

In Eq. 4.19, $\boldsymbol{\alpha}$ represents a certain configuration of the spins whose indices are $\{\alpha_1, \alpha_1, ...\alpha_m\}$ while $\bar{\boldsymbol{\alpha}} = \{\bar{\alpha_1}, \bar{\alpha_2}, ...\alpha_{\bar{N_s}-m}\}$ represents the complementary set of indices. We have approximated the product of cosines by a product of Gaussian functions, since we are working in the small angle limit, $\delta\theta_k \ll 1$.

To illustrate the decomposition 4.17, we give explicit expression for $\mathcal{R}$ in the case of three spin-1/2:

$$
\begin{aligned}
\mathcal{R} \;=\; & \prod_{k=1}^{3}[\mathbb{1}\cos(\delta\theta_k/2) - i\sigma_{kz}\sin(\delta\theta_k/2)] = \\
& \underbrace{\cos(\delta\theta_1/2)\cos(\delta\theta_2/2)\cos(\delta\theta_3/2)\;\mathbb{1}}_{A_0} \\
& \underbrace{-\,i\;\left[\cos(\delta\theta_2/2)\cos(\delta\theta_3/2)\sin(\delta\theta_1/2)\;\sigma_{1z} + \cos(\delta\theta_1/2)\cos(\delta\theta_3/2)\sin(\delta\theta_2/2)\;\sigma_{2z}\right.}_{A_1} \\
& \underbrace{\left. +\;\cos(\delta\theta_1/2)\cos(\delta\theta_2/2)\sin(\delta\theta_3/2)\;\sigma_{3z}\right]}_{A_1} \\
& +(-i)^2\left[\cos(\delta\theta_3/2)\sin(\delta\theta_1/2)\;\sigma_{1z}\;\sin(\delta\theta_2/2)\;\sigma_{2z}\right. \\
& \underbrace{\left. +\cos(\delta\theta_2/2)\sin(\delta\theta_1/2)\;\sigma_{1z}\;\sin(\delta\theta_3/2)\;\sigma_{3z} + \cos(\delta\theta_1/2)\sin(\delta\theta_2/2)\;\sigma_{2z}\;\sin(\delta\theta_3/2)\;\sigma_{3z}\right]}_{A_2} \\
& + \underbrace{(-i)^3\sin(\delta\theta_1/2)\;\sigma_{1z}\;\sin(\delta\theta_2/2)\;\sigma_{2z}\;\sin(\delta\theta_3/2)\;\sigma_{3z}}_{A_3}. \qquad (4.21)
\end{aligned}
$$

A state Ψ_ν that belongs to the perturbation basis, corresponding to a certain configuration $\boldsymbol{\alpha}$ consisting of m spins, is expressed as

$$|\Psi_{\nu(m,\boldsymbol{\alpha})}\rangle = \sigma_{l_{\alpha 1}z}\sigma_{l_{\alpha 2}z}...\sigma_{l_{\alpha m}z}|\Psi_-\rangle, \qquad (4.22)$$

while its amplitude is given by

$$c_{\nu(m,\boldsymbol{\alpha})} \approx \left(-\frac{1}{2}i\right)^m \exp\left\{-\frac{1}{8}\sum_{p}^{N_s-m}\delta\theta^2_{l_{\bar{\alpha}p}}\right\}\delta\theta_{l_{\alpha 1}}\delta\theta_{l_{\alpha 2}}...\delta\theta_{l_{\alpha m}}. \qquad (4.23)$$

The average of c_ν over many perturbations is given by

$$\langle|c_{\nu(m,\boldsymbol{\alpha})}|^2\rangle \approx (\frac{1}{4})^m \exp\left\{-\frac{1}{4}\sum_{p}^{N_s-m}\langle\delta\theta^2_{l_{\bar{\alpha}p}}\rangle\right\}\langle\delta\theta^2_{l_{\alpha 1}}\rangle\langle\delta\theta^2_{l_{\alpha 2}}\rangle... = e^{-(N_s-m)\kappa}\;\kappa^m, \qquad (4.24)$$

where

$$\kappa \equiv \frac{1}{4}\langle\delta\theta^2_k\rangle. \qquad (4.25)$$

This quantity does not depend on the particular configuration $\boldsymbol{\alpha}$, but only on the number of spins m. The overall probability to find the x-components of m spins flipped is given by

$$P_m \approx L(m)e^{-(N_s-m)\kappa}\kappa^m \approx \frac{N_s!\;e^{m(\ln\kappa - \ln m + 1) - (N_s-m)[\ln(N_s-m)-1+\kappa]}}{2\pi\sqrt{m(N_s-m)}}. \qquad (4.26)$$

We now show that this quantity is dominated by the probabilities corresponding to a small number m, i.e., only a small fraction of spins is effectively flipped.

Neglecting the pre-exponential factor and maximising the power of the exponent with respect to m, we find that the exponential factor is maximum when m is given by

$$m = \frac{\kappa e^{\kappa} N_s}{\kappa e^{\kappa} + 1} \approx \kappa N_s. \tag{4.27}$$

That means that, on average, only a fraction $\approx \frac{1}{4}\langle \delta\theta_k^2 \rangle$ of the whole lattice is flipped, in the S_x-basis, by the action of the perturbation operator. In other words, the probability of each spin to be flipped is given by $\frac{1}{4}\langle \delta\theta_k^2 \rangle$, an expected result.

Coming back to the main quantity of interest,

$$\langle M_x \rangle_f = \sum_{\nu,\nu'} c^*_{\nu'} c_{\nu} \langle \Psi_{\nu'} | e^{-i\mathcal{H}_0\tau}\ M_x\ e^{i\mathcal{H}_0\tau} | \Psi_{\nu} \rangle,$$

we show that it is primarily controlled by the diagonal elements, $\langle \Psi_{\nu} | e^{-i\mathcal{H}_0\tau}\ M_x\ e^{i\mathcal{H}_0\tau} | \Psi_{\nu} \rangle$, while the off-diagonal elements are orders of magnitude smaller. To begin with, the average of $c^*_{\nu'} c_{\nu}$ will vanish for $\nu' \neq \nu$ when the angles of rotations $\{\delta\theta_k\}$ are uncorrelated. Moreover, if we represent $|\Psi_{\nu}\rangle$ and $|\Psi_{\nu'}\rangle$ as

$$\Psi_{\nu} = \sigma_{q_1 z}\sigma_{q_2 z}...\sigma_{p_1 z}\sigma_{p_2 z}...|\Psi_{-}\rangle, \tag{4.28}$$

$$\Psi_{\nu'} = \sigma_{q_1 z}\sigma_{q_2 z}...\sigma_{p'_1 z}\sigma_{p'_2 z}...|\Psi_{-}\rangle, \tag{4.29}$$

where $\{\sigma_{q_1 z}, \sigma_{q_2 z}, ...\}$ is the set of common spin indices between $|\Psi_{\nu}\rangle$ and $|\Psi_{\nu'}\rangle$ while $\{\sigma_{p_1 z}, \sigma_{p_2 z}, ...\}$ and $\{\sigma_{p'_1 z}, \sigma_{p'_2 z}, ...\}$ are the distinct indices, we see that at $\tau = 0$, $\langle \Psi_{\nu'} |\ M_x\ | \Psi_{\nu} \rangle$ will be vanishingly small due to the unpaired spin operators in the last two sets. We illustrate in Fig. 4.17 a typical evolution for $\langle \Psi_{\nu'}(t) |\ M_x\ | \Psi_{\nu}(t) \rangle$ and $\langle \Psi_{\nu}(t) |\ M_x\ | \Psi_{\nu}(t) \rangle$ for a spin 1/2 chain consisting of 24 spins where each of the states $|\Psi_{\nu}\rangle$ and $|\Psi_{\nu'}\rangle$ is obtained from $|\Psi_{-}\rangle$ by applying a set of three operators $\{\sigma_{iz}\}$ located randomly in the lattice.

To recapitulate, we have demonstrated that the effect of applying the perturbation operator defined in Eq. 4.16 is equivalent to the action of flipping the x-components of a small number of spins that represents a fraction $\approx \frac{1}{4}\langle \delta\theta_k^2 \rangle$ of the entire lattice. There are several configurations of spins $\boldsymbol{\alpha}$ having the same order of magnitude in their contributions which renders $|\Psi_{+}\rangle$ a superposition of all of them. Nevertheless, the net effect on $\langle M_x \rangle_f$ is dominated by the average contribution of each of them, and their interferences are negligible.

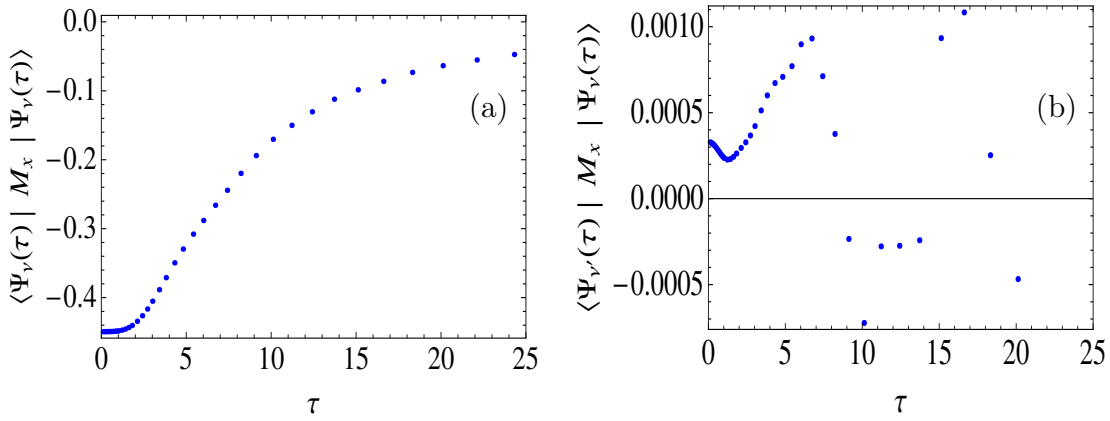

Figure 4.17: This figure demonstrates the order of magnitude of the terms $\langle\Psi_\nu(t)|\ M_x\ |\Psi_\nu(t)\rangle$ and $\langle\Psi_{\nu'}(t)|\ M_x\ |\Psi_\nu(t)\rangle$ for a spin chain consisting of 24 spins 1/2. $|\Psi_\nu\rangle$ is obtained from $|\Psi_-\rangle$ by applying a sequence of three randomly selected σ_{iz} operators.

4.3.4 Numerical simulations of Loschmidt echoes in quantum spin systems

We now present the numerical simulations that show that support the previous arguments. We take as a nonintegrable quantum spin-1/2 system a 2D lattice consisting of 5×5 spins with XXZ coupling coefficients $J_x = -0.47$, $J_y = -0.47$, $J_z = 0.94$. This Hamiltonian corresponds to the Hamiltonian considered for classical spins after rescaling the coupling coefficients to account for the fact that $|\boldsymbol{S}|^2 = \frac{3}{4}$ for a quantum spin while $|\boldsymbol{S}|^2 = 1$ for a classical spin. We illustrate in Fig. 4.18 the FID for this lattice, where the initial state is selected from the ensemble $\rho_0 = e^{-\beta\mathcal{H}}$ with $\beta = 0.1$ corresponding to an initial polarization $= 5\%$ of the maximum polarization. Numerically, we generate an infinite temperature state $|\psi_0\rangle$, and obtain $|\Psi_0\rangle$ by applying the operator$e^{-\beta/2\mathcal{H}}$ on $|\psi_0\rangle$. The last step is implemented through an imaginary time version of the Runge-Kutta routine described in chapter 3.

We compute the quantity $1 - F(\tau)$, where $F(\tau)$ is defined in 4.14, for the same system by the same procedure described for the classical spin system. Namely, we propagate the nonequilibrium state $|\Psi_0\rangle$ for a certain time τ, perturb the state, propagate it backwards for τ and compute $\langle M_x\rangle_f$. However, now we can take advantage of the quantum typicality results [4, 141] of the previous chapter and the better averaging properties associated with the quantum simulation and

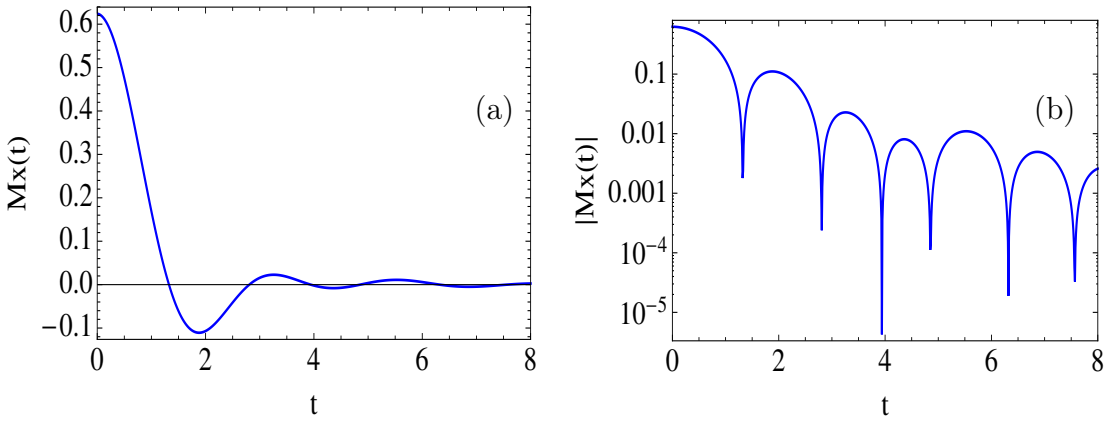

Figure 4.18: The free induction decay FID computed for a 5×5 quantum spin 1/2 lattice, with XXZ coupling coefficients $J_x = -0.47$, $J_y = -0.47$, $J_z = 0.94$, plotted on a linear scale (a) and a semi-log scale (b). The initial state is selected from the ensemble $\rho_0 = e^{-\beta \mathcal{H}}$ with $\beta = 0.1$ corresponding to an initial polarization = 5% of the maximum polarization.

compute $1 - F(\tau)$ based on one single initial state, $|\Psi_0\rangle$.

In Fig. 4.19, we show $1 - F(\tau)$ computed for the quantum system where the perturbation is implemented by rotating each spin around the z-axis by an angle randomly selected from the interval $[-0.01, 0.01]$. We observe that $1 - F(\tau)$ exhibits no exponential growth in the limited range available by the finite system size. We test the validity of the previous argument stating that the effect of such a perturbation is equivalent to the flipping of a small fraction of spins by computing $1 - F(\tau)$ when the perturbation $\mathcal{R}$ causes a single spin flip (rotating a single spin by an angle π around the z-axis). As depicted in Fig. 4.19, $1 - F(\tau)$ computed by this perturbation is very close to the original echo function, and does not exhibit exponential growth either. While the overlap between the perturbed and unperturbed evolution is large in the first case, it is almost zero in the second case. This implies that the vanishing of the overlap between $|\Psi_0\rangle$ and $|\Psi_f\rangle$ in a macroscopic system should not change this result.

To illustrate that one spin flip is a large perturbation that falls outside the Lyapunov regime, we compute the echo function for a classical system, when the perturbation is caused by completely flipping one spin ($s_x \to -s_x, s_y \to -s_y$ and $s_z \to -s_z$). The results shown for an average over 8×10^4 runs is very similar to the quantum case and confirm our previous explanation. To exclude the possibility that the absence of exponential sensitivity in a 5×5 lattice is a finite size effect,

we compute $1 - F(\tau)$ and $\langle [M_x(t_0 - \tau) - M_x(t_0 + \tau)]^2 \rangle$ for a classical system of the same size when the perturbation is caused by a small rotation of each spin and the initial state is selected from an equilibrium ensemble in the second case. We show the results in Fig. 4.20 and they clearly exhibit an exponential growth of $\sim e^{1.6\lambda_{\max}\tau}$.

The second possibility for the disturbance of the echo by a perturbation to the Hamiltonian, instead of perturbing the state itself, is illustrated in Fig. 4.19-b. We disturb the echo function of the spin 1/2 system by adding a disordered field in the z direction of the form $\sum_k h_k S_{kz}$, where each h_k is randomly selected from the interval $[0.05, -0.05]$. The growth of $1 - F(\tau)$ does not show any exponential dependence in this case either. We note, however, that the overall shape of the echo function is determined by the overlap between $|\Psi_0\rangle$ and $|\Psi_f\rangle$, which is initially very close to one, and then decays to zero due to the perturbed dynamics. A perturbed Hamiltonian continuously perturbs the state during the reversed evolution and therefore makes the discussion on the absence of exponential sensitivity due to the first type of perturbation relevant to this case too.

For the sake of completeness, we illustrate that a single spin flip is a large perturbation even for a macroscopic system. We show in Fig. 4.21 $\langle [M_x(t_0 - \tau) - M_x(t_0 + \tau)]^2 \rangle$ computed for classical 100×100 spin lattice when the echo is disturbed by a complete flip of a single spin and by flipping only the x-component of a single spin separately. The exponential sensitivity is absent in both cases.

Since the validity of our argument for the absence of exponential sensitivity to perturbations in spin 1/2 systems relies on the fact that the projection of individual spins 1/2 can not be perturbed by a small value, then we should expect to see first signs of exponential growth in spin $> 1/2$ systems. This is indeed the case, as we show in Fig. 4.22, where $1 - F(\tau)$ is computed for a classical spin chain consisting of 1000 spins and a quantum spin-12 chain consisting of 5 spins. We see clearly that a small region of exponential growth appears in the quantum case that has the same slope on the logarithmic scale as the classical case.

Finally, we note that the Loschmidt echo produced by a spin-flip perturbation in a classical spin system can be used to probe whether the perturbation caused by the flipping of a classical spin propagates through the lattice in a ballistic or diffusive way. Since $1 - F(\tau)$ measures the square of the phase space distance between the perturbed and unperturbed systems $\langle |\bar{\mathbf{D}}(\tau)| \rangle^2$, it can be used as an indicator for the size of the perturbation bubble. If the perturbation propagates

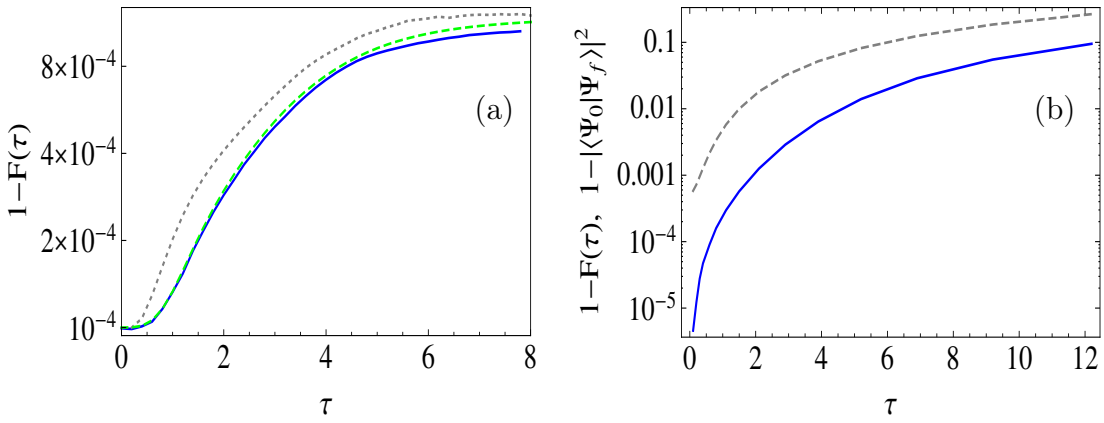

Figure 4.19: (a) Solid line: Imperfect Loschmidt echo $1 - F(\tau)$ for a 5×5 quantum spin 1/2 lattice, with XXZ coupling coefficients $J_x = -0.47$, $J_y = -0.47$, $J_z = 0.94$. The perturbation is implemented by rotating each spin around the z-axis by an angle selected randomly from the interval $[-\pi/100, \pi/100]$. Dashed line: Imperfect Loschmidt echo $1 - F(\tau)$ for the same quantum spin lattice, with the perturbation implemented by rotating a single spin around the z-axis by an angle$=\pi$. Dotted line: imperfect Loschmidt echo $1 - F(\tau)$ for a 5×5 classical spin lattice, with the perturbation implemented by rotating a single spin around the z-axis by an angle equal to π. (b) Solid line: Imperfect Loschmidt echo $1 - F(\tau)$ for a 5×5 quantum spin 1/2 lattice, with XXZ coupling coefficients $J_x = -0.47$, $J_y = -0.47$, $J_z = 0.94$. The echo is disturbed by adding a perturbation to the Hamiltonian of the form $\sum_k h_k S_{kz}$, where each h_k is randomly selected from the interval $[0.05, -0.05]$. The dashed line represents $1 - |\langle \Psi_f | \Psi_0 \rangle|^2$.

through the lattice diffusively, the size of the bubble, and consequently $\langle |\bar{\mathbf{D}}(\tau)| \rangle$ grows as a power law $\sim (\sqrt{\tau})^d$ where d is the number of dimensions. On the other hand, if the perturbation spreads ballistically, $\langle |\bar{\mathbf{D}}(\tau)| \rangle$ grows as $\sim \tau^d$. We show in Fig. 4.23 the echo function for 1D, 2D and 3D classical spin systems perturbed with a single spin flip on a log-log scale fitted with the functions $c_1\tau^{1.22}$, $c_2\tau^{2.8}$ and $c_3\tau^{3.8}$ respectively. The deviations from the prediction of the diffusion model are 20%, 40% and 26% respectively. We present further investigations of the spin diffusion problem in classical and quantum spin lattices in the next chapter.

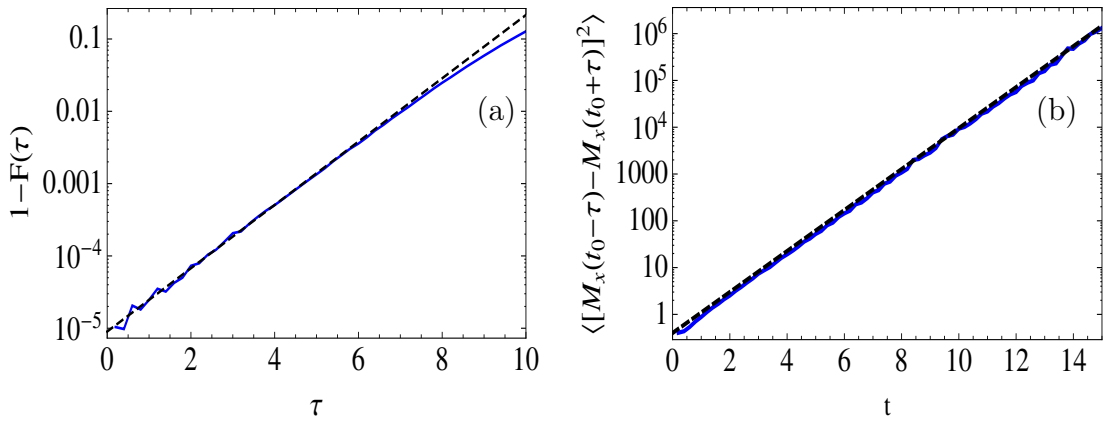

Figure 4.20: (a) Imperfect Loschmidt echo $1 - F(\tau)$ for a 5×5 classical spin lattice averaged over 32×10^6 time evolutions. The echo is disturbed by rotating each spin around the z-axis by an angle selected randomly from the interval $[-\pi/100, \pi/100]$. (b) $\langle[M_x(t_0 - \tau) - M_x(t_0 + \tau)]^2\rangle$ for a 5×5 classical lattice (dashed black) where the state is perturbed by rotating all spins slightly around a random direction before reversing the sign of the Hamiltonian. In Fig. (b), the initial state is selected from an equilibrium ensemble. The dashed lines in the two plots represent the exponential function $\sim e^{1.6\lambda_{\max}\tau}$.

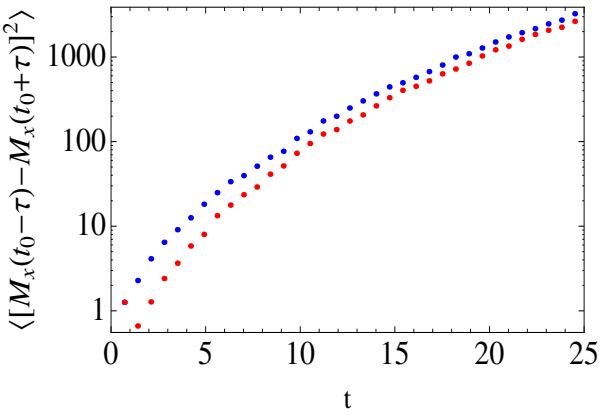

Figure 4.21: $\langle[M_x(t_0 - \tau) - M_x(t_0 + \tau)]^2\rangle$ computed for a 2D classical spin lattice consisting of 100×100 spins. The the disturbance to the echo is caused by completely flipping a single spin (blue) or by flipping only the x-component of a single spin (red). In both cases, the growth of $\langle[M_x(t_0 - \tau) - M_x(t_0 + \tau)]^2\rangle$ is not exponential. The initial state is selected from an equilibrium ensemble.

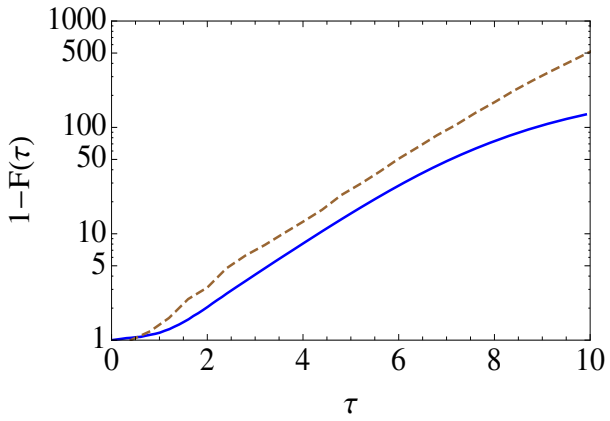

Figure 4.22: The imperfect Loschmidt echo $1-F(\tau)$ for a classical spin chain consisting of 1000 spins (dashed brown) averaged over 36×10^4 runs compared with $1-F(\tau)$ for a quantum spin chain consisting of 5 spins-12, with XXZ coupling coefficients (blue).

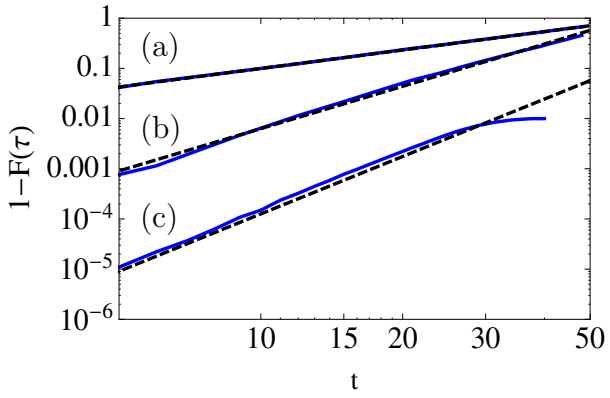

Figure 4.23: The imperfect Loschmidt echo $1-F(\tau)$ for a classical spin chain consisting of 100 spins (a), 2D classical spin lattice consisting of 100×100 spins (b) and a 3D classical spin cube consisting of $40 \times 40 \times 40$ spins (c) plotted on a log-log scale, all with XXZ coupling coefficients. The echo is disturbed at the moment of time reversal by the flipping of a single spin. The three plots are fitted with power law fits, with exponents 1.22, 2.8 and 3.8 respectively.

4.4 Summary

In this chapter, we tried to look for any signature of exponential sensitivity in nonintegrable quantum spin systems. We started with the most popular measure to quantify sensitivity to perturbations in quantum systems, namely quantum fidelity. The negative results obtained in quantum spin 1/2 systems indicated that either exponential sensitivity does not exist at all in these systems, or that we have to look for another measure. We introduced several elementary attempts that aimed to conceive analogous measures to Lyapunov exponents in quantum spin systems. However, all of them failed to discriminate between integrable and nonintegrable quantum spin systems. We noticed, however, a clear distinction between spin 1/2 and higher spin systems.

The following endeavor sought to find out the footprint of exponential sensitivity in the behavior of macroscopic observables. We developed a technique [5] that could extract the value of the maximum Lyapunov exponent from imperfect Loschmidt echo experiments performed on classical spin systems. Once again, the same technique applied to quantum spin 1/2 systems implied the absence of exponential sensitivity. The analytical argument justifying this behavior hinges on the fact that a perturbation to a spin 1/2 will flip it completely. The effect of the perturbation will propagate to the neighboring spins in a power law time-dependent fashion. Therefore, the total effect on the magnetization does not grow exponentially. For spins higher than 1/2, on the other hand, there is room for small growth of the perturbation effect on the total magnetization locally in each spin. Therefore, we can observe initial signs of exponential sensitivity in terms of the Loschmidt echo in those systems.

Anything you can do in classical physics, we can do better in quantum physics.

Daniel Kleppner

5

Spin diffusion and free induction decay in solids

This chapter is devoted to two separate issues in the physics of quantum spin systems: Spin diffusion and free induction decay in solids.

Spin diffusion is a scheme of spin transport which has practical implications in information technologies [142]. An extensive number of studies have been pursued to prove or disprove the existence of this regime (the spin diffusion hypothesis) in quantum spin systems. In section 5.1, we apply the methods developed in chapter 3 to shed more light on this problem and compare the results of our simulation with several results obtained in the past using other approaches.

One of these approaches used classical spin simulation to gain insights into the analogous quantum problem. The idea of using classical spin dynamics to study the properties of quantum spin systems is not new. In fact, it was exploited by Fisher [143] to compute correlation functions and thermodynamic properties for quantum spin 1/2 chains by simulating the classical limit of the quantum spin chain. In the context of spin transport, Waugh et. al. in [135, 144] used classical spin simulation to study spin diffusion in NMR systems. Recently, Steinigeweg compared the spin transport at infinite temperature of classical and quantum spins

and found also close similarity between the two regimes [145]. In section 5.2, we use the same method to compute the free induction decay in solids and compare our results with experimental data.

5.1 Spin diffusion in quantum and classical spin systems

Consider a quantum spin system, where the projection of the total magnetization in a certain direction is conserved, and the initial state of the system is such that one spin is completely polarized while the rest is not polarized. How should the polarization of that spin spread throughout the entire system? Will the spin polarization be transported to the neighboring spins in a diffusive manner or a ballistic manner? The answer to this question was first proposed in the context of nuclear magnetic resonance (NMR) [146–148] to explain the long decay time of the magnetization (T_2) by assuming that the energy (and magnetization) is spatially transported in solids via a diffusion process.

The concept of diffusion in solids is a phenomenological concept to describe the transport of conserved quantities in a hydrodynamic way following a diffusion equation similar to the heat diffusion equation. Consider a quantum spin system having the conserved quantity,

$$S_q^\mu = \frac{1}{\sqrt{N}} \sum_m \exp(iqm) S_m^\mu, \tag{5.1}$$

where S_m^μ represents the μ^{th} component of the spin operator at lattice site m. According to the spin diffusion hypothesis, the intermediate structure factor $C^\mu(q,t)$, defined as

$$C^\mu(q,t) = \left\langle S_q^\mu(t)\, S_{-q}^\mu(0) \right\rangle, \tag{5.2}$$

follows the diffusion equation

$$\frac{\partial C^\mu(q,t)}{\partial t} \approx -Dq^2 C^\mu(q,t), \tag{5.3}$$

at very small values of momentum q, long times and high temperatures. D is the diffusion coefficient. This relation is applicable only for $t > 0$, since at $t = 0$, $C^\mu(q,t)$ exhibits a time-reversible behavior, and can not be described by such an irreversible process. The solution of 5.3 yields $C^\mu(q,t) \sim e^{-Dq^2 t}$. Noticing that $C^\mu(q,t)$ is the spatial Fourier transform of the correlation function $C_n(t) =$

$\langle S^{\mu}_{m}(t)\, S^{\mu}_{m+n}(0)\rangle$, i.e., $C^{\mu}(q,t) = \sum_n \exp(-iqn)\,\langle S^{\mu}_{m}(t)\, S^{\mu}_{m+n}(0)\rangle$, we find that a diffusive behavior in 1D leads to $C_n(t) \sim t^{-1/2} e^{-\frac{n^2}{4Dt}}$ [149]. In general, a diffusive behavior in d dimensions leads to a decay of the long-time behavior of the auto-correlation function $\langle S^{\mu}_{m}(t)\, S^{\mu}_{m}(0)\rangle$ that behaves as $t^{-d/2}$ [150].

It is generally accepted that the spin-1/2 XXZ Heisenberg model,

$$H_{XXZ} = 2J \sum_{i=1}^{N} \{S^x_i S^x_{i+1} + S^y_i S^y_{i+1} + \Delta S^z_i S^z_{i+1}\}, \tag{5.4}$$

exhibits diffusive behavior for $\Delta > 1$ and ballistic behavior for $\Delta < 1$ (see [145, 151] and references therein). In this section, we treat both the anisotropic Heisenberg model ($\Delta > 1$) and the more subtle isotropic model ($\Delta = 1$). We let $\hbar = 1$ in the rest of this section.

5.1.1 Spin diffusion in isotropic Heisenberg systems

In this part, we will be concerned with testing the spin diffusion hypothesis at infinite temperature for isotropic Heisenberg 1D systems with periodic boundary conditions. In this case, we can show that $C^{\mu}(q,t)$ is equivalent to $I^{\mu}_{q}(t)$ defined in (3.47). Due to the isotropy of the system, we drop the μ index from the intermediate structure factor in this section and denote it simply as $I_q(t)$. We will use the quantum dynamical typicality approach developed in chapter 3 to compute $I_q(t)$ for Heisenberg spin 1/2 chains for different values of q and test directly whether $I_q(t)$ obeys a diffusion equation, i.e., test the validity of $I_q(t) \sim e^{-Dq^2 t}$.

We have computed $I_q(t)$ based on Eq. 3.48 for Heisenberg chains consisting of 17, 20, 24, 26 and 29 spin 1/2 with nearest neighbor interaction Hamiltonian, $\mathcal{H} = J \sum_i \mathbf{S_i} \cdot \mathbf{S_{i+1}}$. The value of q is taken to be the smallest q allowed for the system, i.e., $q = \frac{2\pi}{N_s}$, where N_s is the number of spins. The normalized intermediate structure factor, $I_q(t)/I_q(0)$ is shown in plots (a) in Fig. 5.1. We notice that after the initial reversible behavior, a region of extended exponential decay appears, before an oscillatory behavior dominates at large times.

To test whether the exponential parts of plots (a) in Fig. 5.1 obey the diffusion behavior, $I_q(t) \sim e^{-Dq^2 t}$, we plot the same data with the horizontal axis scaled as $\alpha\, q^2 t$ in (b). If $I_q(t)$ was described as $e^{-Dq^2 t}$, the extended exponential regions for different values of q would be parallel to each other. It is not so obvious whether this is the case or not in (b). In part (c) of Fig. 5.1, we plot the same data with the time scaled as $q^2\,(1 + 0.1\ln|q|)\, t\ln(t)$. The motivation behind this choice

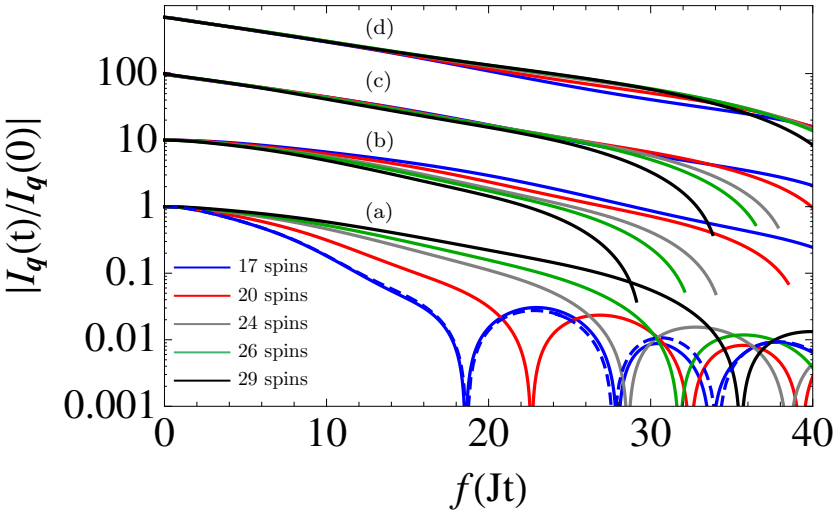

Figure 5.1: Intermediate structure factor $I_q(t)$ computed at infinite temperature using (3.48) for Heisenberg chains consisting of 17 (blue), 20 (Red), 24(Gray), 26 (Green) and 29 (Black) spins with nearest neighbor interaction Hamiltonian $\mathcal{H} = J\sum_i \mathbf{S_i}\cdot\mathbf{S_{i+1}}$. $q = 2\pi/N_s$, where N_s is the number of spins. The dashed plot is computed by exact diagonalization for comparison. The horizontal axis is Jt for (a), $\alpha q^2 t$ for (b), $\beta q^2\,(1+0.1\ln(q))\,t\,\ln(t)$ for (c) and $\gamma q^2 t^{1.5}$ for (d) where α, β and γ are arbitrary scaling parameters. The vertical axes for the upper three sets of plots are arbitrarily scaled. Plots (b) test spin diffusion hypothesis. Plots (c) test scaling reported for classical spins in [153].

comes from the work of Bonfin and Reiter [152] who found from numerical experiments on the classical Heisenberg spin system that $I_q(t)$ fits equally well with $\exp\left(-0.543\ q^{2.12}t\ \ln(t)\right)$ and $\exp\left(-0.537\ q^2(1+0.1\ \ln|q|)\ t\ \ln(t)\right)$. The remarkable coincidence between the four plots in (c), before the oscillatory regime dominates, gives more credit to the proposal that $I_q(t)$ is described by $e^{-D_0 q^2(1+0.1\ln|q|)t\ln(t)}$ as in the classical regime.

Before we go on and describe plots (d) in Fig. 5.1, we discuss the issue of anomalous diffusion in quantum spin systems. It is clear that the function $\exp\left(-D_0\ q^2(1+0.1\ \ln|q|)\ t\ \ln(t)\right)$ can not be the result of a normal diffusion process. Let us first emphasize that what controls whether the spin transport is ballistic or diffusive is the behavior of the current-current correlation function, $\langle\mathcal{J}^\mu(t)\mathcal{J}^\mu\rangle$, where $\mathcal{J}^\mu$ is the spin current operator corresponding to the magnetization in the μ-direction. The current operator for $\mathcal{J}^z$ is $\sum_n j_n^z$ where J_n^z is determined from the continuity equation $\frac{\partial S_n^z}{\partial t} + \nabla J_n^z = 0$. The time derivative

term in this equation is computed using the Heisenberg equation of motion and the gradient term is represented in a discretized form. After solving for j_n^z, we find $j_n^z = S_n^x S_{n+1}^y - S_n^y S_{n+1}^x$. According to the Green-Kubo formula [91, 154], the diffusion coefficient D is the integral of $\langle \mathcal{J}^\mu(t)\mathcal{J}^\mu \rangle$,

$$D = \int_0^\infty dt \langle \mathcal{J}^\mu(t)\mathcal{J}^\mu \rangle. \tag{5.5}$$

A finite value of D occurs when $\langle \mathcal{J}^\mu(t)\mathcal{J}^\mu \rangle$ decays sufficiently fast. For example, in the context of the Brownian motion problem, it is assumed that the velocity auto-correlation function of the Brownian particle decays very fast, with respect to the time scale of the large-scale motion of the Brownian particle, giving rise to the diffusive behavior. This turns out not to be the case in the spin transport problem. It was found in the isotropic quantum Heisenberg system, by means of tDMRG calculation in [151], that the diffusion coefficient anomalously diverges with the square root of the number of spins, $D \propto \sqrt{n}$. However, from our numerical simulation, we found that $I_q(t)$ is the same for the same q and different system sizes. Therefore, we suggest that the divergence of the diffusion coefficient observed in [151] is an effective behavior due to the slow decay of the spin current correlation function $\langle \mathcal{J}(t)\mathcal{J} \rangle$ at long times. If the current correlation function decays as $1/\sqrt{t}$, then, according to Green-Kubo formula, D will diverge with the square root of time. In this case, when the Green-Kubo integral is restricted to times proportional to the system size, the effective proportionality $D \propto \sqrt{n}$ will emerge [155, 156].

This line of thought gives rise to the possibility that $I_q(t)$ can also be described by $\exp\left(-D_0\, q^2 t\sqrt{t}\right)$. We show in Fig. 5.1 (d), the scaling corresponding to this behavior where horizontal axis is $\gamma q^2 t\sqrt{t}$. The good agreement between different values of q supports this prediction as well. On the other hand, the better agreement between $I_q(t)$ and $\exp\left(-D_0\, q^2\, (1 + 0.1\, \ln|q|)\, t\, \ln(t)\right)$ in Fig. 5.1 (c) implies that $\langle \mathcal{J}(t)\mathcal{J} \rangle$ decays as $1/t$.

In what follows, we investigate the two possibilities for the behavior of the current autocorrelation function using direct calculation of $\langle \mathcal{J}(t)\mathcal{J} \rangle$ based on the Onsager regression relation (ORR) expressed by Eq. 3.29. In Fig. 5.2, we show $\langle \mathcal{J}(t)\mathcal{J} \rangle$ computed for a 28-spin system. The correlation function is computed using ORR with an initial state $e^{-\beta\mathcal{J}/2}|\varphi(0)\rangle$, where $|\varphi(0)\rangle$ is an infinite temperature state and $\beta = 0.25$[1]. Although $I_q(t)$ fits very well with both $e^{-0.35\, q^2\, t\sqrt{t}}$

[1]Compare the computation of $\langle \mathcal{J}(t)\mathcal{J} \rangle$ with the computation based on tDMRG (Fig. 3-a in [150]).

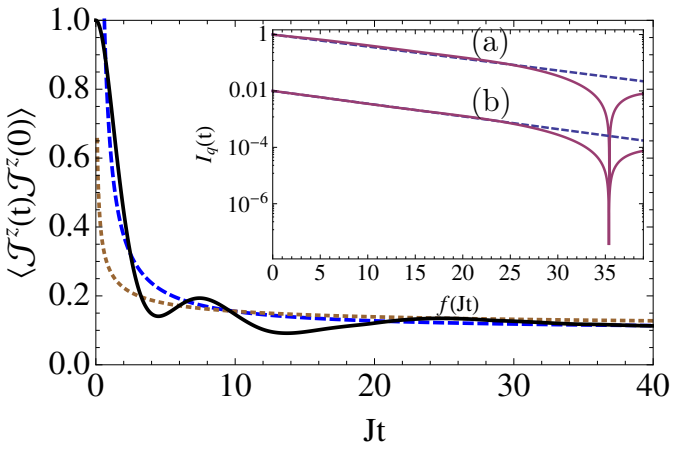

Figure 5.2: Main frame: The spin current autocorrelation function $\langle \mathcal{J}(t)\mathcal{J}\rangle$ (solid) computed using ORR (3.28) for a Heisenberg chain composed of 28 spins fitted with with $0.105 + 0.55/t$ (dashed) and $0.065 + 0.35/\sqrt{t}$ (dotted). Inset: The intermediate structure factor $\langle I_q\,(t)\rangle$ computed using ORR (3.28) for the same system (solid) fitted with $e^{-0.55\ q^2\ t\ \ln(t)}$ (dashed) and plotted versus $\alpha t\ \ln(t)$ (a). Plot (b) represents the same quantity plotted versus $\beta t^{1.5}$ and fitted with $e^{-0.35\ q^2\ t\sqrt{t}}$ (dashed). α and β are arbitrary constants chosen such that the first zero crossing in the two plots coincide with its location in the Jt axis. The vertical axis in (a) and (b) is arbitrarily scaled.

and $e^{-0.55\ q^2\ t\ \ln(t)}$ as shown in the inset of Fig. 5.2 , we show in the main frame of Fig. 5.2 that $\langle \mathcal{J}(t)\mathcal{J}\rangle$ fits better with $0.105 + 0.55/t$ than $0.065 + 0.35/\sqrt{t}$, which gives more merit to the second form.

The results in Figs. 5.1 and 5.2 confirm the recent investigations suggesting that the isotropic Heisenberg model is an intermediate case between ballistic and diffusive behaviors [150, 157, 158]. A non-vanishing Drude weight, defined by the limiting value of the spin current correlation function at very long times, gives rise to an infinite DC conductivity and consequently indicates ballistic transport. This is the case we have here as shown in Fig. 5.2. However, a non-vanishing Drude weight is a not a necessary condition for ballistic transport. The diffusion coefficient would also diverge with time if the current correlation function decays to zero sufficiently slow. Our findings are consistent with the investigations in [150], where the the transport in the Heisenberg chain with periodic boundary conditions is attributed to the existence of both ballistic and diffusive channels simultaneously.

Another way to deal with the spin diffusion problem is to compute the spatial correlation function $C_n\,(t)$. A diffusive behavior in 1D makes $C_0\,(t)$ behaves

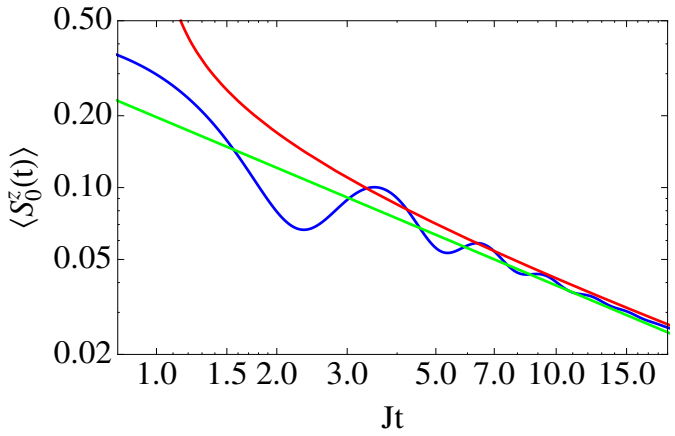

Figure 5.3: The relaxation of $\langle S_0^z(t)\rangle$ for a initial state with one spin completely polarized. The systems is an isotropic Heisenberg chain consisting of 25 spin 1/2 with periodic boundary conditions (blue) compared with $At^{-0.705}$ (green) and $B\left(t\,\ln(t)\right)^{-0.5}$ (red), where A and B are fitting parameters. The horizontal and vertical axes are in logarithmic scales. In the linear response regime, $\langle S_0^z(t)\rangle$ gives a good representation of the spatial correlation function $\langle S_m^z\left(t\right)S_m^z\left(0\right)\rangle$ according to Onsager regression hypothesis

as $t^{-0.5}$. An earlier study by Fabricius and McCoy [159] on infinite temperature correlation functions of 16-spin chains suggested the absence of spin diffusion in anisotropic Heisenberg systems with small anisotropy. For the particular case of isotropic Heisenberg system, they found that $C_0\left(t\right)\sim t^{-0.705}$. However, the agreement between $I_q(t)$ and $\exp\left(-D_0\;q^2\;t\;\ln(t)\right)$ suggests that $C_0\left(t\right)\sim\left[t\;\ln(t)\right]^{-0.5}$. We illustrate in Fig.5.3 that the two predictions are very close to each other at large times.

The infinite temperature spin-spin correlation function for a 25-spin chain is computed in the spirit of Onsager relaxation relation by letting one spin be initially completely polarized in a completely unpolarized environment and following the evolution of its polarization as it decays with time. During its relaxation to zero polarization (equilibrium state), the polarization of the spin will pass through the linear response regime where its polarization is proportional to $C_0(t)\equiv\langle S_0^z(t)S_0^z(0)\rangle$. In Fig. 5.3, the long time tail in the linear response regime is compared with $At^{-0.705}$ and $B\left[t\;\ln(t)\right]^{-0.5}$ and shows a good agreement with the two functions. The true behavior of $C_0(t)$ in the thermodynamic and long time limits can not however be described by both functions since they diverge at very large times.

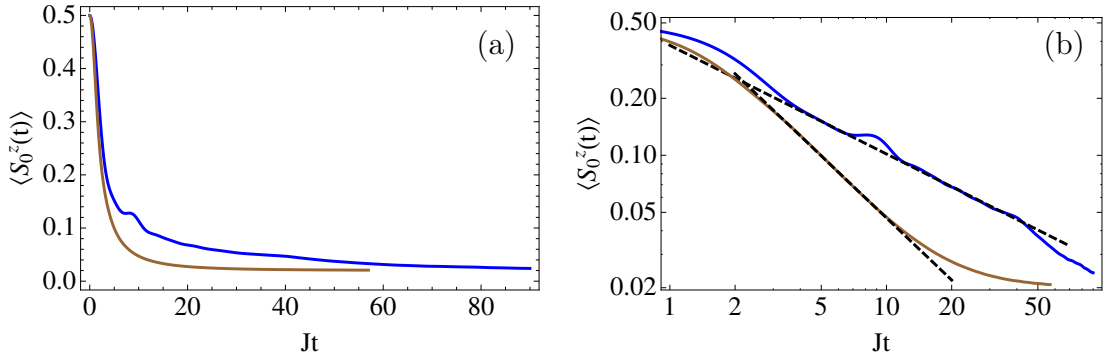

Figure 5.4: (a) The relaxation of $\langle S_0^z(t)\rangle$ for an initial state with one spin completely polarized. The systems is an anisotropic Heisenberg system with coupling coefficients $J_x = -0.5, J_y = -0.5$ and $J_z = 1$ for a 1D system consisting of 25 spins (blue) and 2D lattice consisting of 5×5 spins (brown). (b) Same as (a) in logarithmic scale. The dashed black lines represent the fitting functions $c_1\ t^{-0.574}$ in the 1D case and $c_2\ t^{-1.09}$ in the 2D case.

5.1.2 Spin diffusion in anisotropic Heisenberg systems

After treating the controversial case of the isotropic Heisenberg system, let us now consider the more established case of anisotropic Heisenberg, namely the XXZ model. We have computed $C_0(t) \equiv \langle S_0^z(t) S_0^z(0)\rangle$ for 1D and 2D XXZ systems consisting of 25×1 and 5×5 spins respectively with coupling coefficients $J_x = -0.5, J_y = -0.5$ and $J_z = 1$. We used the same relaxation technique in Fig. 5.3 by letting one spin be completely polarized, while the rest of the system is unpolarized. We show in Fig. 5.4 the relaxation of $\langle S_0^z(t)\rangle$ for both systems in linear and logarithmic scales. This figure confirms the existence of power law decay regions in both cases. We show the fitting of these regions with the functions $c_1\ t^{-0.574}$ in the 1D case and $c_2\ t^{-1.09}$ in the 2D case. These functions are close to the predictions of the spin diffusion hypothesis.

Let us now consider an interesting issue in the dynamical process of the relaxation of $\langle S_0^z(t)\rangle$. In order to study the diffusion of a single spin polarization (say the zeroth spin S_0), we have initialized that spin to a completely polarized state. That means that its state is initially disentangled with rest of the system (the environment). As the polarization of that spin diffuses away to the surrounding, the spin gets more and more entangled with its environment. How does the growth of the entanglement between the spin and its environment correlate with the diffusion of the spin polarization?

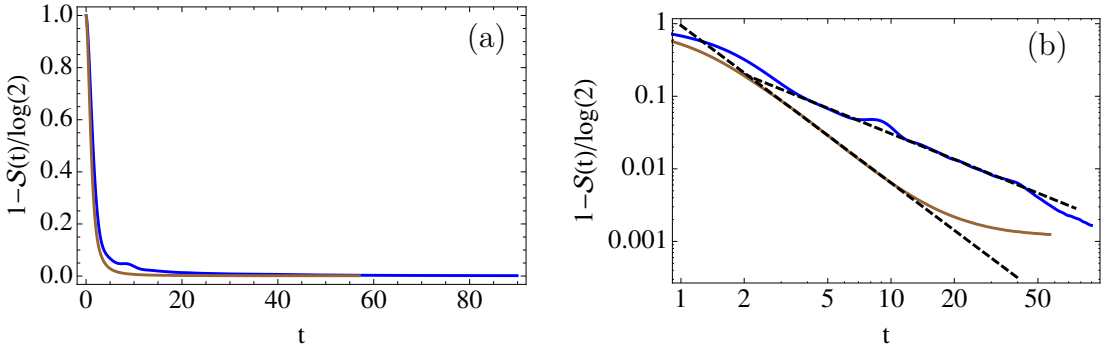

Figure 5.5: (a) $1-\mathcal{S}(t)/log(2)$, where $\mathcal{S}$ is the entanglement entropy of ρ_0, the reduced density matrix of the 0^{th} spin as its polarization diffuses to its environment. The two plots represent the 1D (blue) ad 2D (brown) systems in Fig. 5.4. (b) Same as (a) in logarithmic scale. The dashed black lines represent the fitting functions $c_1\ t^{-1.17}$ in the 1D case and $c_2\ t^{-2.17}$ in the 2D case.

We have investigated this issue by computing the von Neumann entanglement entropy ($\mathcal{S} \equiv -\text{Tr}\{\rho_0 \ln\rho_0\}$) of the reduced density matrix ρ_0 of the zeroth spin as a function of time. Initially, the 0^{th} spin is in a pure state, therefore the entropy of ρ_0 is zero. At equilibrium, the spin is fully entangled and $\mathcal{S} = \log(2)$. In Fig. 5.5, we plot $1-\mathcal{S}(t)/\log(2)$ for the two cases in Fig. 5.4 on logarithmic and linear scales. We notice that the function $1-\mathcal{S}(t)/\log(2)$ decays as a power law with almost twice the exponent of the power law decay of $\langle S_0^z(t)S_0^z(0)\rangle$.

Of course, entanglement entropy is not a conserved quantity so as to speak about a model of its transport. However, the correlation between the diffusion of the spin polarization (a measurable quantity) and the development of its entanglement entropy implies that $\mathcal{S}$ can be probed in experiments by measuring a physical quantity.

5.1.3 Spin diffusion in classical spin systems

For the sake of completeness, we include the results of investigating the spin diffusion hypothesis in classical spin lattices. We consider XXZ models, with coupling coefficients $J_x = -0.5, J_y = -0.5$ and $J_z = 1$ as in the previous part for quantum spin 1/2 systems. The correlation function $\langle S_0^z(t)S_0^z(0)\rangle$ is computed in the spirit of Onsager regression relation, as before, by letting one spin be completely polarized, and monitoring the relaxation of $\langle S_0^z(t)\rangle$ in the linear response regime (near equilibrium). We include the results in 1D, 2D and 3D in Fig. 5.6 in logarithmic

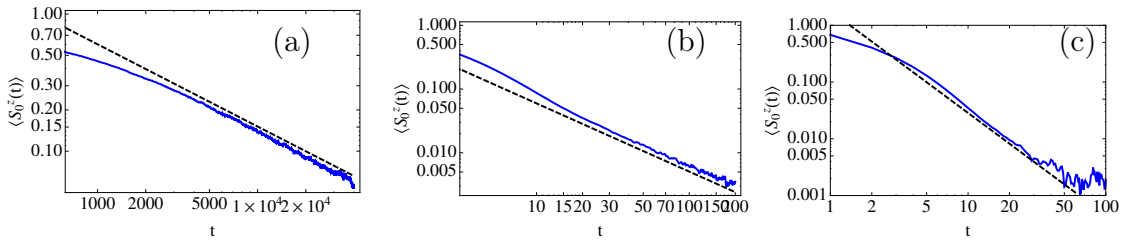

Figure 5.6: The relaxation of $\langle S_0^z(t)\rangle$ from a completely polarized state for a classical anisotropic Heisenberg system with coupling coefficients $J_x = -0.5, J_y = -0.5$ and $J_z = 1$ for a 1D system consisting of 1000 spins (a), 2D lattice consisting of 30×30 spins (b) and 3D lattice consisting of $10 \times 10 \times 10$ spins (c). The dashed black line represent the fitting functions $c_1\ t^{-0.6}$ in the 1D case, $c_2\ t^{-1.07}$ in the 2D case, and $c_3\ t^{-1.8}$ in the 3D case. The results shown in the three figures correspond to averaging over 2×10^6, 4×10^6 and 1.2×10^6 runs respectively.

scales, fitted with polynomial functions of the form $c\, t^{-\nu}$. The values of ν obtained from the fitting polynomials differ from the predictions of the diffusion hypothesis by at most 20%.

5.2 Free induction decay in solids

In this section, we consider one of the most outstanding problems in solid state physics, namely computing the free induction decay (FID) in solids. The problem is to find a controllable method to compute the FID signal for a given material, in terms of the its microscopic parameters. The setting of an FID experiment, is similar to the relaxation scheme described in chapter 3 in the context of Onsager regression relation. A typical experiment can be abstracted as follows: A lattice of interacting magnetic dipoles is polarized by an external magnetic field, and then the field is switched off, letting the lattice relax to equilibrium under the effect of mutual interactions between the dipoles, which do not conserve the total polarization.

The problem lies in computing the shape of the magnetization signal as it decays to zero, approaching the equilibrium state. This signal is proportional to the RF signal detected in the RF coils in NMR experiments. In frequency domain, this signal controls the shape of the NMR spectral lines which is used to identify unknown materials or tissues in magnetic resonance experiments.

Computing this signal accurately is a long standing problem in solid state physics due to its non-perturbative nature (absence of small parameter that can

be used in perturbation expansions to obtain approximate solutions). Moreover, the time scale for the decay of the FID signal is the fastest time scale of the problem, namely the time scale of the dipole-dipole interaction [13]. Therefore this problem can not be dealt with like a Markovian problem, where a separation of time scales between a slow process and a fast environment exists.

In NMR problems, the lattice of interacting dipoles is initially in thermal equilibrium in an external magnetic field in the z-direction at a certain temperature. This temperature determines the value of the overall polarization of the lattice in the z-direction. The Hamiltonian of this lattice is given by

$$H = \sum_{m<n} \frac{1}{r_{mn}^3} \left\{ \boldsymbol{\mu}_m . \boldsymbol{\mu}_n - 3 \frac{(\boldsymbol{\mu}_n . \mathbf{r}_{mn})(\boldsymbol{\mu}_m . \mathbf{r}_{mn})}{r_{mn}^2} \right\}, \tag{5.6}$$

where the magnetic dipole moment $\boldsymbol{\mu}$ is given in terms of the gyromagnetic ratio γ and the spin operator $\mathbf{S}$ by $\boldsymbol{\mu} = \gamma\hbar\mathbf{S}$ and $\mathbf{r}_{mn}$ is the distance vector connecting the lattice locations m and n.

In order to excite the lattice in the nonequilibrium state, that has a nonzero magnetic polarization in x-direction, a $\pi/2$ RF pulse is applied that effectively rotates the polarization vector by 90 degrees around the y-axis. Under the mutual interactions between the nuclear dipoles, the transverse polarization in the xy-plane decays to its equilibrium value during a time interval known as spin-spin relaxation time (T_2).

It is more convenient to work in the rotating reference frame, defined by the frequency of the exciting RF field. In this frame, the effective Hamiltonian is a truncated version of 5.6, that reads [160]

$$\mathcal{H} = \sum_{m<n} J_{mn} \left[S_m^z S_n^z - \frac{1}{2} \left(S_m^x S_n^x + S_m^y S_n^y \right) \right], \tag{5.7}$$

where

$$J_{mn} = \frac{\gamma^2 \hbar^2 \left(1 - 3\cos^2 \theta_{mn}\right)}{|\mathbf{r}_m - \mathbf{r}_n|^3}. \tag{5.8}$$

The angle θ_{mn} represents the angle between the lattice vector $\mathbf{r}_{mn}$ and the external magnetic field $\mathbf{B}_0$. According to the linear response theorem, the relaxation function (FID signal) of the transverse magnetization is determined by the infinite temperature correlation function

$$C(t) = \frac{\mathrm{Tr}\{e^{\frac{i}{\hbar}\mathcal{H}t} \sum_n S_n^x \, e^{\frac{-i}{\hbar}\mathcal{H}t} \sum_m S_m^x\}}{\mathrm{Tr}\{[\sum_n S_n^x]^2\}}. \tag{5.9}$$

Computing $C(t)$ for realistic materials is by no means a trivial task. Many approximations for $C(t)$ over the past half century have been devised. We have performed many numerical experiments with small quantum spin clusters that aimed to reproduce $C(t)$ for real materials using the techniques of chapter 3. The main limitation comes from the finite number of quantum spin 1/2 (in the order of 20) that can be included in the simulation. The long-range nature of the interaction makes the memory required to store the Hamiltonian matrix much larger than the nearest neighbor interaction Hamiltonian for the same system size. In the next part, we report on another method that uses classical spins to compute the correlation function $C(t)$ for a fundamentally quantum problem!

5.2.1 Computing free induction decay using classical spin simulation

We have seen in the previous section how the magnetization is transported in XXZ classical and quantum spin lattices following similar diffusion laws. This observation was exploited to study spin and energy diffusion in quantum spin systems based on computational studies on classical spin lattices by J. S. Waugh and his collaborators [135, 144]. They have shown, using coherent state representation of quantum spins, that at high temperature and large number of interacting spins, the quantum spin diffusion problem reduces to the classical limit [135]. Additionally, the long time behavior of classical spin lattices was found to exhibit decaying oscillatory behavior as in the long time behavior of the free induction decay in solids [12]. An early attempt to derive a theoretical formula for the FID for a quantum system of a general spin S found also similar behavior for all $S > 1/2$ and in some cases for $S > 1$ [134]. We have also observed in chapter 4 that the imperfect Loschmidt echo for spin S much bigger than 1/2 behave similarly to classical spin systems. Do not all these observations indicate that the long standing challenge of controllably computing FID can be solved at least for $S > 1/2$ using simulations of large clusters of spins in the classical limit?

C. Tang and J. S. Waugh have already performed classical spin simulations in the early 90s with the modest computing resources available at that time to reconstruct the FID signal for simple cubic lattices [144]. They have also shown that the moments of FID functions for quantum and classical spin lattices are close to each other. In this part, we exploit the tremendous leap in computational power over the last two decades to do a more extensive simulation of classical

spin lattices to investigate how far this method can reproduce accurately the free induction decay signal for real materials having both $S = 1/2$ and $S > 1/2$.

We start by CaF_2, the benchmark material for NMR experiments. In this material, the Flourine nuclei have spin quantum number 1/2, gyromagnetic ratio $\gamma = 25166.2$ $s^{-1}G^{-1}$, abundance 100% and are arranged in a simple cubic lattice, with lattice constant $a_0 = 2.72$ Å. We show in Fig. 5.7, the experimental data for FID corresponding to directions [100], [110] and [111] of the external magnetic field compared with the results of computing $C(t)$ for a classical spin lattice. The experimental data for [100] and [111] directions are taken from [161] while the data for [110] direction is taken from [162]. The Hamiltonian of the classical spin lattice is defined by 5.7 with the spin operators replaced by classical spin vectors and with imposed periodic boundary conditions. The coupling coefficients for the classical Hamiltonian J_{mn} equal the coupling coefficients for the quantum Hamiltonian 5.8 divided by $\hbar$. In all cases, we considered a lattice consisting of $11 \times 11 \times 11$ sites.

To compute $C(t)$, we initialize the system at an infinite temperature state, evolve it for a time T, and evaluate

$$C(t) = \int_0^{T-t} M_x(\tau) M_x(\tau + t) d\tau \tag{5.10}$$

where $M_x = \sum_n S_n^x$. This procedure is repeated over many random initial states, and the resultant $C(t)$ is averaged over all of them and properly normalized such that $C(0) = 1$. The results shown in Fig. 5.7 correspond to $T = 200J^{-1}$, time step $dt = 0.1J^{-1}$ where $J = \gamma\hbar/a_0^3$ and averaging over 32×10^4 independent runs in [100] and [110] directions and 64×10^4 in [111] direction. The time axis for the classical simulation has to be rescaled by a factor $\sqrt{S(S+1)}$ to account for the quantum spin number $S = 1/2$.

The good agreement between $C(t)$ computed for classical spin lattices and the experimental data in the three directions for three orders of magnitude indicates the validity and robustness of this method to reproduce FID. The ability to compute the quantum correlation function from measuring the classical spin noise may give some credit to Eq. 3.31 in the context of the modified regression relation introduced in chapter 3. The two separate findings imply that in the macroscopic limit, the classical and quantum spin noise at equilibrium behave similarly and both can be employed to reproduce the quantum correlation function at infinite temperature.

In fact, the method followed in [144] to reproduce $C(t)$ depends on the Onsager regression relation described in chapter 3, applied on classical spin systems.

An initial state corresponding to a nonequilibrium ensemble is selected, and the evolution of $M_x(t)$ in the linear response regime averaged over many runs was compared with the FID. Let us repeat this procedure for the CaF_2 with external magnetic field in [110] direction. We have selected an initial state from an ensemble corresponding to $M_x(0) \approx 0.35\%$ of the maximum polarization, and computed the average evolution of $M_x(t)$ over 64×10^5 runs. We see in Fig. 5.8 that the relaxation of $M_x(t)$ reproduces accurately $C(t)$ for the first two peaks, but the level of statistical noise is higher than using (5.10), although the same computing resources were used in both calculations. Therefore, we conclude that Eq. 5.10 is a more efficient method to compute FID with classical spin systems. [2]

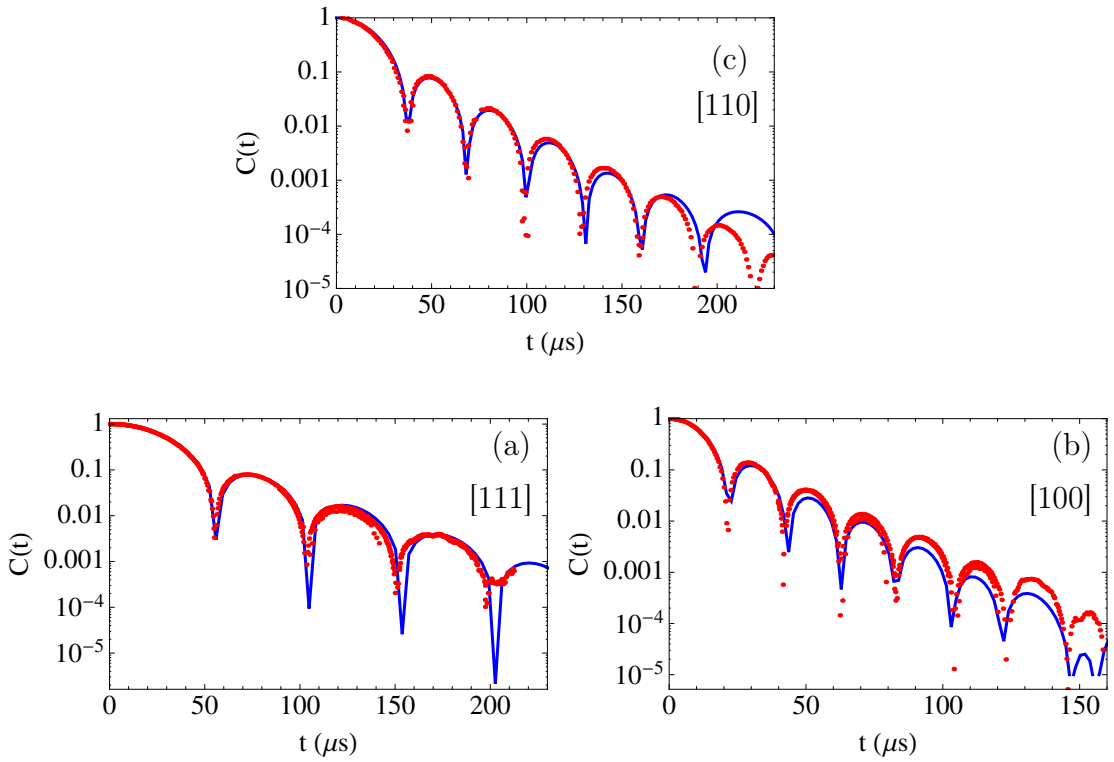

Figure 5.7: The correlation function $C(t)$ (blue) computed as described by (5.10) for the total magnetization of classical spin lattices consisting of $11 \times 11 \times 11$ spins at infinite temperature compared with the experimental FID for CaF_2 (red). The external magnetic field is directed towards the lattice directions [100], [111] and [110]. The numerical simulations are obtained by averaging over 32×10^4 independent runs.

[2] From Fig. 5.8, we see that the linear response theory and Onsager regression relation are applicable to nonintegrable (chaotic) systems, whose underlying dynamics is nonlinear. This falsifies the objections of van Kampen [163] against the validity of ORR in nonlinear systems.

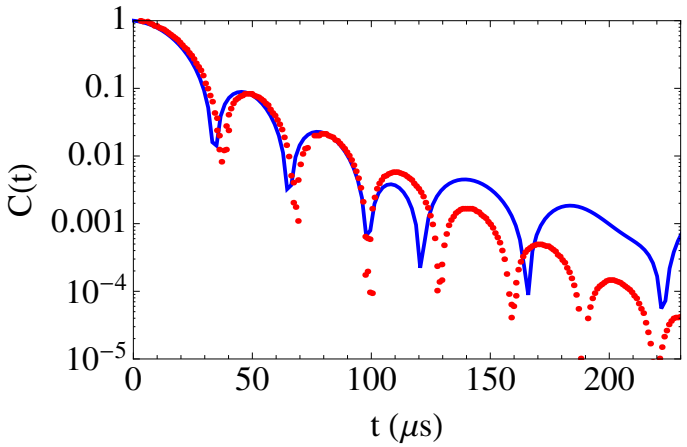

Figure 5.8: The experimental FID for CaF_2 (red) compared with the correlation function computed by the relaxation function of $M_x(t)$ from a nonequilibrium state corresponding to a total polarization $\approx 0.35\%$ of the maximum polarization towards equilibrium averaged over 64×10^5 runs (blue). The external magnetic field is directed towards the lattice directions [110].

Finally, we consider the free induction decay of Aluminium powder based on the experimental data of Jürgen Haase group in Leipzig [164], and investigate whether the present method can reproduce accurately $C(t)$. The nuclei of Aluminium are characterized by quantum spin number $S = 5/2$ and gyromagnetic ratio $\gamma = 6972.04\ s^{-1}G^{-1}$ and are arranged in an FCC lattice structure with lattice constant $a_0 = 4.0495$ Å. The result of computing $C(t)$ using classical spin simulation, with the same simulation parameters for the CaF_2 is depicted in Fig. 5.9. The only difference in this case, is that we let the magnetic field have a random direction for each run, to simulate a powder material. We notice that the frequency of the oscillations in the FID signal is accurately reproduced by the classical spin correlation function, while the exponential decay constant is not. We tried to increase the size of the lattice, but that did not help improve the matching of the decay constant.

Based on the findings of this chapter and chapter 3, we propose the following hybrid classical-quantum algorithm to obtain more accurate results for the FID problem. The algorithm is based on replacing the core of the classical spin lattice by a lattice of quantum spins, interacting fully quantum mechanically. The mutual effects of the quantum core and the outside classical lattice can be modeled in a

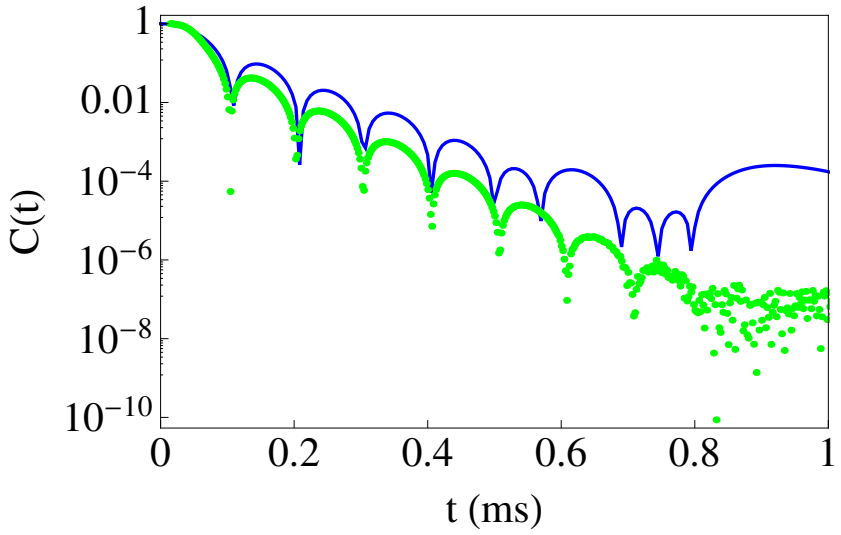

Figure 5.9: The correlation function $C(t)$ (blue) computed as described by (5.10) for the total magnetization of classical spin lattices consisting of $11 \times 11 \times 11$ spins at infinite temperature averaged over 64×10^4 random orientations of the magnetic field compared with the experimental FID [164] for metallic Aluminium powder measured at 11.7 Tesla (green).

mean field manner, by adding a dynamic classical field at the location of each spin that sums up the effects of all spins of the other type. This algorithm is likely to be severely limited by the memory requirements which will limit the number of spins that can be used in the quantum core.

Each problem that I solved became a rule, which served afterwards to solve other problems.

Rene Descartes

6

Summary and outlook

Motivated by the long-anticipated relevance of chaos to the foundations of statistical mechanics, we attempted to identify chaos in many-body systems through a universal approach valid for both macroscopic many-body classical and quantum system. The essence of this approach is to quantify the randomness of macroscopic observables instead of dealing with phase space techniques (e.g., Lyapunov exponents and Kolmogorov-Sinai entropy). However, the finite-length limitation of the measured data in realistic situations was not easy to overcome. We exploited our observation of the qualitative differences in the frequency domain between chaotic and integrable time series to introduce new measures that demand very accurately measured data, but not necessarily very long time series. We believe that other information-theoretic approaches (e.g., [165, 166]) can still give useful insights into the problem of quantum chaos.

In chapter 2, we emphasized the overall differences in the shapes of the power spectra between several chaotic and integrable systems. We anticipate that detailed analysis of the fluctuations of the power spectrum may lead to new indicators of chaos in both classical and quantum systems.

Most of the work presented in the rest of the dissertation dealt with various aspects of quantum and classical spin systems. In chapter 3, we combined several

results and concepts in the dynamics of many-particle quantum systems. These results are:
(i) Quantum dynamical typicality: The expectation value of an observable computed from a single pure state is a good representative of the dynamics of that observable averaged over the whole Hilbert space.
(ii) Onsager regression relation: The relaxation of an observable to equilibrium is similar to the quantum correlation function at equilibrium.
(iii) Runge Kutta algorithm: Simple fourth-order expansion of the Taylor series of the time evolution operator is an effective method to solve the time-dependent Schrödinger equation.

We used these results to arrive at two new important results:
(i) The modified regression relation: The relaxation of an observable computed from a single pure state approaches the correlation of the equilibrium fluctuations at equilibrium in the thermodynamic limit.
(ii) Infinite temperature correlation functions can be efficiently computed by propagating single pure states.

We were mainly concerned in chapter 3 with the infinite temperature limit of the fluctuation-dissipation theorem. It would be interesting, though, in future studies to study the more general case of finite temperature and verify equation 3.10 numerically in various types of systems.

The crucial property of chaos in classical systems is hypersensitivity to initial conditions and perturbations. Hypersensitivity to perturbations was already shown to exist in several quantum systems [127, 167]. On the other hand, several studies, e.g., [168], maintained the absence of sensitivity of quantum dynamics, in particular in bounded systems, to initial conditions and perturbations. In chapter 4, we set out to investigate this issue in quantum spin systems, equipped with the toolbox of numerical techniques developed in chapter 3. We developed several intrinsically quantum quantities that had the potential to discriminate integrable from nonintegrable quantum spin lattices. None of these quantities fulfilled this aim. We noticed, however, that these quantities behave differently for spin $1/2$ systems and systems with higher spin quantum number.

The most experimentally relevant approach to detect chaos in chapter 4 is based on the concept of Loschmidt echo. We showed that the maximum Lyapunov exponent can be extracted from this type of experiments performed on classical spin lattices. Nonintegrable quantum spin $1/2$ systems, however, were shown to

exhibit no sensitive dependence on small perturbations based on this approach.

This result may sound a bit surprising given some of the signatures of chaos existing in the free induction decay of real spin 1/2 materials (e.g., exponential decay of correlation functions and exponential tails in NMR spectral lines). It implies that nonintegrable quantum systems can exhibit these features without possessing the essential property of chaos, which is exponential sensitivity to small perturbations.

In chapter 5, we concentrated on two issues. The first is the spin transport in Heisenberg spin chains. We showed that the anomalous diffusion in the isotropic Heisenberg chain can be attributed to the signatures of ballistic transport in that model. On the other hand, we verified the predictions of the spin diffusion hypothesis in the anisotropic case for both classical and quantum spin systems.

In the second part of this chapter, we showed the close agreement between the free induction decay of real materials and the simulation results from the analogous classical spin lattices (at least as far as the frequency of the oscillatory behavior of the free induction decay is concerned). This agreement is a good news for NMR community, where a controllable method to predict FID and the spectral line shapes accurately is still missing.

Finally, we believe that the methods developed in this work can be used to analyze many interesting phenomena in the physics of many-body systems that have not been discussed here. These topics include:

- Decoherence, and how it is affected by the integrability of the system, the bath, or both of them.
- Quenched dynamics and periodically driven spin systems [169].
- Localization in disordered spin systems.
- Spin glasses.
- Thermalization and the role of integrability in the approach to equilibrium.
- Quantum phase transitions.

Bibliography

[1] T. Elsayed, B. Hess, and B. V. Fine, "Detecting microscopic chaos in a time series of a macroscopic observable," *arXiv preprint arXiv:1105.4575*, 2011. 2, 8, 18, 25, 33, 39, 40, 43

[2] M. Toda, "Waves in nonlinear lattice," *Progress of Theoretical Physics Supplement*, vol. 45, no. Supplement 1, pp. 174–200, 1970. 2, 44, 49

[3] S. W. Morgan, B. V. Fine, and B. Saam, "Universal long-time behavior of nuclear spin decays in a solid," *Phys. Rev. Lett.*, vol. 101, p. 067601, 2008. 2

[4] T. A. Elsayed and B. V. Fine, "Regression relation for pure quantum states and its implications for efficient computing," *Phys. Rev. Lett.*, vol. 110, p. 070404, Feb 2013. 2, 57, 61, 68, 71, 79, 108, 143

[5] B. V. Fine, T. A. Elsayed, C. M. Kropf, and A. S. de Wijn, "Absence of exponential sensitivity to small perturbations in nonintegrable systems of spins 1/2," *ArXiv preprints arXiv:1305.2817*, May 2013. 3, 98, 114

[6] B. V. Chirikov, "The problem of quantum chaos," in *Chaos and Quantum Chaos*, pp. 1–56, Springer, 1992. 4

[7] J. Realpe and G. Ordonez, "The role of chaos and resonances in brownian motion," in *Chaos, Nonlinearity, Complexity*, pp. 179–206, Springer, 2006. 4

[8] G. Gallavotti, "Chaotic dynamics, fluctuations, nonequilibrium ensembles," *Chaos: An Interdisciplinary Journal of Nonlinear Science*, vol. 8, no. 2, pp. 384–392, 1998.

[9] P. Gaspard, *Chaos, scattering and statistical mechanics*, vol. 9. Cambridge University Press, 2005. 4

[10] P. Gaspard, M. E. Briggs, M. K. Francis, J. V. Sengers, R. W. Gammon, J. R. Dorfman, and R. V. Calabrese, "Experimental evidence for microscopic chaos," *Nature*, vol. 394, pp. 865–868, Aug. 1998. 4, 18

[11] C. P. Dettmann, E. G. D. Cohen, and v. H., "Statistical mechanics: Microscopic chaos from brownian motion?," *Nature*, vol. 401, pp. 875–876, Oct. 1999. 4, 18

[12] B. V. Fine, "Universal long-time relaxation on lattices of classical spins: Markovian behavior on non-markovian timescales," *Journal of Statistical Physics*, vol. 112, pp. 319–327, July 2003. 4, 98, 126

[13] B. V. Fine, "Long-time relaxation on spin lattice as a manifestation of chaotic dynamics," *Int. J. Mod. Phys. B*, vol. 18, pp. 1119–1159, 2004. (cond-mat/9911230). 4, 34, 125

[14] T. Prosen, "Chaos and complexity of quantum motion," *Journal of Physics A: Mathematical and Theoretical*, vol. 40, no. 28, p. 7881, 2007. 5

[15] J. Ford, "Quantum chaos, is there any?," *Directions In Chaos—Volume 2. Series: Series on Directions in Condensed Matter Physics, World Scientific, Edited by BL Hao*, vol. 4, pp. 128–147, 1988. 5

[16] T. Kapitaniak, *Chaotic oscillators: theory and applications*. World Scientific, 1992. 6

[17] G. Benettin, L. Galgani, A. Giorgilli, and J.-M. Strelcyn, "Lyapunov characteristic exponents for smooth dynamical systems and for hamiltonian systems; a method for computing all of them. part 1: Theory," *Meccanica*, vol. 15, no. 1, pp. 9–20, 1980. 6

[18] L. Casetti, M. Cerruti-Sola, M. Pettini, and E. G. D. Cohen, "The Fermi-Pasta-Ulam problem revisited: Stochasticity thresholds in nonlinear Hamiltonian systems," *Phys. Rev. E*, vol. 55, pp. 6566–6574, Jun 1997. 6

[19] A. S. de Wijn, B. Hess, and B. V. Fine, "Largest Lyapunov Exponents for Lattices of Interacting Classical Spins," *Phys. Rev. Lett.*, vol. 109, p. 034101, Jul 2012. 8, 24, 33, 86, 99

[20] P. A. Miller and S. Sarkar, "Entropy production, dynamical localization and criteria for quantum chaos in the open quantum kicked rotor," *Nonlinearity*, vol. 12, no. 2, p. 419, 1999. 9, 12

[21] M. Hossein Partovi, "Entropic formulation of chaos for quantum dynamics," *Physics Letters A*, vol. 151, no. 8, pp. 389–394, 1990. 9

[22] G. M. Zaslavsky, "Stochasticity in quantum systems," *Physics Reports*, vol. 80, no. 3, pp. 157 – 250, 1981. 9, 11

[23] J.-S. Caux and J. Mossel, "Remarks on the notion of quantum integrability," *Journal of Statistical Mechanics: Theory and Experiment*, vol. 2011, no. 02, p. P02023, 2011. 9

[24] B. Sutherland and B. Sutherland, *Beautiful models: 70 years of exactly solved quantum many-body problems*. World Scientific, 2004. 9

[25] A. Peres, "Stability of quantum motion in chaotic and regular systems," *Physical Review A*, vol. 30, pp. 1610–1615, Oct. 1984. 10, 83

[26] N. Moiseyev and A. Peres, "Motion of wave packets in regular and chaotic systems," *The Journal of Chemical Physics*, vol. 79, no. 12, pp. 5945–5950, 1983. 10

[27] E. Ott and T. Tel, "Chaotic scattering: An introduction," *Chaos: An Interdisciplinary Journal of Nonlinear Science*, vol. 3, no. 4, pp. 417–426, 1993. 10

[28] O. Bohigas, M. J. Giannoni, and C. Schmit, "Characterization of chaotic quantum spectra and universality of level fluctuation laws," *Phys. Rev. Lett.*, vol. 52, pp. 1–4, Jan 1984. 10, 86

[29] F. Haake, *Quantum signatures of chaos*. Springer, 2010. 11, 15

[30] A. Relaño, J. M. G. Gómez, R. A. Molina, J. Retamosa, and E. Faleiro, "Quantum chaos and $1/f$ noise," *Phys. Rev. Lett.*, vol. 89, p. 244102, Nov 2002. 11

[31] L. Santos, F. Borgonovi, and F. Izrailev, "Onset of chaos and relaxation in isolated systems of interacting spins: Energy shell approach," *Physical Review E*, vol. 85, no. 3, p. 036209, 2012. 11

[32] V. Zelevinsky, B. Brown, N. Frazier, and M. Horoi, "The nuclear shell model as a testing ground for many-body quantum chaos," *Physics Reports*, vol. 276, no. 2–3, pp. 85 – 176, 1996. 11

[33] L. F. Santos and M. Rigol, "Fluctuations in the delocalization level of eigenstates and thermalization," *Physica Scripta*, vol. 2012, no. T151, p. 014033, 2012. 11

[34] P. Pechukas, "Remarks on " quantum chaos"," *The Journal of Physical Chemistry*, vol. 88, no. 21, pp. 4823–4829, 1984. 11

[35] B. Eckhardt, "Quantum mechanics of classically non-integrable systems," *Physics Reports*, vol. 163, no. 4, pp. 205–297, 1988. 11

[36] I. Percival, "Regular and irregular spectra," *Journal of Physics B: Atomic and Molecular Physics*, vol. 6, no. 9, p. L229, 1973. 11

[37] L. Benet, T. H. Seligman, and H. A. Weidenmüller, "Quantum signatures of classical chaos: Sensitivity of wave functions to perturbations," *Phys. Rev. Lett.*, vol. 71, pp. 529–532, Jul 1993. 12

[38] A. Peres, "The many faces of quantum chaos," *Chaos, Solitons & Fractals*, vol. 5, no. 7, pp. 1069–1075, 1995. 12

[39] M. Feit and J. Fleck Jr, "Wave packet dynamics and chaos in the Hénon–Heiles system," *The Journal of chemical physics*, vol. 80, p. 2578, 1984. 12

[40] W. H. Zurek and J. P. Paz, "Decoherence, chaos, and the second law," *Phys. Rev. Lett.*, vol. 72, pp. 2508–2511, Apr 1994. 12

[41] V. V. Sokolov, O. V. Zhirov, and Y. A. Kharkov, "Classical versus quantum dynamical chaos: Sensitivity to external perturbations, stability and reversibility," in *Chaos Theory: Modeling, Simulation and Applications-Selected Papers from the 3rd Chaotic Modeling and Simulation International Conference (chaos2010)*, p. 59, World Scientific, 2011. 12

[42] G. Casati and D. Rossini, "Dynamical chaos and decoherence," *Progress of Theoretical Physics Supplement*, vol. 166, no. Supplement 1, pp. 70–84, 2007. 13

[43] A. K. Pattanayak and P. Brumer, "Exponentially rapid decoherence of quantum chaotic systems," *Phys. Rev. Lett.*, vol. 79, pp. 4131–4134, Nov 1997. 13

[44] M. V. Berry, "Chaos and the semiclassical limit of quantum mechanics (is the moon there when somebody looks?)," *Quantum Mechanics: Scientific perspectives on divine action*, p. 41, 2001. 13, 89

[45] S. Habib, K. Shizume, and W. H. Zurek, "Decoherence, chaos, and the correspondence principle," *Phys. Rev. Lett.*, vol. 80, pp. 4361–4365, May 1998. 13

[46] A. W. Sandvik, "Computational studies of quantum spin systems," *arXiv preprint arXiv:1101.3281*, 2011. 14

[47] H. Kantz and T. Schreiber, *Nonlinear time series analysis*. Cambridge university press, 2003. 17, 24

[48] A. Babloyantz and A. Destexhe, "Is the normal heart a periodic oscillator?," *Biological Cybernetics*, vol. 58, pp. 203–211, 1988. 17

[49] E. E. Peters, *Chaos and order in the capital markets: a new view of cycles, prices, and market volatility*. John Wiley & Sons, 1996. 17

[50] T. Sleator, E. L. Hahn, C. Hilbert, and J. Clarke, "Nuclear-spin noise," *Phys. Rev. Lett.*, vol. 55, pp. 1742–1745, Oct 1985. 18

[51] J. Schlagnitweit, J.-N. Dumez, M. Nausner, A. Jerschow, B. Elena-Herrmann, and N. Müller, "Observation of NMR noise from solid samples," *Journal of Magnetic Resonance*, vol. 207, pp. 168–172, Nov. 2010. 18

[52] C. Dettmann and E. Cohen, "Microscopic chaos and diffusion," *Journal of Statistical Physics*, vol. 101, no. 3-4, pp. 775–817, 2000. 18

[53] N. H. Packard, J. P. Crutchfield, J. D. Farmer, and R. S. Shaw, "Geometry from a time series," *Phys. Rev. Lett.*, vol. 45, pp. 712–716, Sep 1980. 19

[54] A. Wolf, J. B. Swift, H. L. Swinney, and J. A. Vastano, "Determining Lyapunov exponents from a time series," *Physica D: Nonlinear Phenomena*, vol. 16, no. 3, pp. 285–317, 1985. 19, 47

[55] J. P. Eckmann, S. O. Kamphorst, D. Ruelle, and S. Ciliberto, "Liapunov exponents from time series," *Phys. Rev. A*, vol. 34, pp. 4971–4979, Dec 1986.

[56] M. T. Rosenstein, J. J. Collins, and C. J. De Luca, "A practical method for calculating largest Lyapunov exponents from small data sets," *Physica D: Nonlinear Phenomena*, vol. 65, no. 1, pp. 117–134, 1993.

[57] H. Kantz, "A robust method to estimate the maximal Lyapunov exponent of a time series," *Physics letters A*, vol. 185, no. 1, pp. 77–87, 1994. 19

[58] P. Grassberger and I. Procaccia, "Estimation of the Kolmogorov entropy from a chaotic signal," *Phys. Rev. A*, vol. 28, pp. 2591–2593, Oct 1983. 22, 24

[59] A. Cohen and I. Procaccia, "Computing the Kolmogorov entropy from time signals of dissipative and conservative dynamical systems," *Phys. Rev. A*, vol. 31, pp. 1872–1882, Mar 1985. 22

[60] P. Gaspard and X. Wang, "Noise, chaos, and (ϵ, τ)-entropy per unit time," *Physics Reports*, vol. 235, pp. 291–343, Dec. 1993. 23, 24, 26

[61] Ya.B. Pesin, Math. USSR Izv. 10(6) (1976) 1261. 24

[62] A. Cohen and I. Procaccia, "Survival of deterministic dynamics in the presence of noise and the exponential decay of power spectra at high frequency," *Phys. Rev. A*, vol. 31, p. 1872, 1985. 24

[63] F. Harris, Proceedings of the IEEE **66**, 51 (1978). 28

[64] J. W. Tukey, "An introduction to the calculations of numerical spectrum analysis," *Spectral Analysis of Time Series*, pp. 25–46, 1967. 28

[65] D. Sigeti and W. Horsthemke, "High-frequency power spectra for systems subject to noise," *Phys. Rev. A*, vol. 35, pp. 2276–2282, Mar 1987. 29

[66] D. E. Sigeti, "Exponential decay of power spectra at high frequency and positive Lyapunov exponents," *Physica D: Nonlinear Phenomena*, vol. 82, no. 1-2, pp. 136 – 153, 1995.

[67] D. E. Sigeti, "Survival of deterministic dynamics in the presence of noise and the exponential decay of power spectra at high frequency," *Phys. Rev. E*, vol. 52, pp. 2443–2457, Sep 1995.

[68] J. D. Farmer, "Chaotic attractors of an infinite-dimensional dynamical system," *Physica D: Nonlinear Phenomena*, vol. 4, no. 3, pp. 366 – 393, 1982. 29

[69] M. Tabor and J. Weiss, "Analytic structure of the Lorenz system," *Phys. Rev. A*, vol. 24, pp. 2157–2167, Oct 1981. 30

[70] U. Frisch and R. Morf, "Intermittency in nonlinear dynamics and singularities at complex times," *Phys. Rev. A*, vol. 23, pp. 2673–2705, May 1981. 30

[71] T. C. Bountis, "A singularity analysis of integrability and chaos in dynamical systems," in *Singularities and Dynamical Systems, Proceedings of the International Conference on Singularities and Dynamical Systems* (S. N. Pnevmatikos, ed.), North-Holland, 1985. 30

[72] A. B. Migdal, *Qualitative methods in quantum theory*. Cambridge: Advanced Book Program, Perseus Pub, 2000. 30

[73] K. Ramasubramanian and M. Sriram, "A comparative study of computation of Lyapunov spectra with different algorithms," *Physica D: Nonlinear Phenomena*, vol. 139, no. 1, pp. 72–86, 2000. 31, 46

[74] G. Casati and B. Chirikov, "Quantum chaos: unexpected complexity," *Physica D: Nonlinear Phenomena*, vol. 86, no. 1, pp. 220–237, 1995. 31

[75] A. A. Lundin, A. V. Makarenko, and V. E. Zobov, "The dipolar fluctuation spectrum and the shape of the wings of nuclear magnetic resonance absorption spectra in solids," *Journal of Physics Condensed Matter*, vol. 2, pp. 10131–10145, Dec. 1990. 34

[76] J. Stolze, A. Nöppert, and G. Müller, "Gaussian, exponential, and power-law decay of time-dependent correlation functions in quantum spin chains," *Phys. Rev. B*, vol. 52, pp. 4319–4326, Aug 1995. 34

[77] T. Stachowiak and T. Okada, "A numerical analysis of chaos in the double pendulum," *Chaos, Solitons & Fractals*, vol. 29, no. 2, pp. 417–422, 2006. 46

[78] I. Shevchenko and A. Mel'nikov, "Lyapunov exponents in the Hénon-Heiles problem," *Journal of Experimental and Theoretical Physics Letters*, vol. 77, no. 12, pp. 642–646, 2003. 46

[79] T. Konishi and K. Kaneko, "Clustered motion in symplectic coupled map systems," *Journal of Physics A: Mathematical and General*, vol. 25, no. 23, p. 6283, 1992. 46

[80] J. J. Morales-Ruiz and J. P. Ramis, "A note on the non-integrability of some hamiltonian systems with a homogeneous potential," *Methods and applications of analysis*, vol. 8, no. 1, pp. 113–120, 2001. 49

[81] M. Olshanetsky and A. M. Perelomov, "Classical integrable finite-dimensional systems related to Lie algebras," *Physics Reports*, vol. 71, no. 5, pp. 313–400, 1981. 49

[82] A. Ramani, B. Grammaticos, and T. Bountis, "The Painleve property and singularity analysis of integrable and non-integrable systems," *Physics Reports*, vol. 180, pp. 159 – 245, 1989. 49

[83] M. C. Gutzwiller, *Chaos in classical and quantum mechanics*. Springer, 1990. 51, 52

[84] H. Flaschka, "The Toda lattice. II. Existence of integrals," *Phys. Rev. B*, vol. 9, pp. 1924–1925, Feb 1974. 51

[85] H. Yoshida, "Non-integrability of the truncated Toda lattice Hamiltonian at any order," *Communications in mathematical physics*, vol. 116, no. 4, pp. 529–538, 1988. 52

[86] C. Bartsch and J. Gemmer, "Dynamical typicality of quantum expectation values," *Phys. Rev. Lett.*, vol. 102, p. 110403, 2009. 57

[87] L. Onsager, "Reciprocal relations in irreversible processes. ii.," *Phys. Rev.*, vol. 38, pp. 2265–2279, Dec 1931. 58

[88] M. Lax, "The Lax-Onsager regression 'theorem' revisited," *Optics Communications*, vol. 179, pp. 463–476, May 2000. 59

[89] H. B. Callen and T. A. Welton, "Irreversibility and generalized noise," *Phys. Rev.*, vol. 83, pp. 34–40, Jul 1951. 59

[90] U. M. B. Marconi, A. Puglisi, L. Rondoni, and A. Vulpiani, "Fluctuation–dissipation: Response theory in statistical physics," *Physics Reports*, vol. 461, pp. 111–195, June 2008. 59

[91] R. Kubo, "Statistical-mechanical theory of irreversible processes. I. General theory and simple applications to magnetic and conduction problems," *Journal of the Physical Society of Japan*, vol. 12, pp. 570–586, 1957. 59, 119

[92] H. B. Callen and T. A. Welton, "Irreversibility and generalized noise," *Phys. Rev.*, vol. 83, pp. 34–40, Jul 1951. 60

[93] G. W. Ford and R. F. O'Connell, "There is no quantum regression theorem," *Phys. Rev. Lett.*, vol. 77, pp. 798–801, Jul 1996. 62

[94] R. Karplus and J. Schwinger, "A note on saturation in microwave spectroscopy," *Phys. Rev.*, vol. 73, pp. 1020–1026, May 1948. 62

[95] See supplementary material of reference [4]. 63

[96] P. Reimann, "Typicality for generalized microcanonical ensembles," *Phys. Rev. Lett.*, vol. 99, p. 160404, Oct 2007. 63

[97] C. Bartsch and J. Gemmer, "Dynamical typicality of quantum expectation values," *Phys. Rev. Lett.*, vol. 102, p. 110403, 2009. 63, 64

[98] S. Goldstein, J. L. Leibowitz, R. Tumulka, and N. Zanghi, "Canonical typicality," *Phys. Rev. Lett.*, vol. 96, p. 050403, 2006. 63

[99] S. R. White, "Density matrix formulation for quantum renormalization groups," *Phys. Rev. Lett.*, vol. 69, pp. 2863–2866, Nov 1992. 69

[100] S. R. White and A. E. Feiguin, "Real-time evolution using the density matrix renormalization group," *Phys. Rev. Lett.*, vol. 93, p. 076401, Aug 2004. 69

[101] G. Vidal, "Classical simulation of infinite-size quantum lattice systems in one spatial dimension," *Phys. Rev. Lett.*, vol. 98, p. 070201, Feb 2007. 69

[102] G. Vidal, "Efficient classical simulation of slightly entangled quantum computations," *Phys. Rev. Lett.*, vol. 91, p. 147902, Oct 2003. 69

[103] F. Verstraete and J. Cirac, "Renormalization algorithms for quantum-many body systems in two and higher dimensions," *cond-mat/0407066*, 2004. 69

[104] G. M. Crosswhite, A. C. Doherty, and G. Vidal, "Applying matrix product operators to model systems with long-range interactions," *Phys. Rev. B*, vol. 78, p. 035116, Jul 2008. 69

[105] H. Tal-Ezer and R. Kosloff, "An accurate and efficient scheme for propagating the time dependent Schrödinger equation," *J. Chem. Phys.*, vol. 81, no. 9, pp. 3967–3971, 1984. 70

[106] M. Suzuki and K. Umeno in *Computer Simulation Studies in Condensed Matter Physics VI* (D. P. Landau, K. K. Mon, and H. B. Schüttler, eds.), Springer, Berlin, 1993. 70

[107] T. J. Park and J. Light, "Unitary quantum time evolution by iterative Lanczos reduction," *The Journal of chemical physics*, vol. 85, p. 5870, 1986. 70

[108] M. Hochbruck and C. Lubich, "On Krylov subspace approximations to the matrix exponential operator," *SIAM Journal on Numerical Analysis*, vol. 34, no. 5, pp. 1911–1925, 1997. 70

[109] S. R. White, "Minimally entangled typical quantum states at finite temperature," *Phys. Rev. Lett.*, vol. 102, p. 190601, 2009. 73

[110] G. A. Álvarez, E. P. Danieli, P. R. Levstein, and H. M. Pastawski, "Quantum parallelism as a tool for ensemble spin dynamics calculations," *Phys. Rev. Lett.*, vol. 101, p. 120503, Sep 2008. 74

[111] F. Bloch, "Nuclear induction," *Phys. Rev.*, vol. 70, pp. 460–474, 1946. 75

[112] B. V. Fine, "Typical state of an isolated quantum system with fixed energy and unrestricted participation of eigenstates," *Phys. Rev. E*, vol. 80, p. 051130, Nov 2009. 76

[113] L. Devroye, *Non-uniform random variate generation*. Springer-Verlag, 1986. 76

[114] J. Gemmer, M. Michel, and G. Mahler, *Quantum Thermodynamics: Emergence of Thermodynamic Behavior Within Composite Quantum Systems*. Springer, 1 ed., Feb. 2005. 77

[115] A. Polkovnikov, K. Sengupta, A. Silva, and M. Vengalattore, "*Colloquium*: Nonequilibrium dynamics of closed interacting quantum systems," *Rev. Mod. Phys.*, vol. 83, pp. 863–883, 2011. 80

[116] J. Ford and M. Ilg, "Eigenfunctions, eigenvalues, and time evolution of finite, bounded, undriven, quantum systems are not chaotic," *Phys. Rev. A*, vol. 45, pp. 6165–6173, May 1992. 81

[117] L. G. Yaffe, "Large n limits as classical mechanics," *Rev. Mod. Phys.*, vol. 54, pp. 407–435, Apr 1982. 82

[118] E. Lieb, "The classical limit of quantum spin systems," *Communications in Mathematical Physics*, vol. 31, no. 4, pp. 327–340, 1973. 82

[119] T. Gorin, T. Prosen, T. H. Seligman, and M. Žnidarič, "Dynamics of Loschmidt echoes and fidelity decay," *Physics Reports*, vol. 435, pp. 33–156, Nov. 2006. 83

[120] J. Bolte and T. Schwaibold, "Stability of wave-packet dynamics under perturbations," *Physical Review E*, vol. 73, p. 026223, Feb. 2006. 83

[121] R. A. Jalabert and H. M. Pastawski, "Environment-independent decoherence rate in classically chaotic systems," *Physical Review Letters*, vol. 86, pp. 2490–2493, Mar. 2001. 83

[122] F. M. Cucchietti, C. H. Lewenkopf, E. R. Mucciolo, H. M. Pastawski, and R. O. Vallejos, "Measuring the Lyapunov exponent using quantum mechanics," *Physical Review E*, vol. 65, p. 046209, Apr. 2002. 83, 89

[123] D. D'Alessandro, *Introduction to Quantum Control and Dynamics*. Chapman and Hall/CRC, Aug. 2007. 83

[124] L. E. Reichl, *The transition to chaos: Conservative classical systems and quantum manifestations*. Springer, 2004. 85

[125] G. Benenti and G. Casati, "How complex is quantum motion?," *Physical Review E*, vol. 79, p. 025201, Feb. 2009. 86

[126] J. Emerson, Y. S. Weinstein, S. Lloyd, and D. G. Cory, "Fidelity decay as an efficient indicator of quantum chaos," *Phys. Rev. Lett.*, vol. 89, p. 284102, Dec 2002. 86

[127] R. Schack and C. M. Caves, "Hypersensitivity to perturbations in the quantum baker's map," *Phys. Rev. Lett.*, vol. 71, pp. 525–528, Jul 1993. 88, 132

[128] R. Blümel and B. Esser, "Type II quantum chaos," *Zeitschrift für Physik B Condensed Matter*, vol. 98, pp. 119–131, Mar. 1995. 89

[129] R. V. Mendes, "Sensitive dependence and entropy for quantum systems," *Journal of Physics A: Mathematical and General*, vol. 24, no. 18, p. 4349, 1991. 89

[130] V. Man'ko and R. Vilela Mendes, "Lyapunov exponent in quantum mechanics. a phase-space approach," *Physica D: Nonlinear Phenomena*, vol. 145, no. 3, pp. 330–348, 2000.

[131] L. E. Ballentine, "Lyapunov exponents for the differences between quantum and classical dynamics," *Phys. Rev. A*, vol. 63, p. 024101, Jan 2001.

[132] U. Schwengelbeck and F. Faisal, "Definition of Lyapunov exponents and KS entropy in quantum dynamics," *Physics Letters A*, vol. 199, no. 5, pp. 281–286, 1995. 89, 90

[133] G. Müller, "Nature of quantum chaos in spin systems," *Phys. Rev. A*, vol. 34, pp. 3345–3355, Oct 1986. 90

[134] S. Gade and I. J. Lowe, "Nuclear magnetic resonance line-shape calculations for a spin system in a fixed lattice," *Phys. Rev.*, vol. 148, pp. 382–392, Aug 1966. 96, 126

[135] D. K. Sodickson and J. S. Waugh, "Spin diffusion on a lattice: Classical simulations and spin coherent states," *Phys. Rev. B*, vol. 52, pp. 6467–6479, Sep 1995. 98, 115, 126

[136] S. J. Vlaev and L. M. Gaggero-Sager, eds., *Problems of Condensed Matter Physics*. Nova Science Pub Inc, 2001. 99

[137] W.-K. Rhim, A. Pines, and J. S. Waugh, "Time-reversal experiments in dipolar-coupled spin systems," *Phys. Rev. B*, vol. 3, pp. 684–696, Feb 1971. 101

[138] C. P. Slichter, *Principles of Magnetic Resonance*. Springer, 1990. 101

[139] H. M. Pastawski, P. R. Levstein, G. Usaj, J. Raya, and J. Hirschinger, "A nuclear magnetic resonance answer to the Boltzmann–Loschmidt controversy?," *Physica A: Statistical Mechanics and its Applications*, vol. 283, no. 1, pp. 166–170, 2000. 101

[140] A. Goussev, R. A. Jalabert, H. M. Pastawski, and D. A. Wisniacki, "Loschmidt echo," *Scholarpedia*, vol. 7, no. 8, p. 11687, 2012. 102

[141] C. Bartsch and J. Gemmer, "Dynamical typicality of quantum expectation values," *Phys. Rev. Lett.*, vol. 102, p. 110403, Mar 2009. 108

[142] S. Wolf, D. Awschalom, R. Buhrman, J. Daughton, S. Von Molnar, M. Roukes, A. Y. Chtchelkanova, and D. Treger, "Spintronics: A spin-based electronics vision for the future," *Science*, vol. 294, no. 5546, pp. 1488–1495, 2001. 115

[143] M. E. Fisher, "Magnetism in one-dimensional systems—The heisenberg model for infinite spin," *American Journal of Physics*, vol. 32, no. 5, pp. 343–346, 1964. 115

[144] C. Tang and J. S. Waugh, "Dynamics of classical spins on a lattice: Spin diffusion," *Phys. Rev. B*, vol. 45, pp. 748–754, 1992. 115, 126, 127

[145] R. Steinigeweg, "Spin transport in the XXZ model at high temperatures: Classical dynamics vs. quantum s=1/2 autocorrelations," *EPL (Europhysics Letters)*, vol. 97, no. 6, p. 67001, 2012. 116, 117

[146] N. Bloembergen, "On the interaction of nuclear spins in a crystalline lattice," *Physica*, vol. 15, pp. 386 – 426, 1949. 116

[147] P. De Gennes, "Inelastic magnetic scattering of neutrons at high temperatures," *Journal of Physics and Chemistry of Solids*, vol. 4, no. 3, pp. 223–226, 1958.

[148] A. G. Redfield, "Spatial diffusion of spin energy," *Phys. Rev.*, vol. 116, pp. 315–316, Oct 1959. 116

[149] K. Fabricius, U. Löw, and J. Stolze, "Dynamic correlations of antiferromagnetic spin- XXZ chains at arbitrary temperature from complete diagonalization," *Phys. Rev. B*, vol. 55, pp. 5833–5846, Mar 1997. 117

[150] J. Sirker, R. G. Pereira, and I. Affleck, "Diffusion and ballistic transport in one-dimensional quantum systems," *Phys. Rev. Lett.*, vol. 103, p. 216602, 2009. 117, 119, 120

[151] M. Žnidarič, "Spin transport in a one-dimensional anisotropic heisenberg model," *Phys. Rev. Lett.*, vol. 106, p. 220601, 2011. 117, 119

[152] O. F. de Alcantara Bonfim and G. Reiter, "Breakdown of hydrodynamics in the classical 1D heisenberg model," *Phys. Rev. Lett.*, vol. 69, pp. 367–370, 1992. 118

[153] O. F. de Alcantara Bonfim and G. Reiter, "Breakdown of hydrodynamics in the classical 1d heisenberg model," *Phys. Rev. Lett.*, vol. 69, pp. 367–370, 1992. 118

[154] M. S. Green, "Markoff random processes and the statistical mechanics of time-dependent phenomena. ii. irreversible processes in fluids," *The Journal of Chemical Physics*, vol. 22, no. 3, pp. 398–413, 1954. 119

[155] S. Lepri, R. Livi, and A. Politi, "Thermal conduction in classical low-dimensional lattices," *Physics Reports*, vol. 377, no. 1, pp. 1 – 80, 2003. 119

[156] H. van Beijeren, "Exact results for anomalous transport in one-dimensional hamiltonian systems," *Phys. Rev. Lett.*, vol. 108, p. 180601, 2012. 119

[157] M. Žnidarič, "Spin transport in a one-dimensional anisotropic heisenberg model," *Phys. Rev. Lett.*, vol. 106, p. 220601, 2011. 120

[158] T. Prosen, "Open xxz spin chain: Nonequilibrium steady state and a strict bound on ballistic transport," *Phys. Rev. Lett.*, vol. 106, p. 217206, May 2011. 120

[159] K. Fabricius and B. M. McCoy, "Spin diffusion and the spin-1/2 XXZ chain at $t = \infty$ from exact diagonalization," *Phys. Rev. B*, vol. 57, pp. 8340–8347, 1998. 121

[160] A. Abragam, *Principles of Nuclear Magnetism*. Oxford University Press, 1961. 125

[161] M. Engelsberg and I. J. Lowe, "Free-inducation-decay measurements and determination of moments in caf_2," *Phys. Rev. B*, vol. 10, pp. 822–832, Aug 1974. 127

[162] B. Meier, J. Kohlrautz, and J. Haase, "Eigenmodes in the long-time behavior of a coupled spin system measured with nuclear magnetic resonance," *Phys. Rev. Lett.*, vol. 108, p. 177602, Apr 2012. 127

[163] N. Van Kampen, "The case against linear response theory," *Physica Norvegica*, vol. 5, no. 3-4, pp. 279–284, 1971. 128

[164] J. Kohlrautz, T. Meissner, and J. Haase, "Long-time behaviour of the FID in metallic aluminum." In preparation. 129, 130

[165] R. Schack and C. M. Caves, "Information-theoretic characterization of quantum chaos," *Phys. Rev. E*, vol. 53, pp. 3257–3270, Apr 1996. 131

[166] A. K. Pattanayak, "Lyapunov exponents, entropy production, and decoherence," *Phys. Rev. Lett.*, vol. 83, pp. 4526–4529, Nov 1999. 131

[167] R. Schack, G. M. D'Ariano, and C. M. Caves, "Hypersensitivity to perturbation in the quantum kicked top," *Phys. Rev. E*, vol. 50, pp. 972–987, Aug 1994. 132

[168] M. H. Partovi, "Absence of sensitivity to initial conditions in quantum dynamics," *Phys. Rev. A*, vol. 45, pp. R555–R558, Jan 1992. 132

[169] K. Ji and B. V. Fine, "Nonthermal statistics in isolated quantum spin clusters after a series of perturbations," *Phys. Rev. Lett.*, vol. 107, p. 050401, Jul 2011. 133